主論文

VARIOUS INTERMEDIATE CHANNELS IN $^{12}C+^{12}C \rightarrow ^{12}C_{g.s.}+\alpha+^{8}Be_{g.s.}$ REACTION

Susumu SHIMOURA

VARIOUS INTERMEDIATE CHANNELS IN $^{12}C+^{12}C \rightarrow ^{12}C_{g.s.}+\alpha+^{8}Be_{g.s.}$ REACTION

Susumu SHIMOURA

Department of Physics,
Faculty of Science,
Kyoto University

CONTENTS

CHAPTER 1

Introduction

In heavy-ion induced reactions, a large part of the total reaction cross section consists of fusion, deep-inelastic collision, quasi-elastic scattering and so on, where many degrees of freedom participate. These reactions have been often analyzed in terms of models relevant to macroscopic aspects of the reaction, e.g. a friction model. On the other hand, there are also many direct-like processes such as breakup and inelastic scattering or few-nucleon transfers to low-lying states, especially in reactions between light-heavy nuclei (C, N, O, Ne etc.). These reactions, where fewer degrees of freedom participate, have been usually analyzed in terms of models based on full quantum mechanics such as distorted wave Born approximation (DWBA) or coupled-channel calculations[1] . Such analyses have been used for deducing quantum numbers of discrete states such as spin and parity, or for microscopic understanding of the reaction mechanism[2,3] .

As the bombarding energy is increased, at 5 - 10 MeV/nucleon, states with higher excitation energy and spin can be populated by direct-like process due to the kinematical matching condition of linear and angular momenta between initial and final channels[4,5] . Note that these states are hardly populated by light-ion induced reactions. When these states lie above particle threshold, they subsequently decay by particle emission. The final channel of the reaction consists of three particles. For example, the cross

section of the process associated with α-particle emission is considerably large due to relatively low α-particle threshold and α-cluster structure of the light-heavy nuclei. Such α-particles are sometimes detected to determine the properties (spin, parity or partial width) of the decaying states[6-9] or to investigate the reaction mechanism by obtaining spin-distributions (sub-state populations) of the decaying states[7,10,11]. In the former case, model-independent determination[12] of spin and parity of the decaying state have often been made.

However, for the study of such high-lying states above particle threshold, a serious inherent difficulty is that various processes possibly lead to the same three-body final channel; when one investigates a specific process or decaying state, other undesired processes leading to the same final channel intrude[13-15]. Such undesired processes so far have been often treated only as "contaminants", and studied less quantitatively. However, cross sections of such "contaminants" are often of the same order of magnitude as that of the specific process. Such an example is also seen in the studies of the breakup reactions induced by light-heavy nuclei[16-20]. Therefore, from a new point of view, it is interesting to investigate various processes leading to the same final channel on an equal footing for a thorough understanding of the reaction mechanism. Then, it is possible to study the following interesting problems:

(1) What processes contribute to a three-body final channel and how much is the cross section for each process?

(2) What is the mechanism of each process: Is it a simple direct

transition of binary character (with sequential particle decay)?

(3) Is there any aspect which cannot be understood as a binary process, *i.e.* an effect where all of the three particles interact at the same time?

In order to discuss these problems, it is necessary to perform coincidence experiment where reaction products are detected over a wide angular region and a wide dynamic range of energy. The data analysis is to be performed based on three-body kinematics dealing with various processes at the same time.

We have investigated the $^{12}C+^{12}C \rightarrow ^{12}C_{g.s.}+\alpha+^{8}Be_{g.s.}$ reaction at bombarding energies around 10 MeV/nucleon as one of the simplest systems where various intermediate channels are to be observed. In this reaction, it is possible to consider the following different processes:

(i) inelastic scattering process with subsequent α-decay

$$^{12}C+^{12}C \rightarrow ^{12}C_{g.s.}+^{12}C^{*} \rightarrow ^{12}C_{g.s.}+\alpha+^{8}Be_{g.s.} ,$$

(ii) alpha-transfer process with subsequent α-decay

$$^{12}C+^{12}C \rightarrow ^{16}O^{*}+^{8}Be_{g.s.} \rightarrow ^{12}C_{g.s.}+\alpha+^{8}Be_{g.s.} ,$$

(iii) ^{8}Be-transfer process with subsequent ^{8}Be-particle decay

$$^{12}C+^{12}C \rightarrow \alpha+^{20}Ne^{*} \rightarrow \alpha+^{12}C_{g.s.}+^{8}Be_{g.s.} , \text{ and}$$

(iv) non-resonant (direct) breakup process without resonant states in the intermediate channels

$$^{12}C+^{12}C \rightarrow ^{12}C_{g.s.}+\alpha+^{8}Be_{g.s.} \quad .$$

This reaction is considered to be mostly direct-like because the compound system (^{24}Mg) at high excitation energy easily evaporates more than three particles. In this case, reaction products of the primary process are emitted in the forward direction. Particles in the forward direction ^{12}C and α were detected in coincidence over wide angular regions (5° - 20° for ^{12}C and 8° - 50° for α-particles) and wide dynamic range of the energies (typically, $E_{^{12}C} > 10$ MeV and $E_{\alpha} > 1$ MeV). Another α-detector was set covering 100° - 152° to detect α-particles decaying into backward angles. More details of the experimental procedure are described in chapter 2.

From analysis based on the three-body kinematics, which is described in appendix A, processes (i)-(iv) were clearly identified. It was found that the processes (i) (inelastic scattering) and (ii) (α-transfer) have most of the cross sections and that the cross sections of the other processes (iii) and (iv) are small. The data are presented and discussed in section 1 of chapter 3.

For the main processes (i) and (ii), coincidence cross sections in the form of double-differential cross sections[6,7] (the angular distribution of the primary process and the angular correlation in the decay process) were obtained. The observed double-differential cross sections for the discrete states were reproduced well by the calculation based on a finite-range DWBA. For the α-transfer process, the transferred angular momentum in

the primary process was determined by the oscillatory angular correlation patterns. We could also explain the observed shifts of the correlation functions depending on the angle of the primary process. The experimental data and discussion are given in section 2 of chapter 3.

In this reaction, there are kinematical regions where the different intermediate channels of the processes (i) and (ii) can contribute at the same time. As mentioned in ref. 21, at these regions there is a possibility of interference between the different intermediate channels. We obtained the cross sections at such regions, and then, found that the cross sections could not be explained by a simple sum of the cross sections estimated individually for these two intermediate channels. Therefore, it is concluded that evidence for the interference of the intermediate channels has been observed for the first time. By taking into account the interference between DWBA *T*-matrices calculated independently for the two processes, characteristics of the observed cross sections could be understood qualitatively. Section 3 of chapter 3 is devoted for a detailed discussion of this interference effect.

Chapter 4 gives summary and conclusions.

CHAPTER 2

Experimental procedure

The experiments were performed with $^{12}C^{4+}$- projectiles of 90, 110, and 140 MeV from the AVF cyclotron of the Research Center for Nuclear Physics, Osaka University. Incident beams were focused onto a 1.1 mg/cm^2 natural carbon foil positioned at the center of a 1 m ϕ scattering chamber.

The experimental setup for the ^{12}C-α coincidence measurement is shown schematically in fig. 1. Heavy particles (^{12}C) were detected at 5° – 20° with a fixed detector-telescope (HI) consisting of a gas-ionization chamber (ΔE) and a Si position-sensitive E-detector (PSD). Alpha-particles were detected by other two Si detector-telescopes (α_0 and α_1) consisting of PSD-ΔE and E detector and a Si PSD (α_2) on a movable arm in the opposite side to the HI-detector with respect to the beam direction. By rotating the arm twice, angular regions of -8° – -50° and -100° – -152° for α-particles were covered.

For the process (i) and (iv) in chapter 1, the ^{12}C- particles are emitted mainly around beam direction and the α-particles from the target nucleus are emitted up to the backward angle region. The HI-detector was set across the beam direction so as to detect ^{12}C- particles as forward as possible (up to 5°), and thus incident beams were stopped with a Faraday-cup in front of the detector. Alpha-particles emitted in a wide angular region were detected by the three α-detectors. For the process (ii), unstable $^{16}O^*$-particles are emitted around beam direction with a velocity

much larger than the relative velocity between ^{12}C- and α-particles decaying from the $^{16}O^*$-particles. Therefore the ^{12}C- and α-particles are emitted mainly at forward angles and on opposite sides of the beam. By detecting ^{12}C- and α-particles with HI-detector and α_0- and α_1-detectors, most of $^{16}O^*$-particles were observed at forward angles covering 0° . For the process (iii), the α-particles in the primary process and the ^{12}C-particles decaying from the residual $^{20}Ne^*$-particles were detected by α_0- and HI-detectors, respectively. Because of the rather large center-of-mass velocity of the $^{20}Ne^*$-particles, the ^{12}C- particles are emitted mainly at forward angles. Therefore, most of ^{12}C- particles decaying from $^{20}Ne^*$-particles were detected.

For the calibration of the detection angles, two masks consisting of a copper wire of 0.5 - 1 mm diameter were placed in front of each PSD. The energy calibration was performed by using ^{12}C-particles scattered elastically. The absolute magnitudes of the cross sections were obtained by using the measured target thickness and the integrated beam charge. The absolute cross sections of elastic scattering in the singles measurement were in good agreement with those taken by Kubono *et al.*[22] Energy, angle, and absolute value of cross sections in the laboratory frame were determined within 500 keV, 0.3° , and 20 %, respectively.

Signals of energy-loss and position in the detectors and of timing between HI- and α-detectors, time-to-amplitude converter (TAC), were stored on magnetic tapes event by event through the interface Raw Data Processor[23] . The off-line analysis was performed in three steps as shown in fig. 2.

At the first step, only C–α coincident events were selected by the requirement of particle identification. For the detector telescopes (HI, α_0 and α_1), particle identification was performed by ΔE– and E–signals (fig. 3). Because of the lowest three-body $|Q|$–value[24] of the $^{12}C_{g.s.}+\alpha+^{8}Be_{g.s.}$ channel, other channels such as $^{13}C+\alpha+^{7}Be$ or $^{12}C+p+^{11}B$ associated with carbon isotopes and/or light particles could be rejected by selecting the Q–value in the next step. Therefore, in the procedure of particle identification, it was not necessary to distinguish carbon isotopes and also α–particles from other light particles. Coincidence events with α_2–detector (E–detector only) and events without E–signals of α_0– or α_1–detector were also stored for the next step of the analysis. These selected events were stored on magnetic tapes with flags of true/accidental coincidence by TAC analysis (fig. 4). As a result, most part of undesired events was rejected (*e.g.* about 1.6×10^{6} events were selected out of 10×10^{6} in the live data at 90 MeV).

Next, for each event selected in the first step, the three-body Q–value was calculated by using energy and position information of the detector. Here, energy loss in the target and the window of the gas counter was taken into account. Figure 5 shows a typical Q–value spectrum at 90 MeV. Peaks in the Q–value spectra correspond to final channels of the reaction as indicated in fig. 5. In the following procedure of the data reduction, only events of the peak which correspond to the $^{12}C_{g.s.}+\alpha+^{8}Be_{g.s.}$ final channel indicated as "Q_{ggg}" in fig. 5 were analyzed. As mentioned before, although the particle identification in the first step was

not clear and no particle identification was made for α_2 and α_0 and α_1 without E-signal, the other final channels such as $^{13}C+\alpha+^{7}Be$ or $^{12}C+p+^{11}B$ have been excluded by selecting the Q-value.

The selected events were stored on a disk and used for further kinematical calculations in the final step of the data reduction described in the next chapter.

CHAPTER 3

Results and discussion

This chapter consists of three sections corresponding to three problems (1)–(3) presented in chapter 1. In section 1, contributions of the four processes with different intermediate channels (i)–(iv) discussed in chapter 1 are estimated. In section 2, the coincidence cross sections of (i) and (ii) (inelastic scattering and α-transfer) are presented in a form of double-differential cross sections and discussed in terms of a DWBA analysis. Then, in section 3, evidence of the interference effect between two intermediate channels (i) and (ii) is discussed.

SECTION 1. CROSS SECTIONS OF VARIOUS INTERMEDIATE CHANNELS

Excited states in the intermediate channels of sequential processes (i) – (iii) are to be observed as resonant states consisting of two particles in the final channel. Therefore, in order to identify these intermediate channels (i) – (iii), spectra for relative energies between any pair out of three particles in the final channel were examined. Typical examples are shown in fig. 6 for the incident energy of 110 MeV. Horizontal axes in figs. 6(a) and (b) represent the relative energies between ^{12}C and α ($E_{1\text{-}2}$), and α and ^{8}Be ($E_{2\text{-}3}$), respectively. (Hereafter, ^{12}C–, α–, and ^{8}Be–particles in the final channel are denoted as 1, 2, and 3, respectively.) There are seen in fig. 6 four and two sharp peaks

which may correspond to the α-transfer to the discrete states of $^{16}O^*$ and to the inelastic excitation of the $^{12}C^*$-nuclei, respectively. The excitation energies observed for these peaks are 10.4, 14.7, 16.3, and 20.9 MeV for $^{16}O^*$ and 9.6 and 14.1 MeV for $^{12}C^*$, respectively. Note that the excitation energy is obtained by adding the particle-threshold energy to the relative energy. These peaks were also observed at other incident energies. It should be noted that these relative-energy spectra are alternative representations of the same data. Therefore, not all structures in a relative-energy spectrum of the particles j and k correspond to the excited states $(j+k)^*$ composed of particles j and k. This fact can be seen more clearly in a two-dimensional scatter plot as shown in figs. 7(a) and (b) plotted for the incident energy of 90 and 110 MeV, respectively. Horizontal and vertical axes in fig. 7 represent the relative energies $E_{2\text{-}3}$ and $E_{1\text{-}2}$, respectively. States consisting of particle j and k are identified by the presence of locus with $E_{j\text{-}k}=const.$ in the scatter plot. There are four loci of $E_{1\text{-}2}=const.$ and two of $E_{2\text{-}3}=const.$ which indeed correspond to the sharp peaks in fig. 6(a) and (b), respectively. Comparing fig. 6 with fig. 7, it is seen immediately that a bump centering around $E_{2\text{-}3}$=34 MeV in fig. 6(b) cannot be attributed to the highly excited continuum states of the $^{12}C^*$-nucleus, but is due to discrete states of the $^{16}O^*$-nucleus.

The scatter plot in fig. 7 is a kind of Dalitz-plot as described in appendix A in detail. In other words, the relative energy between ^8Be and ^{12}C ($E_{3\text{-}1}$) as well as $E_{1\text{-}2}$ and $E_{2\text{-}3}$ is shown in the scatter plot. The value of $E_{3\text{-}1}$ is represented by a

distance from the axis with a gradient of -3/4 as indicated in fig. 7. If the ^{8}Be-transfer process populating ^{20}Ne*-states (process (iii)) has comparable cross sections to the inelastic scattering or α-transfer process, there should be loci with a gradient of -3/4. Such loci could not be observed at any incident energy of the present experiment. It should be noted that α-particles are detected up to angles as forward as 7 degrees, where large cross section of direct ^{8}Be-transfer process is expected, if any. This observation suggests that the ^{8}Be-transfer process contributes only a small part of the cross sections of the reaction leading to the $^{12}C_{g.s.}+\alpha+^{8}Be_{g.s.}$ final channel. This fact agrees with arguments that the massive-cluster transfer processes have not been observed in the direct-like process for systems of light-heavy nuclei like $^{16}O+^{12}C$ at incident energies higher than 8 MeV/nucleon[13-16].

The non-sequential (direct) breakup process is to be identified in the scatter plot as events showing no locus with constant relative energy corresponding to the definite resonant state of either pair of particles out of the three. As seen in both the scatter plot and the relative-energy spectrum such as fig. 6(a), the non-sequential breakup process contributes at most on the level of underlying background yields in the relative-energy spectra. Accordingly, the non-sequential breakup process seems to have by far less yields than the sequential (α-transfer or inelastic scattering) process in the present experiment. This is consistent with recent studies[16-19] of the breakup process in light-heavy-ion reactions, which show that the

sequential processes dominate the non-sequential ones.

It was found that by integrating the yields of the loci in the scatter plot (four for $^{16}O^*$ and two for $^{12}C^*$) the $^{16}O^*+^8Be$ and $^{12}C+^{12}C^*$ channels account for more than 80 % of the cross section of the $^{12}C+^{12}C \rightarrow ^{12}C_{g.s.}+\alpha+^8Be_{g.s.}$ reaction (in the laboratory frame).

SECTION 2. DOUBLE-DIFFERENTIAL CROSS SECTIONS OF $^{16}O^*+^8Be$ AND $^{12}C+^{12}C^*$ CHANNELS

As described in section 1, the sequential processes through $^{16}O^*+^8Be$ and $^{12}C+^{12}C^*$ intermediate channels have dominant yields in the $^{12}C+^{12}C \rightarrow ^{12}C_{g.s.}+\alpha+^8Be_{g.s.}$ reaction. In this section, the coincidence cross sections for these channels are presented and discussed in detail. The coincidence cross sections for sequential processes are expressed in a form of double-differential cross sections[6,7] $d^2\sigma/d\Omega_{i-jk}d\Omega_{j-k}$ which consists of the angular distributions of the primary process and angular correlation function of the decaying process (see eq. (C5) in appendix C). Here, Ω_{i-jk} and Ω_{j-k} ($(i,j,k)=(3,1,2)$ for α-transfer or (1,2,3) for inelastic scattering) denote the solid angles associated with the primary process and decaying process in the recoil center-of-mass system[24], respectively. In the present in-plane correlation experiment, the double-differential cross sections are of a function of two polar angles θ_{i-jk} and θ_{j-k} corresponding to Ω_{i-jk} and Ω_{j-k}, respectively. These angles are schematically shown in fig. 8. The experimental double-differential cross sections were analyzed in terms of DWBA

formalism.

2.1. Experimental double-differential cross sections

The events from a sequential process were selected by gating on the corresponding locus in the scatter plot. For the selected events, the angles θ_{i-jk} and θ_{j-k}, azimuthal acceptance of detectors, and Jacobian of the transformation between the laboratory and recoil-center-of-mass system were calculated event by event. Then, these events were stored in an array consisting of meshes for θ_{i-jk} and θ_{j-k} (3 degrees in this analysis). Correction due to the low-energy threshold and the geometry of the detectors were taken into account. Detail procedure is presented in Appendix B.

Figures 9, 10, and 11 show the double-differential cross sections of the α-transfer processes ($^{12}C+^{12}C\rightarrow^{16}O^{*}(\rightarrow^{12}C+\alpha)+^{8}Be$) at incident energies of 90, 110, and 140 MeV, respectively. In these figures, the horizontal axis represents the decay angle ($\theta_{1\text{-}2}$) of the ^{12}C- particle in the rest frame of $^{16}O^{*}$-particle with respect to the direction of the momentum of the $^{16}O^{*}$-particle in the total center-of-mass frame (see fig. 8 also). Since the double-differential cross sections are proportional to the angular correlation functions which are usually used in the correlation experiments (defined by (C5) and (C6) in appendix C), they can be called (angular) correlation patterns. The angle of the primary process ($\theta^{c.m.}(^{16}O^{*})=\theta_{3\text{-}12}-180^{\circ}$) is shown at the middle column for each correlation pattern (1.5° , 4.5° , *etc.*). The angular

distribution of the primary process $^{12}C+^{12}C \rightarrow ^{16}O^*+^{8}Be$ can be obtained by integrating the correlation pattern over the solid angle ($\Omega_{1\text{-}2}$) in the rest frame of $^{16}O^*$.

The correlation patterns at $\theta^{c.m.}(^{16}O^*)=0^\circ$ show oscillations proportional to $|P_J|^2$ where J is spin of the $^{16}O^*$-states[12]. Here, P_J is the Legendre polynomial of order J. By fitting the correlation patterns with $|P_J|^2$ the J^π-values of the $^{16}O^*$-states were assigned to be 4^+, 5^-, 6^+, and 7^- for the states at the excitation energy of 10.4, 14.7, 16.3, and 20.9 MeV, respectively. These states have significant $^{12}C_{g.s.}$-α cluster configurations and large α-decay widths, and have been also observed selectively at lower incident energy[8] or in the $^{12}C(^{6}Li,d)^{16}O^*$ reaction[10].

When the angle of the primary process $\theta^{c.m.}(^{16}O^*)$ increases, the pattern changes its shape little but shifts in the decay angle $\theta_{1\text{-}2}$ linearly with $\theta^{c.m.}(^{16}O^*)$ (see fig. 12 for an example). Such a phenomenon also has been reported in other particle-γ or particle-particle correlation measurements[6,7,10,11,25,26]. As shown in appendix C (see eq. (C6)), the fact that the angular correlation patterns show characteristic oscillations even at angles $\theta^{c.m.}(^{16}O^*)\neq 0^\circ$ suggests that the mixing of the magnetic sub-states is not so strong.

Figures 13, 14, and 15 show the double-differential cross sections of the inelastic scattering processes ($^{12}C+^{12}C \rightarrow ^{12}C+^{12}C^*(\rightarrow\alpha+^{8}Be)$) at 90, 110, and 140 MeV, respectively. The presentation of these figures is identical to that of figs. 9-11 with the change of the notations ($\theta_{1\text{-}2} \rightarrow \theta_{2\text{-}3}$,

$\theta^{c.m.}(^{16}O^*) \rightarrow \theta^{c.m.}(^{12}C) = \theta_{1\text{-}23}$). The observed range of the correlation patterns was limited due to the absence of an α-detector at 50° – 100°. Contrary to the α-transfer case, it is noticed that the angular correlation patterns have less characteristic oscillations. Since the HI-detector didn't cover the angular region more forward than 5 degrees, angles of the primary inelastic scattering detected were more backward than those of the α-transfer, where $^{16}O^*$-particles were observed in the very forward angular region between the HI-detector and the α_0- and α_1-detectors. Since the correlation patterns at $\theta^{c.m.}(^{12}C) = 0°$ were not observed, spins and parities of the $^{12}C^*$-states could not be assigned model-independently. Therefore, they were assumed to be well-known 3^- and 4^+ states which have the same excitation energies as the observed (9.6 and 14.1 MeV).

2.2. DWBA analysis of double-differential cross sections

In order to understand the reaction mechanism of α-transfer and inelastic scattering processes, calculations based on a one-step finite-range DWBA formalism were carried out. The DWBA amplitudes for the primary processes were calculated by the code TWOFNR[27], and the double-differential cross sections were calculated by using resultant DWBA amplitudes (see appendix C).

For the α-transfer, the optical-model parameters used in the calculation are shown in table 1. The parameters were taken from the analyses of elastic scatterings of $^{12}C+^{12}C$ [22] and $^{9}Be+^{16}O$ [28] (instead of $^{8}Be+^{16}O$). The wave function of the ^{12}C- nucleus in the

initial channel was calculated on the assumption that the ^{12}C- nucleus has a cluster structure composed of an α-particle and a ^{8}Be-nucleus bound by a Woods-Saxon potential. The potential depth was determined to reproduce the binding energy (7.367 MeV). This potential was also used as the interaction potential of the reaction, as usually done in the post-form DWBA. As for the unbound states of the $^{16}O^{*}$-nucleus in the final (intermediate) channel, it is difficult to incorporate the unbound wave function in the calculation code. Therefore, by calculating the *T*-matrices for the bound-state wave functions with different binding energies, the binding-energy dependence of *T*-matrix is obtained, and then the *T*-matrix is extrapolated to the unbound states in the $^{16}O^{*}$-nucleus. By using the extrapolated *T*-matrix, the double-differential cross sections were evaluated.

Solid lines in figs. 9-11 show the results of the calculation. Only one normalization parameter was used for each transition. Rather good agreements with the experimental data, not only in the correlation functions but also in the angular distributions of the primary process, are obtained except for the region of $\theta_{1\text{-}2}$=180° -230° in fig. 9(a) (these disagreements will be discussed in section 3). Especially, the calculation reproduces well the shift of the correlation patterns. It was found that the absolute magnitudes of the DWBA cross section depended much on the distorting potential, whereas the correlation patterns did not.

To understand the shift of the correlation patterns the radial integrals of the DWBA calculation were examined (see appendix C). Figure 16(a) shows the radial integrals $I^{l}_{bL_a}$ of the

$^{12}C+^{12}C \rightarrow ^{16}O^*(6^+)+^{8}Be$ reaction at 90 MeV, where L_a and L_b represent the orbital angular momenta of the initial and final channels, respectively, and the spin of the $^{16}O^*$-state J is 6. It is shown that the contribution from $L_a=L_b+J$ terms (aligned terms) dominate the others and that L-distribution of $I^J_{L_bL_a}$ has a sharp peak centered at the grazing angular momentum ($L_a\sim22$ and $L_b\sim16$). This tendency didn't depend on the distorting potentials, and was also seen for the other $^{16}O^*$-states and the other incident energies. These characteristics of the radial integrals are determined mainly by the simple kinematical matching conditions rather than by the detailed dynamics of the reaction such as shape or depth of potentials. As described in detail in appendix C, in the case where the kinematical matching conditions play an important role, the shift of pattern from that at $\theta^{c.m.}(^{16}O^*)=0^\circ$ can be approximated as $-((L_{gr.}+1)/(J+1))\theta^{c.m.}(^{16}O^*)$, where $L_{gr.}$ denotes the grazing angular momentum in the initial channel. For the case of the $^{16}O^*(6^+)$-state, since $L_{gr.}\sim22$ at 90 MeV and $J=6$, the shift predicted is about $-(23/7)\theta^{c.m.}(^{16}O^*)$. This indeed agrees with the observation as shown in fig. 12.

For the inelastic scattering process, the collective form-factor and the same distorting potential as in the initial channel for the α-transfer were used. Dashed lines in fig. 15 show the results of the calculation.

As compared with the α-transfer, agreement with the experimental data is rather poor. If the results of the calculation are normalized at the forward angle of $\theta^{c.m.}(^{12}C)$, they underestimate the data at backward angles. In other words, the

calculation predicts too steep angular distributions of the primary inelastic scattering process. The calculated correlation patterns (dashed lines) are less oscillatory than those for the α-transfer (compare fig. 15(a) with fig. 9(d)). This agrees with the trend of the experimental results but the experimental patterns seem to be still more structureless than the calculated ones.

In order to investigate the reason why less oscillatory correlation patterns are predicted by the calculation for the inelastic scattering, the radial integrals were examined in the same manner as the α-transfer process. Figures 17(a) and (b) show the radial integrals and the sub-state populations, respectively, of the $^{12}C+^{12}C \rightarrow ^{12}C+^{12}C^*(4^+)$ reaction at 140 MeV. In comparison with the α-transfer case (fig. 16(a)), the $L_a=L_b+J-2$ terms are as large as the $L_a=L_b+J$ terms. This is due to the linear momentum mismatch in the inelastic scattering process. Therefore, the correlation patterns cannot be approximated by the sum only of p_J^J and $p_{\bar{J}}^J$ (see eq. (C5) in appendix C). Because of the coherent summation over various terms of the sub-state populations p_J^J, the double-differential cross sections depend on the relative phases of the radial integrals of $L_a=L_b+J$ and $L_a=L_b+J-2$ through p_J^J and thus on the distorting potentials. In fact it was found that the DWBA calculations were sensitive to the distorting potentials and better agreement with data has been obtained with a weak imaginary potential (about half depth of W as shown in table 1). Solid lines in figs. 13-15 show the results of the calculation.

Here, the following comment on the change of the distorting

potential can be made. In the $^{12}C+^{12}C$ system, the inelastic transition to the low-lying collective state (2^+; 4.44 MeV) is so strong that the coupling effects with the 2^+-state should be taken into account in the elastic scattering and the inelastic scatterings to the 3^- and 4^+-states. In one-step calculations such coupling effects are not treated explicitly. But they can be included phenomenologically in the potentials as dynamic polarization potentials[2]. Such dynamic polarization potentials for various states may not always be the same. In our calculation, better agreement with the data was achieved with the distorting potential with weaker imaginary part than that determined to fit the elastic data. Therefore, it may be suggested that the dynamic polarization potential in the inelastic scattering is different from that included in the optical potential for the elastic scattering.

2.3. Absolute values of the cross sections

In this subsection, we discuss the absolute values of the cross section of the α-transfer and the inelastic scattering processes and their energy dependence. The reaction cross section of each process was deduced by integrating the experimental correlation patterns. In the integration the azimuthal angular distributions of the correlation patterns (off-plane correlations) were assumed to be those obtained by the DWBA calculation. Dots with dashed lines and solid lines in fig. 18 show the integrated cross sections of the experimental data and of the DWBA.

calculation, respectively.

In the DWBA calculation for the α-transfer process (fig. 18(a)), both the partial width and the spectroscopic factor were set to unity for all transitions. The calculation reproduces the experimental value within factor of 2-4 at all three incident energies. Note that the absolute magnitude predicted by the DWBA calculation strongly depends on the amplitude of the tails of the wave functions of ^{12}C- and $^{16}O^*$-nuclei because of the localization of the form-factors around the surface region. Therefore, the wave functions used in our calculation are rather reasonable. However, in order to discuss the absolute magnitudes more quantitatively *i.e.* to deduce spectroscopic factors and/or partial width, more realistic wave functions are needed which take into account the unbound nature and clustering features. In fig. 18(a) it is noticed that the observed cross sections decrease with increasing the incident energy, whereas the calculation tends to predict less steep energy dependence than the experimental data. Such a tendency has been also reported for other heavy-ion induced transfer reactions[29,30]. Even when one took wave functions of the $^{16}O^*$-nucleus with a larger tail, which simulates the unbound nature, the energy dependence and sub-state populations changed little, although the absolute cross sections became much larger. As mentioned in ref. 1, the energy dependence of the calculation may be improved by taking into account the effect of multi-step or coupling with the low-lying collective states.

For the inelastic scattering, except for the transition to the 3^--state at the incident energy of 90 MeV, the calculation

reproduces the energy dependence rather well as shown in fig. 18(b). Contrary to the α-transfer process, the observed cross sections do not change with the incident energy. The partial widths were set to unity, and the deformation parameters β_3=0.25 and β_4=0.21 for the 3^-- and 4^+-states, respectively, were obtained by normalizing the data at the incident energy of 140 MeV. However, it is necessary to perform a coupled-channel calculation in order to estimate the deformation parameters correctly, because our calculation does not take into account the coupling with the 2^+-state explicitly.

Here, the absolute cross sections in the present work are compared with those of other (final) channels around 10 MeV/nucleon (93.8 MeV[31]). Table 2 shows the integrated cross sections of the present work together with those of the elastic scattering, the inelastic scatterings to the low-lying 2^+-states and the few-nucleon transfer reactions. It is noticed that the α-transfer channels have larger cross sections than either of the one- or two-nucleon transfer channels. This is probably due to the significant α-cluster structures of ^{12}C- and ^{16}O*-nuclei.

SECTION 3. INTERFERENCE EFFECT

We come back to the scatter plot (fig. 7) presented in section 1. It is noticed that there are several crossing points of the loci corresponding to the excited states of both ^{12}C*- and ^{16}O*-nuclei. In other words, at the crossing points, both of the α-transfer and the inelastic scattering processes contribute to

the same final channel. If these different processes with different intermediate channels are independent, the cross sections at the crossing point are to be a simple sum of the cross sections of individual processes. In this section, we examine whether the cross sections at the crossing point are of a simple sum or not, and discuss a possible interference effect.

At first, a locus of $E_{1\text{-}2}=const.$ in the scatter plot is considered. Events on that locus are also represented as the double-differential cross sections of an α-transfer process. At a crossing point with the locus of $E_{2\text{-}3}=const.$ where both $E_{1\text{-}2}$ and $E_{2\text{-}3}$ have definite values, all of the relative velocities $v_{1\text{-}2}$, $v_{2\text{-}3}$, and $v_{3\text{-}1}$ are determined uniquely. Therefore, the shape of the triangle ijk in fig. 8 ($(i,j,k)=(3,1,2)$ in this case) whose sides are equal to the relative velocities $v_{1\text{-}2}$, $v_{2\text{-}3}$, and $v_{3\text{-}1}$ is fixed, and then the decay angle $\theta_{1\text{-}2}$ is fixed independently of the angle $\theta_{3\text{-}12}$ ($\theta^{c.m.}_{2}(^{16}O^{*})$) of the primary α-transfer process. In other words, to specify $E_{2\text{-}3}$ on the locus of $E_{1\text{-}2}=const.$ in the scatter plot is equivalent to fix the decay angle $\theta_{1\text{-}2}$ (not $\theta^{c.m.}(^{16}O^{*})$) in the double-differential cross sections of the α-transfer process (see eq. (A3) in appendix A). For example, on the locus of $E_{1\text{-}2}$=13.5 MeV ($^{16}O^{*}(7^{-})$) at 90 MeV (fig. 7(a)), the crossing points with the loci $E_{2\text{-}3}$=2.3 MeV($^{12}C^{*}(3^{-})$) and 7 MeV($^{12}C^{*}(4^{+})$) correspond to the regions of $\theta_{1\text{-}2}\sim200^{\circ}$ and 230° in the double-differential cross sections (fig. 9(a)), respectively, where the calculation underestimates the data considerably as mentioned in section 2. Reversely, starting from a locus of $E_{2\text{-}3}=const.$ which corresponds to the inelastic scattering, to specify $E_{1\text{-}2}$ on this locus is

equivalent to fix the decay angle $\theta_{2\text{-}3}$ (not $\theta^{c.m.}(^{12}C)$) in the double-differential cross sections of the primary inelastic scattering process (see eq. (A3') in appendix A). For example, on the locus of $E_{2\text{-}3}$=7 MeV($^{12}C^*(4^+)$) at 90 MeV, the crossing points with the loci $E_{1\text{-}2}$=9.6 MeV($^{16}O^*(6^+)$) and 13.5 MeV($^{16}O^*(7^-)$) respectively correspond to the regions of $\theta_{2\text{-}3}\sim310°$ and 285° in the double-differential cross sections of fig. 13(a), where two peaks deviating from the DWBA calculation are seen at all angle of the primary process $\theta^{c.m.}(^{12}C)$.

It should be noted that the shape of the triangle *ijk* is fixed by specifying a crossing point but the spatial direction of the triangle is not fixed. In other words, the cross section at a crossing point is of a function of the spatial direction of the triangle. In the in-plane correlation measurements, this direction is denoted by the angles $\theta^{c.m.}(^{16}O^*)$ ($\theta_{3\text{-}12}$) or $\theta^{c.m.}(^{12}C)$ ($\theta_{1\text{-}23}$). As seen from the velocity diagram there are simple relations between these angles. For example, at the crossing point of the loci $E_{1\text{-}2}$=13.5 MeV and $E_{2\text{-}3}$=7 MeV at 90 MeV, the relation is calculated as follows:

$$\theta_{1\text{-}23} = \theta_{3\text{-}12} + 201° \qquad (1)$$

or

$$\theta^{c.m.}(^{12}C) = \theta^{c.m.}(^{16}O^*) + 21° \quad . \qquad (1')$$

Therefore, we discuss the cross sections at a crossing point as a function of $\theta^{c.m.}(^{16}O^*)$ or equivalently of $\theta^{c.m.}(^{12}C)$.

Now we discuss how to evaluate the cross sections of different processes at the crossing points. At a crossing point

of loci $E_{1\text{-}2}=E^{0}_{1\text{-}2}$ and $E_{2\text{-}3}=E^{0}_{2\text{-}3}$, one can formally consider the following three types of the cross sections:

(A) = the observed cross section.

(B) = the cross section only of the α-transfer process.

(C) = the cross section only of the inelastic scattering process.

If there is no interference effect, (A) is always equal to (B) + (C). Note that these cross sections should be estimated in a common coordinate system. In the section 2, we took two different coordinate systems $(\theta^{c.m.}(^{16}O^{*}),\theta_{1\text{-}2})$ and $(\theta^{c.m.}(^{12}C),\theta_{2\text{-}3})$ for the α-transfer and the inelastic scattering processes, respectively. For simplicity, we call these coordinate systems (b) and (c). The systems (b) and (c) are natural and thus convenient for the estimation of (B) and (C), respectively. They can be expressed as follows:

$$B_b(\theta^{c.m.}(^{16}O^{*})) \equiv \text{(B) in system (b)}$$

$$= \int_{E^{0}_{2\text{-}3}-\Delta E_{2\text{-}3}}^{E^{0}_{2\text{-}3}+\Delta E_{2\text{-}3}} \frac{d^2\sigma}{d\Omega_{3\text{-}12}d\Omega_{1\text{-}2}}(\theta^{c.m.}(^{16}O^{*}),\theta_{1\text{-}2}(E_{2\text{-}3});E^{0}_{1\text{-}2})\,|_{\alpha\text{-}trans.}\frac{\partial\theta_{1\text{-}2}}{\partial E_{2\text{-}3}}dE_{2\text{-}3} \qquad (2)$$

$$C_c(\theta^{c.m.}(^{12}C)) \equiv \text{(C) in system (c)}$$

$$= \int_{E^{0}_{1\text{-}2}-\Delta E_{1\text{-}2}}^{E^{0}_{1\text{-}2}+\Delta E_{1\text{-}2}} \frac{d^2\sigma}{d\Omega_{1\text{-}23}d\Omega_{2\text{-}3}}(\theta^{c.m.}(^{12}C),\theta_{2\text{-}3}(E_{1\text{-}2});E^{0}_{2\text{-}3})\,|_{inel.}\frac{\partial\theta_{2\text{-}3}}{\partial E_{1\text{-}2}}dE_{1\text{-}2}\ , \qquad (3)$$

where the suffices of $\alpha\text{-}trans.$ and $inel.$ denote the double-differential cross sections only of the α-transfer and the inelastic scattering, respectively, and $\Delta E_{2\text{-}3}$ and $\Delta E_{1\text{-}2}$ denote the

widths of loci. For comparison of (A) with (B)+(C), B_b and C_c is transformed to the system (c) and (b), respectively, and the magnitude of (A) in the two coordinate systems is expressed:

$$B_c(\theta^{c.m.}(^{12}C)) \equiv \text{(B) in system (c)} = JB_b \ , \tag{4}$$

$$C_b(\theta^{c.m.}(^{16}O^*)) \equiv \text{(C) in system (b)} = (1/J)C_c \ , \tag{5}$$

$$A_b(\theta^{c.m.}(^{16}O^*)) \equiv \text{(A) in system (b)}$$

$$= \int_{E^0_{2-3}-\Delta E_{2-3}}^{E^0_{2-3}+\Delta E_{2-3}} \frac{d^2\sigma}{d\Omega_{3-12}d\Omega_{1-2}}(\theta^{c.m.}(^{16}O^*), \theta_{1-2}(E_{2-3}); E^0_{1-2})\,|_{obs.} \frac{\partial\theta_{1-2}}{\partial E_{2-3}} dE_{2-3} \ , \tag{6}$$

$$A_c(\theta^{c.m.}(^{12}C)) \equiv \text{(A) in system (c)}$$

$$= \int_{E^0_{1-2}-\Delta E_{1-2}}^{E^0_{1-2}+\Delta E_{1-2}} \frac{d^2\sigma}{d\Omega_{1-23}d\Omega_{2-3}}(\theta^{c.m.}(^{12}C), \theta_{2-3}(E_{1-2}); E^0_{2-3})\,|_{obs.} \frac{\partial\theta_{2-3}}{\partial E_{1-2}} dE_{1-2}$$

$$= JA_b \ , \tag{7}$$

where J denotes the Jacobian of the coordinate transformation from system (b) to system (c), and suffix *obs.* denotes the observed double-differential cross sections. Note that the $\theta^{c.m.}(^{16}O^*)$- dependence in the above quantities is equivalent to the $\theta^{c.m.}(^{12}C)$- dependence because of the linear relation between $\theta^{c.m.}(^{16}O^*)$ and $\theta^{c.m.}(^{12}C)$ as mentioned before (eq. (1')).

Since it is confusing and complicated a little to discuss the comparison of (A) and (B)+(C) by the quantities depending on the

coordinate system, we introduce a ratio k of (A) to (B)+(C) which is independent of the choice of the coordinate system. Namely, k is defined as follows:

$$k(\theta^{c.m.}(^{16}O^*) \text{ or } \theta^{c.m.}(^{12}C)) = A_b/(B_b+C_b) \qquad \text{(in system (b))}$$

$$= A_c/(B_c+C_c) \qquad \text{(in system (c))}$$

$$= \left(\frac{B_b}{A_b} + \frac{C_c}{A_c}\right)^{-1}, \qquad (8)$$

where the relation of $C_c/A_c=C_b/A_b$ or $B_c/A_c=B_b/A_b$ is used. It should be noted that B_b/A_b and C_c/A_c can be estimated in the system (b) and (c), respectively, and then the Jacobian J need not be calculated. Since the cross sections (A), (B) and (C) are of a function of $\theta^{c.m.}(^{16}O^*)$ (or $\theta^{c.m.}(^{12}C)$), k is also of a function of these angles. However, if there is no interference effect, k is always to be unity independently of these angles. In other words, the interference effect is checked by examining the $\theta^{c.m.}(^{16}O^*)$- dependence of k.

The k-value for the observed crossing points is estimated. For B_b and C_c we used the results of the DWBA calculation normalized at regions except for the crossing point (solid lines in figs. 9-11 and 13-15). The quantities A_b and A_c were estimated from the experimental double-differential cross sections by using eqs. (6) and (7), respectively. As an example, we discuss the crossing point of the $^{16}O^*(7^-)+^8Be$ and the $^{12}C+^{12}C^*(4^+)$ channels at 90 MeV. At this point, $\theta^{c.m.}(^{12}C)$ is related to $\theta^{c.m.}(^{16}O^*)$ as in eq.

(1'). Figure 19(a) shows k-values for this crossing point as a function of the angle $\theta^{c.m.}(^{16}O^*)$ (or $\theta^{c.m.}(^{12}C)$ shown at the top of the figure). As seen in this figure, the k-value considerably deviates from unity and shows oscillations. Although the absolute magnitudes can be changed a little by changing the normalization factors in the estimation of B_b and C_c, the characteristic oscillation of k hardly depends on the normalization factors. This result shows that the cross sections at the crossing point cannot be explained by a simple sum of the individual cross sections of the α-transfer and the inelastic scattering processes. As shown in fig. 20, for the other crossing points $(^{16}O^*(6^+)-^{12}C^*(4^+)$ and $(^{16}O^*(7^-)-^{12}C^*(3^-))$ and those at other incident energies $(^{16}O^*(7^-)+^{12}C^*(4^+)$ at 110 and 140 MeV), the k-value shows similar oscillatory $\theta^{c.m.}(^{16}O^*)$- dependence and deviates from unity. Therefore, it is concluded that evidence of the interference effect between two different processes has been found in the kinematical region where different processes can contribute to the same three-body final channel at the same time.

In order to understand the oscillatory character of the k-value, the interference effect is discussed in terms of the DWBA T-matrices which are calculated independently for the α-transfer and the inelastic scattering. The quantities of A_b and A_c are expressed theoretically as follows[21]:

$$A_b \propto |T_b(^{16}O^*+^{8}Be;\ \theta^{c.m.}(^{16}O^*), \theta^{0}_{1-2}(E^{0}_{2-3}))$$

$$+\sqrt{1/J}\,T_c(^{12}C+^{12}C^*;\ \theta^{c.m.}(^{12}C), \theta^{0}_{2-3}(E^{0}_{1-2}))|^2, \qquad (9)$$

$$A_c \propto |T_c(^{12}C+^{12}C^*;\ \theta^{c.m.}(^{12}C), \theta^0_{2-3}(E^0_{1-2}))$$

$$+\sqrt{J}T_b(^{16}O^*+^8Be;\ \theta^{c.m.}(^{16}O^*), \theta^0_{1-2}(E^0_{2-3}))|^2, \qquad (10)$$

where the T_b and T_c are the T-matrices for the α-transfer and the inelastic scattering, respectively, obtained by the individual DWBA calculations. Using eqs. (8) - (10), the k-value is expressed as follows:

$$k = \left[\frac{|T_b|^2}{|T_b+(1/J)^{1/2}T_c|^2}+\frac{|T_c|^2}{|T_c+J^{1/2}T_b|^2}\right]^{-1}$$

$$= 1 + \frac{2}{r + r^{-1}}\cos\chi, \qquad (11)$$

where $r = |\sqrt{J}T_1/T_3|$ and χ is the phase difference between T_b and T_c. As an example, the quantities $2/(r+r^{-1})$ and χ were calculated for the crossing point of the $^{16}O^*(7^-)+^8Be$ and $^{12}C+^{12}C^*(4^+)$ channels at 90 MeV by using the individual DWBA calculations for the α-transfer and the inelastic scattering processes. It was found that the former quantity was almost constant, and thus the $\theta^{c.m.}(^{16}O^*)$- dependence of k-values was mainly attributed to that of the phase difference χ. Figure 19(b) shows calculated χ-values versus $\theta^{c.m.}(^{16}O^*)$. The phase difference χ shows an oscillatory behaviour with a similar period to that in k-value in fig. 19(a). This shows that the oscillatory behaviour of the k-values are qualitatively explained by the interference between the DWBA amplitudes for different processes. Note that the absolute

magnitude of χ is not determined since T_b and T_c are calculated independently. For further investigations of the interference effect, both of the T-matrices of the α-transfer and the inelastic scattering processes should be calculated in the same framework. Theoretical models which take into account the three-body aspect and thus describe different intermediate channels at the same time are required for quantitative understood for this interference effect.

CHAPTER 4

Summary and conclusions

In order to investigate the mechanism of the $^{12}C+^{12}C \rightarrow ^{12}C_{g.s.}+\alpha+^{8}Be_{g.s.}$ reaction, $^{12}C-\alpha$ coincidence measurements have been carried out in a wide angular range at 90, 110 and 140 MeV. Cross sections were deduced for all possible (intermediate) channels leading to the same three-body final channel: three intermediate channels ($^{12}C+^{12}C^*$, $^{16}O^*+^{8}Be$ and $\alpha+^{20}Ne^*$) and the non-resonant (direct) breakup process. In order to identify these processes, data were represented in a form of scatter plots which have coordinates of relative energies between three pairs of the particles in the final channel, as well as in a form of relative-energy spectra. Then, contributions from four possible intermediate channels have been evaluated:

(I) The inelastic transition to the $^{12}C^*$-states (3^- and 4^+) and the α-transfer to the $^{16}O^*$-states (4^+, 5^-, 6^+ and 7^-) of the intermediate channels $^{12}C+^{12}C^*$ and $^{16}O^*+^{8}Be$, respectively, account for most part of the cross section.

(II) The massive cluster- (^{8}Be-) transfer process leading to the $\alpha+^{20}Ne^*$ intermediate channel is not observed within the sensitivity of the experiment.

(III) The non-resonant (direct) breakup process contributes, at most, a few percent of the cross section.

The double-differential cross sections (angular distributions of the primary processes and the angular correlation patterns of the subsequent α-decay) for the $^{16}O^*+^{8}Be$ and $^{12}C+^{12}C^*$ intermediate

channels were obtained and analyzed in terms of a one-step DWBA. The following results were obtained:

(1) For the $^{16}O^{*}+^{8}Be$ channel, oscillatory angular correlation patterns were observed. It was found that the position of maxima and minima shifted linearly with the scattering angle of $^{16}O^{*}$. These data were reproduced well by the DWBA calculation assuming direct α-cluster transfer mechanism. It was also found that the shift of the patterns with the scattering angle of $^{16}O^{*}$ was determined by the kinematical matching conditions and approximated as a function mainly of the grazing angular momentum and the spin of the $^{16}O^{*}$-states.

(2) For the $^{12}C+^{12}C^{*}$ channel, less oscillatory angular correlation patterns than in the $^{16}O^{*}+^{8}Be$ case were obtained and reproduced by the DWBA calculation with conventional collective form-factors. Calculations with an imaginary potential weaker than that determined in the analysis of the elastic scattering data gave better agreement with the data. This may be related to the coupling effect to other channels such as the inelastic scattering leading to the 2^{+} state of the ^{12}C- nucleus. Less oscillatory patterns are ascribed to the linear momentum mismatch.

The angular correlation patterns of both the $^{16}O^{*}+^{8}Be$ and the $^{12}C+^{12}C^{*}$ channels were integrated. The integrated cross sections for the α-transfer process populating $^{16}O^{*}$-states (4^{+}, 5^{-}, 6^{+} and 7^{-}) decrease with increasing incident energy, whereas those for the inelastic excitation (3^{-} and 4^{+} states of $^{12}C^{*}$) do not change much with the incident energy. The DWBA calculation reproduced

the energy dependence of the integrated cross section rather well.

An interference effect between two different processes (α-transfer and inelastic scattering) was discussed in terms of the cross sections of the kinematical regions where two processes can participate. Such regions are represented by crossing points of loci in the scatter plot. The observed cross sections deviated from a simple sum of the cross sections of individual processes. This is an evidence of the interference effect between the α-transfer and the inelastic scattering processes. The deviation was explained qualitatively by the interference between DWBA *T*-matrices calculated independently for the two processes. For the quantitative description of the interference effect, it is necessary to calculate *T*-matrices for different processes in the same framework. Theoretical models which can treat various intermediate channels at the same time and also take into account the three-body aspects are required.

The highly excited and high spin states of ^{16}O populated in the $^{12}C+^{12}C$ reaction at $\sim$ 10 MeV/nucleon have been assigned unambiguously by $^{12}C-\alpha$ coincidence measurements in a wide angular range. Cross sections of these states have been reproduced quantitatively by one-step DWBA calculations assuming direct α-transfer. Disagreement between the data and the calculation has been explained by an interference between the α-transfer and the inelastic scattering processes. The method described here, investigating many competitive processes on an equal footing, may open up a new field of spectroscopy.

ACKNOWLEDGEMENT

I wish to express my sincere thanks to Prof. K. Katori, Prof. H. Ogata, Dr. T. Shimoda, Dr. T. Fukuda, and Mr. A. Sakaguchi for their help in the every stage of the present work. I thank to Mr. K. Ogura for his effort in the experimental stage. I wish to thank Prof. M. Igarashi for his kind explanation about his computer program (TWOFNR) and also to thank Dr. T. Motobayashi for his suggestions in the analysis.

I thank to Prof. S. Kobayashi and Dr. K. Takimoto for their helpful advice and encouragement throughout my graduate studies.

The experiment was performed at Research Center for Nuclear Physics (RCNP), Osaka University. I acknowledge the cyclotron crew and supporting staff of RCNP for their devoting efforts. The data reduction and analysis were performed by using FACOM M-180-IIAD at the computer center of RCNP.

APPENDIX A

Modified Dalitz-plot

In the reaction $P + T \rightarrow 1 + 2 + 3$ with a definite Q-value, the sum of the kinetic energy (E_i^c) of each particle ($i = 1 - 3$) in the center-of-mass system is conserved. In this case each event can be represented by a point X inside an equilateral triangle, when one notices that the sum of the distance (R_i) between X and each side of the triangle is constant, *i.e.* $\sum_{i=1}^{3} R_i$ is proportional to $\sum_{i=1}^{3} E_i^c \equiv E_{c.m.}^f$ (total center-of-mass energy in the final three-body channel). This idea was originally obtained by Dalitz[32] and thus such a plot is called as Dalitz-plot.

It is rather convenient, however, to see directly the relative energy E_{j-k} between particle j and k (or equivalently excitation energy of the composite particle $(j+k)$) in the case that each pair out of three particles forms many sharp resonant states. For this purpose, the following relation can be used:

$$\frac{m_2+m_3}{M}E_{2-3} + \frac{m_3+m_1}{M}E_{3-1} + \frac{m_1+m_2}{M}E_{1-2} = E_{c.m.}^f = const., \qquad (A1)$$

where m_i (i=1 - 3) denote the mass of particle i and $M = \sum_{i=1}^{3} m_i$. The derivation of eq. (A1) is easy when one notices the following relation:

$$\frac{M}{m_j+m_k}E_i^c + E_{j-k} = E_{c.m.}^f ,$$

$$((i,j,k)=(1,2,3),(2,3,1),(3,1,2)). \qquad (A2)$$

According to similar arguments as used for the Dalitz-plot, one can relate each event to a point X inside a triangle, the length of side of which is proportional to m_j+m_k (fig. 21). For example, in the case of the $^{12}C+^{12}C \rightarrow ^{12}C+\alpha+^{8}Be$ reaction, the ratio of the length of the side is 3:4:5, and thus the triangle becomes a right-angle one. We call such a plot as a modified Dalitz-plot. From the conservation of energy and momentum, it is found that all events are confined within the inscribed circle of the triangle whose radius is equal to $E^{f}_{c.m.}/2$. Note that the loci parallel to the side BC [AB, CA] in fig. 21 correspond to the events of the sequential process $1 + (2+3)^{*}$ [$(1+2)^{*} + 3$, $(3+1)^{*} + 2$] $\rightarrow 1 + 2 + 3$ with E_{2-3} [E_{1-2}, E_{3-1}] = $const.$

In the modified Dalitz-plot such as fig. 7, each event is specified only by the relative energies. Therefore, no information on the angles is given explicitly in the plot. We discuss angles implicitly expressed in the Dalitz-plot by using the velocity diagram (fig. 8). When a point in the plot is specified, the shape of the triangle ijk, defined by the relative velocities, is fixed as shown in fig. 8. Figure 8 also shows the notation of the angles which define completely the primary and subsequent processes. Because of the in-plane correlation measurement in our case, only two angles θ_{j-k} and θ_{i-jk} are considered. When the triangle ijk in fig. 8 is fixed, clearly the decay angle θ_{j-k} is fixed. Therefore, specifying the point in the modified Dalitz-plot is equivalent to fix the decay angle θ_{j-k}. For example, for the final channel of $^{12}C(1)+\alpha(2)+^{8}Be(3)$, the

relation between the decay angle and the relative energy is calculated as follows:

$$\cos\theta_{1\text{-}2} = \frac{E_{2\text{-}3} - (1/2)E^f_{c.m.}}{(E_{1\text{-}2}(E^f_{c.m.} - E_{1\text{-}2}))^{1/2}} \ , \tag{A3}$$

$$\cos\theta_{2\text{-}3} = \frac{E_{1\text{-}2} - (1/2)E^f_{c.m.}}{(E_{2\text{-}3}(E^f_{c.m.} - E_{2\text{-}3}))^{1/2}} \ . \tag{A3'}$$

These relations are used in section 3 of chapter 3.

For the triangle ijk fixed corresponding to the specific relative energies, however, the spatial direction of the triangle with respect to the beam direction is not yet fixed. This degree of freedom, the direction for the primary process, is truncated in the modified Dalitz-plot. In the double-differential cross section, which is complimentary to the modified Dalitz-plot, the direction of the primary process is given explicitly.

APPENDIX B

Formulation to obtain experimental double-differential cross sections

In this appendix, we present the details of procedure to obtain the experimental double-differential cross sections and Jacobian of coordinate transformation.

For the in-plane correlation measurement in our case, the procedure mentioned in section 2.1 of chapter 3 is described as following equation:

$$\frac{d^2\sigma}{d\Omega_{i-jk}d\Omega_{j-k}}(\theta^0_{i-jk},\theta^0_{j-k};E^0_{j-k},Q^0) = \frac{\partial(\phi_1,\phi_2)}{\partial(\phi_{i-jk},\phi_{j-k})}$$

$$\times\frac{Y(|E_{j-k}-E^0_{j-k}|\leqq\Delta E_{j-k},\ |Q-Q^0|\leqq\Delta Q,\ |\theta_{i-jk}-\theta^0_{i-jk}|\leqq\Delta\theta_{i-jk}/2,\ |\theta_{j-k}-\theta^0_{j-k}|\leqq\Delta\theta_{j-k}/2)}{\varepsilon BT\Delta\theta_{i-jk}\Delta\theta_{j-k}\Delta\phi_1\Delta\phi_2\sin\theta^0_{i-jk}\sin\theta^0_{j-k}}$$

$$(i,j,k) = \begin{cases}(1,2,3) & \text{for inelastic scattering}\\ (3,1,2) & \text{for } \alpha\text{-transfer}\end{cases} . \qquad (B1)$$

In eq. (B1), Y is the yield which satisfies the requirements described in the parentheses, B and T are amounts of beam and target, respectively. θ_{i-jk} and θ_{j-k} represent the angle of the particle i with respect to the beam axis in the total center-of-mass system and the angle of the particle j with respect to the recoil axis of the particle $(j+k)^*$, respectively. The definition of these angles is also shown schematically in fig. 8. $\Delta\theta_{i-jk}$ and $\Delta\theta_{j-k}$ are mesh sizes for the double-differential cross section (set to 3 degree in this analysis), $\Delta\phi_1$ and $\Delta\phi_2$ are azimuthal acceptance of detectors, and ε is the efficiencies in the recoil center-of-mass system due to finite thresholds of

energies deposited in the detectors and angular acceptance which are limited by the geometries of detectors and the masks mentioned in chapter 2. Figure 22 shows typical examples of the calculated efficiencies (ε). ($^{16}O^{*}(7^{-})+^{8}Be$ and $^{12}C+^{12}C^{*}(4^{+})$ at 90 MeV). The data reduction was performed in the angular regions where the efficiencies are greater than 0.5.

The Jacobian $\partial(\phi_1,\phi_2)/\partial(\phi_{i-jk},\phi_{j-k})$ is given as:

$$\frac{\partial(\phi_1,\phi_2)}{\partial(\phi_{i-jk},\phi_{j-k})} = \left[\frac{m_3}{M}\cdot\frac{E^0_{i-jk}E^0_{j-k}}{E'_1E'_2}\right]^{1/2}\cdot\frac{\sin\theta^0_{i-jk}\sin\theta^0_{j-k}}{\sin\theta'_1\sin\theta'_2}\ , \qquad (B2)$$

where $E'_1[\theta'_1]$ and $E'_2[\theta'_2]$ are laboratory energies [angles] of particle 1 (^{12}C) and 2 (α), respectively.

APPENDIX C

Characteristics of double-differential cross sections

In this appendix, we describe the double-differential cross sections for the sequential process, $A(a,b)B^{*}\rightarrow c+d$, in terms of DWBA amplitudes of the primary reaction. Then, the characteristics of the double-differential cross sections will be examined in heavy-ion reactions where kinematical matching conditions are important.

According to the DWBA formalism, the cross section of the reaction $A(a,b)B$ is written in the following form without spin-orbit force[33]:

$$\frac{d\sigma}{d\Omega_b} = \frac{\mu_a\mu_b}{(2\pi\hbar^2)^2}\frac{k_b}{k_a}\frac{2J_B+1}{(2J_A+1)(2s_a+1)}\sum_{j,m}\left|\sum_{l,s}A_{lsj}\beta_{sj}^{lm}\right|^2, \tag{C1}$$

where

$$(2l+1)^{1/2}\beta_{sj}^{lm}(k_b,k_a)$$

$$= \sum_{\substack{L_aL_b\\M_a}} i^{L_a-L_b-l}\langle L_b\ L_a\ m-M_a\ M_a\mid l\ m\rangle Y_{L_a}^{M_a*}(\theta_a,\varphi_a)Y_{L_b}^{m-M_a*}(\theta_b,\varphi_b)4\pi I_{L_bL_a}^{lsj}, \tag{C2}$$

$$I_{L_bL_a}^{lsj} = \frac{4\pi}{k_ak_b}\int r_a dr_a\int r_b dr_b\chi_{L_b}^{(b)}(k_b,r_b)F_{lL_bL_a}^{sj}(r_b,r_a)\chi_{L_a}^{(a)}(k_a,r_a). \tag{C3}$$

All notations in the equations are exactly the same as those in ref. 33. Using eq. (C1), when all particles in the initial and final channel have spin 0, the double-differential cross section of the reaction $A(a,b)B^{*}(J_B=J)\rightarrow c+d$ can be expressed as follows[11]:

$$\frac{d^2\sigma}{d\Omega_b d\Omega_c} = \frac{\Gamma_{c+d}}{\Gamma_{tot}} \frac{\mu_a \mu_b}{(2\pi\hbar^2)^2} \frac{k_b}{k_a} (2J+1) |A_J|^2 |\sum_m \beta^{Jm}(k_b, k_a) Y^{Jm}(\Omega_c)|^2$$

$$= \frac{\Gamma_{c+d}}{\Gamma_{tot}} \frac{d\sigma}{d\Omega_b}(\Omega_b) |\sum_m p^{Jm}(k_b, k_a) Y^{Jm}(\Omega_c)|^2, \qquad (C4)$$

where $p^{Jm} \equiv \beta^{Jm} / [\sum_m |\beta^{Jm}|^2]^{1/2}$ is the sub-state population parameter. In eq. (C4), Γ_{tot} and Γ_{c+d} are the total width of the the resonant state in the nucleus B^* and its decay width into $c+d$ channel, respectively.

When $k_a \times k_b$ and k_b are taken to be z- and x-axes, respectively, the double-differential cross section of (C4) is expressed for the in-plane correlation measurements as:

$$\frac{d^2\sigma}{d\Omega_b d\Omega_c} = \frac{\Gamma_{c+d}}{\Gamma_{tot}} \frac{d\sigma}{d\Omega_b}(\theta) W(\theta, \psi), \qquad (C5)$$

where

$$W(\theta, \psi) = |\sum_m p^{Jm}(\theta) Y^{Jm}(\frac{\pi}{2}, \psi)|^2$$

$$= |\sum_m p^{Jm}(\theta) (-1)^{(J-m)/2} e^{im\psi} [\frac{(J+m-1)!!(J-m-1)!!}{(J+m)!!(J-m)!!}]^{1/2}|^2 \qquad (C6)$$

is an angular correlation function. In these equations, θ and ψ are the scattering angle of the particle b with respect to the beam axis and the decay angle of the particle c with respect to the direction of k_b, respectively. The m-distribution of the state of B^*, which is expressed by the sub-state population parameters ($p^{Jm}(\theta)$), determines the correlation function. From eq. (C2), $p^{Jm}(\theta)$ is written as:

$$p^{\pi}_{J}(\theta) = N(J,\theta)\sum_{\substack{L_a \\ L_b}} i^{L_a-L_b-J} I^{J}_{L_bL_a} F(L_b,L_a,J,m;\theta), \qquad (C7)$$

where

$$F(L_b,L_a,J,m;\theta) = \sum_{M_a} \langle L_b\ L_a\ m-M_a\ M_a \mid J\ m\rangle Y^{M_a*}_{L_a}(\frac{\pi}{2},-\theta) Y^{m-M_a*}_{L_b}(\frac{\pi}{2},0) \qquad (C8)$$

is a geometric factor and $N(J,\theta)$ is a normalization constant determined by the condition $\sum_{m} |p^{\pi}_{J}(\theta)|^2=1$.

We will see the characteristics of $W(\theta,\psi)$ through $p^{\pi}_{J}(\theta)$ in the heavy-ion transfer reaction where the kinematical matching condition is important. In eq. (C7), the kinematical matching condition can be described in terms of radial integrals $I^{J}_{L_bL_a}$:

(a) $L_b=L_a-J$ terms of $I^{J}_{L_bL_a}$ dominate the other terms.

(b) L_a- distribution of $|I^{J}_{L_bL_a}|$ has a peak centered at the grazing angular momentum ($L_{gr.}$) in the initial channel.

As an extreme case satisfying the conditions (a) and (b), we assume that in the summation of eq. (C7) only the $L_a=L_b+J=L\sim L_{gr.}$ term contributes to the p^{π}_{J}- values. Then, p^{π}_{J} is expressed as:

$$p^{\pi}_{J}(\theta) \propto F(L_b=L-J, L_a=L, J, m;\theta)$$

$$= \frac{(-1)^{L-(J+m)/2}}{4\pi} \left[\frac{(2L-2J+1)!\,(2J+1)!}{(2L)!}\ \frac{(J+m-1)!!\,(J-m-1)!!}{(J+m)!!\,(J-m)!!}\right]^{1/2}$$

$$\times\ G(L,J,m;\theta), \qquad (C9)$$

where

$$G(L,J,m;\theta)$$

$$= \sum_{M} \frac{(L+M-1)!!\,(L-M-1)!!}{(L-J-M+m)!!\,(L-J+M-m)!!\,(J+m-1)!!\,(J-m-1)!!} e^{iM\theta}$$

$$= \frac{L!}{(L-J)!J!} a(L,J,m;\theta)\exp(imb(L,J,m;\theta)). \qquad (C10)$$

Here, we introduce the functions a and b for the absolute magnitude and the phase of G, respectively. By substituting eqs. (C9) and (C10) for eq. (C6), the correlation function is expressed as :

$$W(\theta,\psi) = |w(L,J;\theta,\psi)|^2, \qquad (C11)$$

where

$$w(L,J;\theta,\psi) \propto \sum_{m} \frac{(J+m-1)!!\,(J-m-1)!!}{(J+m)!!\,(J-m)!!}$$

$$\times\ a(L,J,m;\theta)\exp[im(\psi+b(L,J,m;\theta))] \qquad (C12)$$

When $L \gg J \geqq 1$, an analytic approximation is obtained for the functions a and b as follows:

For small θ $(<(J+1)/(L+1))$,

$$a(L,J,m;\theta) \cong 1 - \frac{1}{2} \frac{(L+1)(L-J)(J+m+1)(J-m+1)}{(J+2)(J+1)^2} \theta^2 \qquad (C13)$$

and

$$b(L,J,m;\theta) \cong \frac{L+1}{J+1}\left[1 + \frac{1}{3} \frac{(2L-J+1)(L-J)(J+m+1)(J-m+1)}{(J+3)(J+2)(J+1)^2}\theta^2\right] \theta \ . \qquad (C14)$$

For large θ $(>J/(2L-J))$,

$$a(L,J,m\neq 0;\theta) \cong \left[\frac{J}{(2L-J)\sin\theta}\right]^{(J-|m|+1)/2} , \qquad (C15)$$

$$a(L,J,m=0;\theta) = \frac{(L-J)!\,J!!}{L!}\cdot\frac{P_{L-J/2}^{J/2}(\cos\theta)}{\sin^{J/2}\theta}$$

$$\cong \left[\frac{J}{(2L-J)\sin\theta}\right]^{(J+1)/2}\cos\left[\left(L-\frac{J-1}{2}\right)\theta - \frac{\pi}{4}(J+1)\right] , \qquad (C16)$$

$$|m|b(L,J,m\neq 0;\theta) \cong \left(L-\frac{J-|m|-1}{2}\right)\theta - \frac{\pi}{4}(J-|m|+1) , \qquad (C17)$$

and

$$b(L,J,m=0;\theta) = 0 , \qquad (C18)$$

where P_μ^ν is an associated Legendre function. By substituting eqs. (C13) and (C14) for the expression (C12), $w(L,J;\theta,\psi)$ is approximated for small θ $(<(J+1)/(L+1))$ as follows:

$$w(L,J;\theta,\psi) \propto P_J\left[\cos\left(\psi+\frac{L+1}{J+1}\theta\right)\right]$$

$$- \frac{1}{2}\,\frac{(L+1)(L-J)}{(J+2)(J+1)^2}\,\theta^2\,P_{J+1}'\left[\cos\left(\psi+\frac{L+1}{J+1}\theta\right)\right] , \qquad (C19)$$

where $P_J(x)$ is the Legendre polynomial of order J and $P_{J+1}'(x)$ is the derivative $(d/dx)P_{J+1}(x)$. For large θ $(>J/(2L-J))$, $a(L,J,m=\pm J)$ dominate $a(L,J,m\neq\pm J)$ according to eqs. (C15) and (C16). Then, by taking only $m=\pm J$ terms in eq. (C12), $w(L,J;\theta,\psi)$

is approximated as follows:

$$w(L,J;\theta,\psi) \propto \cos\left[J\left(\psi+\frac{L+\delta}{J+\delta}\theta\right)\right], \qquad (C20)$$

where

$$0 \leqq \delta \sim \frac{J}{2(L-J)}\left(\frac{\pi}{2}-\theta\right) < 1 \ . \qquad (C21)$$

The correlation pattern, $W(\theta,\psi)$ is plotted as a function of ψ for various values of θ. Then the function $W(\theta,\psi)$ changes its shape smoothly from square of Legendre polynomial to square of cosine function as θ is increased, and also changes its phase by the amount of $((L+\Delta)/(J+\Delta))\theta$. Here $\Delta = 1$ for small θ and $\Delta = \delta$ $(0 \leqq \delta < 1)$ for large θ. The change of phase means the shift of the correlation patterns by changing θ. Therefore, the amount of shift of the correlation patterns is expressed as $((L+\Delta)/(J+\Delta))\theta$.

These calculations seem to be too simple. Actually, because the L_a-distribution of $|I^{J}_{L_b=L_a-J,L_a}|$ does not have a sharp peak, several terms contribute to the summation in (C7). But even in such a case, the correlation function $W(\theta,\psi)$ is expressed by eq. (C11) by replacing $w(L,J;\theta,\psi)$ with an average of $w(L,J;\theta,\psi)$ terms over several L-values near $L_{gr.}$. This average is approximated by replacing L with $L_{gr.}$ in (C19) and (C20). In this case, the correlation pattern is proportional to $|w(L_{gr.},J;\theta,\psi)|^2$, and the shift of the pattern is determined by the orbital (grazing) angular momentum in the initial channel ($L_{gr.}$) and the spin of the particle B (J).

REFERENCES

1) T. Tamura, T. Udagawa and M.C. Mermaz, Phys. Rep. 65 (1980) 345

2) G.R. Satchler and W.G. Love, Phys. Rep. 55 (1979) 183

3) R.G. Stokstad, R.M. Wieland, G.R. Satchler, C.B. Fulmer, D.C. Hensley, S. Raman, L.D. Rickertsen, A.H. Snell and P.H. Stelson, Phys. Rev. C20 (1979) 655

4) D.M. Brink, Phys. Rev. Lett. 40 (1972) 37

5) M. Ichimura, E. Takada, T. Yamaya and K. Nagatani, Phys. Lett. 102B (1981) 31

6) R.K. Bhowmik, W.D.M. Rae and B.R. Fulton, Phys. Lett. 136B (1984) 149

7) W.D.M. Rae and R.K. Bhowmik, Nucl. Phys. A420 (1984) 320

8) S.J. Sanders, L.M. Martz and P.D. Parker, Phys. Rev. C20 (1979) 1743

9) M.M. Hindi, J.H. Thomas, D.C. Radford and P.D. Parker, Phys. Lett. 99B (1981) 33

10) A. Cunsolo, A. Foti, G. Immè, G. Pappalardo, G. Raciti and N. Saunier, Phys. Rev. C21 (1980) 2345

11) F. Pougheon, P. Roussel, M. Bernas, F. Diaf, B. Fabbro, F. Naulin, E. Plagnol and G. Rotbard, Nucl. Phys. A325 (1979) 481

12) A.E. Litherland and A.J. Ferguson, Can. J. Phys. 39 (1961) 788

13) P.M. Stwertka, T.M. Cormier, M. Herman, N. Nicolas, A. Szanto de Toledo, M.M. Coimbra and N. Carlin Filho, Phys. Rev. Lett. 49 (1982) 640

14) T. Murakami, E. Ungricht, N. Takahashi, Y.-W. Lui, Y. Mihara,

R.E. Neese, E. Takada, D.M. Tanner, R.E, Tribble and K. Nagatani, Phys. Lett. 120B (1983) 319; T. Murakami, E. Ungricht, N. Takahashi, Y.-W. Lui, Y. Mihara, R.E. Neese, E. Takada, D.M. Tanner, R.E, Tribble and K. Nagatani, Phys. Rev. C29 (1984) 847

15) T. Shimoda, S. Shimoura, T. Fukuda, M. Tanaka, H. Ogata, I. Miura, E. Takada, M.-K. Tanaka, K. Takimoto and K. Katori, J. Phys. G9 (1983) L199

16) W.D. Rae, R.G. Stokstad, B.G. Harvey, A. Dacal, R. Legrain, J. Mahoney, M.J. Murphy and T.J.M. Symons, Phys. Rev. Lett. 45 (1980) 884

17) H. Homeyer, M. Bürgel, M. Clover, Ch. Egelhaaf, H. Fuchs, A. Gamp, D. Kovar and W. Rauch, Phys. Rev. C26 (1982) 1335

18) W.D. Rae, A.J. Cole, A. Dacal, R. Legrain, B.G. Harvey, J. Mahoney, M.J. Murphy, R.G. Stokstad and I. Tserruya, Phys. Lett. 105B (1981) 417

19) A.N. Bice, A.C. Shotter and Joseph Cerny, Nucl. Phys. A390 (1982) 161

20) R. Ost, S. Kox, A.J. Cole, N. Longequeue, J.J. Lucas, J. Menet and J.B. Viano, Nucl. Phys. A361 (1981) 453

21) G.C. Phillips, Rev. Mod. Phys. 37 (1965) 409

22) S. Kubono, K. Morita, M.H. Tanaka, M. Sugitani, H. Utsunomiya, H. Yonehara, M.-K. Tanaka, S. Shimoura, E. Takada, M. Fukada and K. Takimoto, Phys. Lett. 127B (1983) 19

23) I. Katayama and H. Ogata, Nucl. Instr. Meth. 174 (1980) 295

24) G.G. Ohlsen, Nucl. Instr. Meth. 37 (1965) 240

25) J.S. Blair and L. Wilets, Phys. Rev. 121 (1961) 1493

26) S.J. Willett, S.K. Korotky, R.L. Phillips, D.A. Bromley, K.A. Erb, Phys. Rev. C28 (1983) 1986

27) M. Igarashi, Finite-range DWBA code TWOFNR, 1977; private communication

28) G.R. Satchler, C.B. Fulmer, R.L. Auble, J.B. Ball, F.E. Bertrand, K.A. Erb, E.E. Gross and D.C. Hensley, Phys. Lett. 128B (1983) 147

29) J.C. Peng, J.V. Maher, W. Oelert, D.A. Sink, C.M. Cheng and H.S. Song, Nucl. Phys. A264 (1976) 312

30) C. Olmer, M. Mermaz, M. Buenerd, C.K. Gelbke, D.H. Hendrie, J. Mahoney, D.K. Scott, M.H. Macfarlane and S.C. Pieper, Phys. Rev. C18 (1978) 205

31) C.B. Fulmer, R.M. Wieland, D.C. Hensley, S. Raman, G.R. Satchler, A.H. Snell, P.H. Stelson and R.G. Stokstad, Phys. Rev. C20 (1979) 670

32) R.H. Dalitz, Ann. Rev. Nucl. Sci. 13 (1963) 339

33) G.R. Satchler, Nucl. Phys. 55 (1964) 1

Table 1. Optical-model parameters used in the DWBA analysis.

Channel	V (MeV)	r_V (fm)	a_V (fm)	W (MeV)	r_W (fm)	a_W (fm)	r_C (fm)
$^{12}C + {}^{12}C$	200	0.783	0.760	142.3 75.0[a]	0.783	0.760	1.2
$^{8}Be + {}^{16}O$	184.8	0.670	0.921	31.0	1.023	0.939	1.2

(a) Used in the analysis of the inelastic scattering to achieve better agreement with data (see text).

Table 2. Integrated cross sections in various channels (mb).

Incident energy (MeV)		88.3[a]	93.8[b]	108.6[a]	138.5[a]
elastic			37.5[c]		
inelastic	(2^+)		45.5[c]		
	(2^+,2^+)		14.0[c]		
	(3^-)	12.4		6.7	8.6
	(4^+)	3.1		3.1	4.6
n-transfer			2.02[d]		
p-transfer			2.01[d]		
(pn)-transfer			3.49[d]		
α-transfer	(4^+)	0.75		0.10	
	(5^-)	1.5		0.39	
	(6^+)	3.6		1.2	0.29
	(7^-)	2.7		1.8	0.76

(a) Present work. The range of integration is 0° – 60°. (b) Ref. 31. The range of integration is 10° – 65°. (c) These cross sections should be divided by two for comparison with the other ones, because both the scattered particles and the recoil nucleus are included[31]. (d) The summation over the states of the residual nuclei is given[31].

Figure captions

Fig. 1. Schematic drawing of the experimental arrangement showing the relative position of the target, Faraday-cup (FC), and detectors. Thickness of each Si-SSD and solid angle of each detector are indicated.

Fig. 2. Flow charts of the data reduction procedure. Solid lines denote the main flow for the final data, while dashed lines denote the flow for the pre-analysis to determine gates and other parameters.

Fig. 3. Typical particle-identification spectra of (a) α_1-detector and (b) HI-detector at 140 MeV.

Fig. 4. Typical TAC spectra for coincidence of (a) α_1-HI and (b) α_0-HI detectors at 140 MeV.

Fig. 5. A typical three-body Q-value spectrum for the incident energy of 90 MeV. Arrows indicate the final channels $^{12}C_{g.s.}+\alpha+^{8}Be_{g.s.}$ (Q_{ggg}), $^{12}C_{g.s.}+\alpha+^{8}Be(2^+)$, and $^{12}C(2^+)+\alpha+^{8}Be_{g.s.}$.

Fig. 6. Typical relative-energy spectra at 110 MeV for (a) ^{12}C-α ($^{16}O^*$) and (b) α-^{8}Be ($^{12}C^*$) pairs. Spins and parities for states of the peaks are indicated.

Fig. 7. Scatter plots of the $^{12}C+^{12}C \rightarrow ^{12}C_{g.s.}+\alpha+^{8}Be_{g.s.}$ reaction at (a) 90 MeV and (b) 110 MeV.

Fig. 8. The velocity diagram in the total center-of-mass system and the definition of the angles for the sequential process of $i+(j+k)^* \rightarrow i+j+k$ $((i,j,k)=(1,2,3),(2,3,1),(3,1,2))$.

Fig. 9. Double-differential cross sections $d^2\sigma/d\Omega_{3\text{-}12}d\Omega_{1\text{-}2}$ of the

$^{12}C+^{12}C \rightarrow ^{16}O^{*}+^{8}Be \rightarrow ^{12}C_{g.s.}+\alpha+^{8}Be_{g.s.}$ reaction for the states of the $^{16}O^{*}$-nuclei (a) 7^{-}, (b) 6^{+}, (c) 5^{-}, and (d) 4^{+} at the incident energy of 90 MeV as a function of $\theta_{1\text{-}2}$ (horizontal axis) and $\theta^{c.m.}(^{16}O^{*}) = \theta_{3\text{-}12} - 180^{\circ}$ (indicated in the middle column). Solid lines show the results of the DWBA calculation.

Fig. 10. Same as fig. 9 for the incident energy of 110 MeV.

Fig. 11. Same as fig. 9 for the incident energy of 140 MeV (5^{-}- and 4^{+}-states are not included).

Fig. 12. The position of the maxima (dots) and minima (crosses) of the correlation patterns for the α-transfer to the $^{16}O^{*}(6^{+})$- state at 90 MeV. Dashed lines represent the shift of the maxima predicted by the plane-wave Born approximation (PWBA). Solid lines with a gradient $-7/23$ ($\sim -(J+1)/(L_{gr.}+1)$ see text) show the prediction of DWBA.

Fig. 13. Double-differential cross sections $d^{2}\sigma/d\Omega_{1\text{-}23}d\Omega_{2\text{-}3}$ of the $^{12}C+^{12}C \rightarrow ^{12}C+^{12}C^{*} \rightarrow ^{12}C_{g.s.}+\alpha+^{8}Be_{g.s.}$ reaction for the states of the $^{12}C^{*}$-nuclei (a) 4^{+} and (b) 3^{-} at the incident energy of 90 MeV as a function of $\theta_{2\text{-}3}$ (horizontal axis) and $\theta^{c.m.}(^{12}C) = \theta_{1\text{-}23}$ (indicated in the middle column). Solid lines show the results of the DWBA calculation with a weak imaginary potential (see text).

Fig. 14. Same as fig. 13 for the incident energy of 110 MeV.

Fig. 15. Same as fig. 14 for the incident energy of 140 MeV. Dashed lines show the results of the DWBA calculation with the potential reproducing the elastic scattering data.

Fig. 16. (a) Radial integrals $|I^{J}_{L_b L_a}|$ as a function of L_a and L_b and (b) sub-state populations $|p^{J}_{M}|$ as a function of $\theta^{c.m.}$. These quantities were calculated by the DWBA for the $^{12}C+^{12}C \rightarrow ^{16}O^{*}(6^{+})+^{8}Be$ reaction at 90 MeV. For the calculation of $|p^{J}_{M}|$, the quantization axis is taken to be perpendicular to the reaction plane.

Fig. 17. Same as fig. 16 for the $^{12}C+^{12}C \rightarrow ^{12}C+^{12}C^{*}(4^{+})$ reaction at 140 MeV.

Fig. 18. Integrated cross sections of the experiment (dots with dashed line) and of the DWBA calculation for α-transfer (a) and inelastic scattering (b) processes. In the integration of the experiment, the azimuthal angular distributions of the correlation patterns were assumed to be those obtained by the DWBA calculation. The experimental values are identical to those in table 1.

Fig. 19. (a) The k-values, ratio of the observed cross sections to the simple sum of the α-transfer and the inelastic scattering processes calculated by the DWBA, are plotted as a function of $\theta^{c.m.}(^{16}O^{*})$ (or $\theta^{c.m.}(^{12}C)$) for the crossing point of $^{16}O^{*}(7^{-})-^{12}C^{*}(4^{+})$ at 90 MeV. Solid line is drawn to guide the eye. (b) Phase differences between the T-matrices of these two processes calculated by the DWBA are shown for comparison.

Fig. 20. Same as fig. 19(a) for the crossing points of (a) $^{16}O^{*}(6^{+})-^{12}C^{*}(4^{+})$ at 90 MeV, (b) $^{16}O^{*}(7^{-})-^{12}C^{*}(3^{-})$ at 90 MeV, (c) $^{16}O^{*}(7^{-})-^{12}C^{*}(4^{+})$ at 110 MeV and (d) $^{16}O^{*}(7^{-})-^{12}C^{*}(4^{+})$ at 140 MeV.

Fig. 21. An illustration of a modified Dalitz-plot. An event with relative energies $E_{2\text{-}3}$, $E_{1\text{-}2}$ and $E_{3\text{-}1}$ is represented by the point X. The ratio of the sides of the triangle is $(m_2+m_3):(m_3+m_1):(m_1+m_2)$. The inscribed circle with the radius of $E^{f}_{c.m.}/2$ shows the boundary of the data.

Fig. 22. Two-dimensional plots of efficiency ε for (a) $^{16}O^{*}(7^{-})+^{8}Be$ and $^{12}C(4^{+})+^{12}C^{*}$ (b) at 90 MeV. Horizontal and vertical axes denote decay angles ($\theta_{j\text{-}k}$) and primary angles ($\theta^{c.m.}$), respectively.

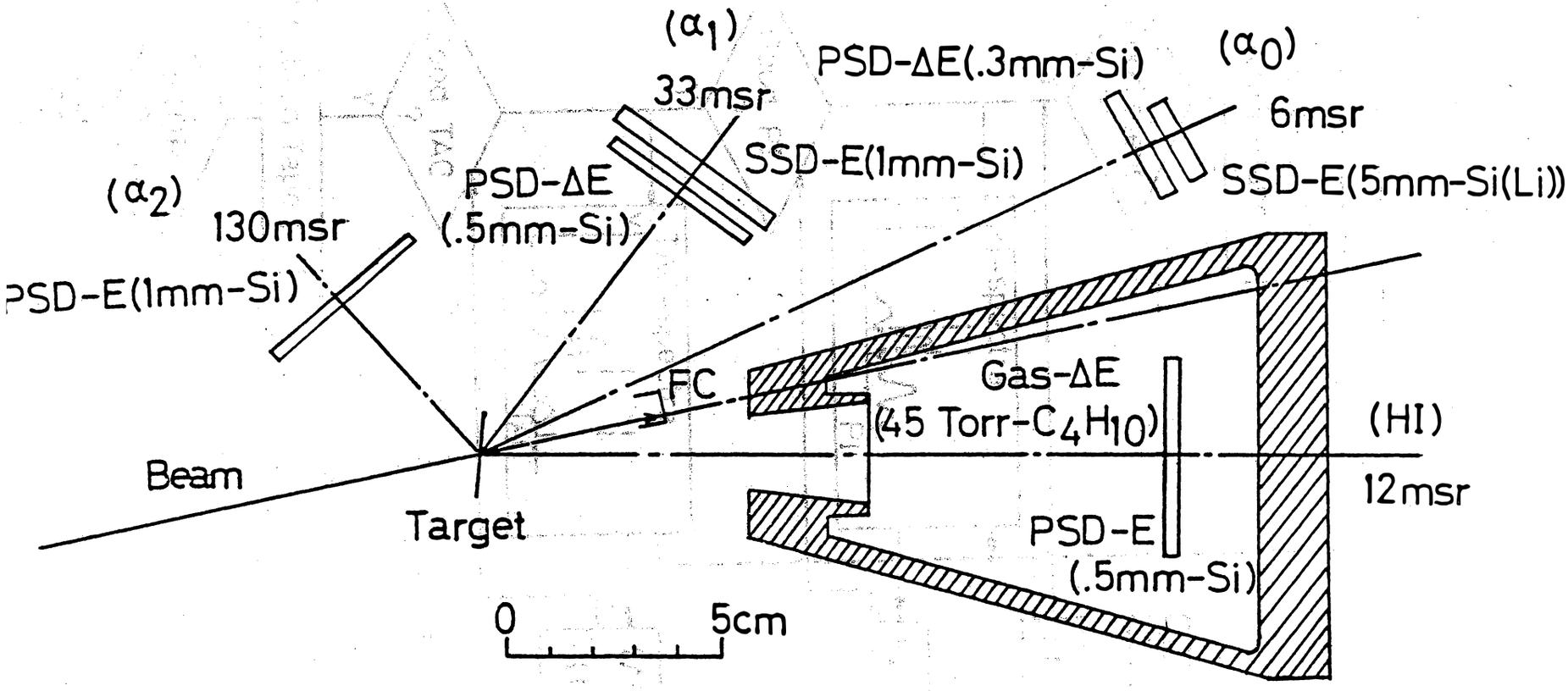
(α1)
33msr
PSD-ΔE(.3mm-Si)
(α0)
6msr
SSD-E(1mm-Si)
SSD-E(5mm-Si(Li))
(α2)
130msr
PSD-ΔE
(.5mm-Si)
PSD-E(1mm-Si)
FC
Gas-ΔE
(45 Torr-C4H10)
(HI)
12msr
Beam
Target
PSD-E
(.5mm-Si)
0
5cm

Fig. 1.

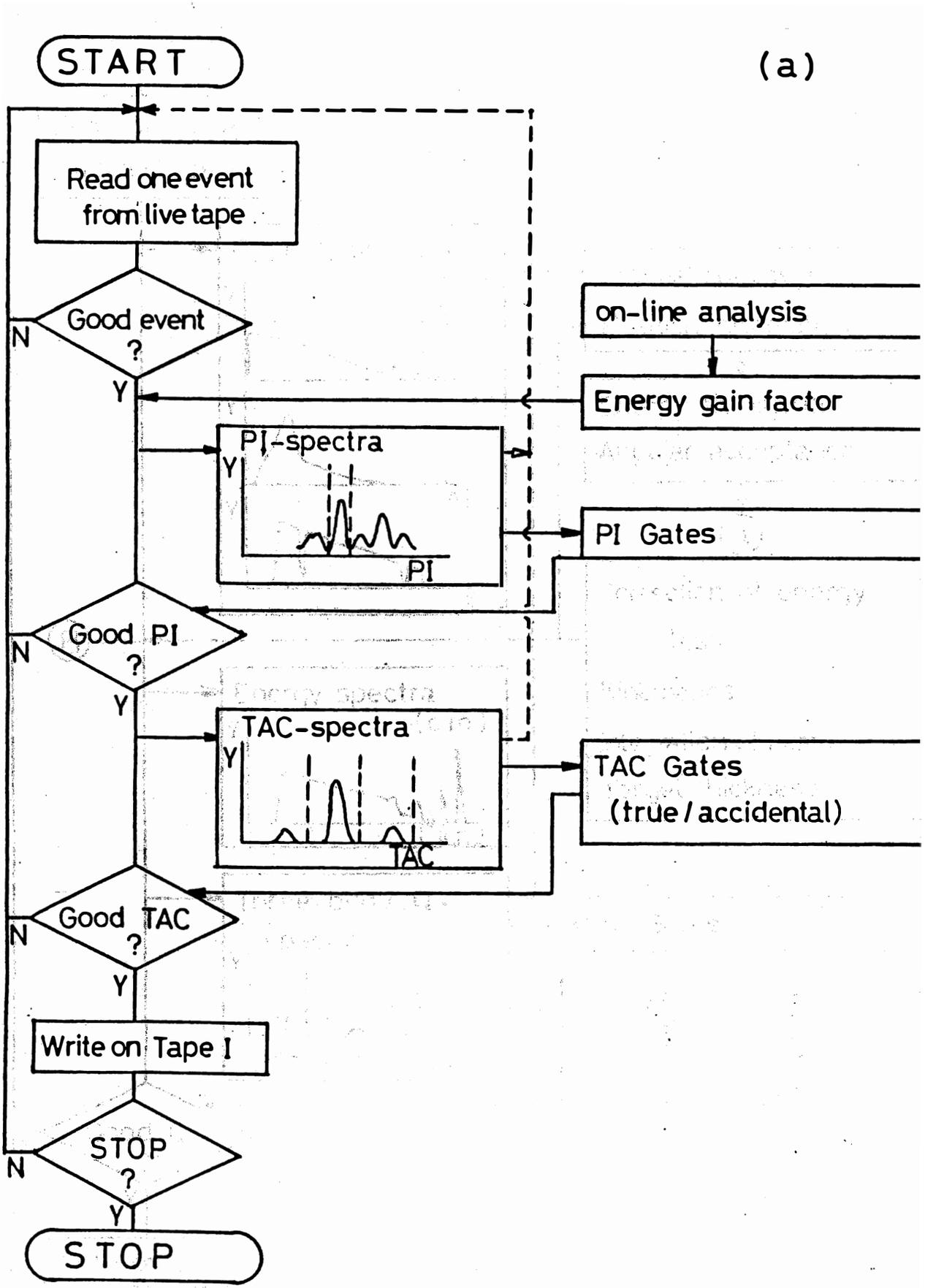
START
(a)
Read one event from live tape
Good event ?
N
Y
on-line analysis
Energy gain factor
PI-spectra
Y
PI
PI Gates
Good PI ?
N
Y
TAC-spectra
Y
TAC
TAC Gates (true / accidental)
Good TAC ?
N
Y
Write on Tape I
STOP ?
N
Y
STOP

Fig. 2.

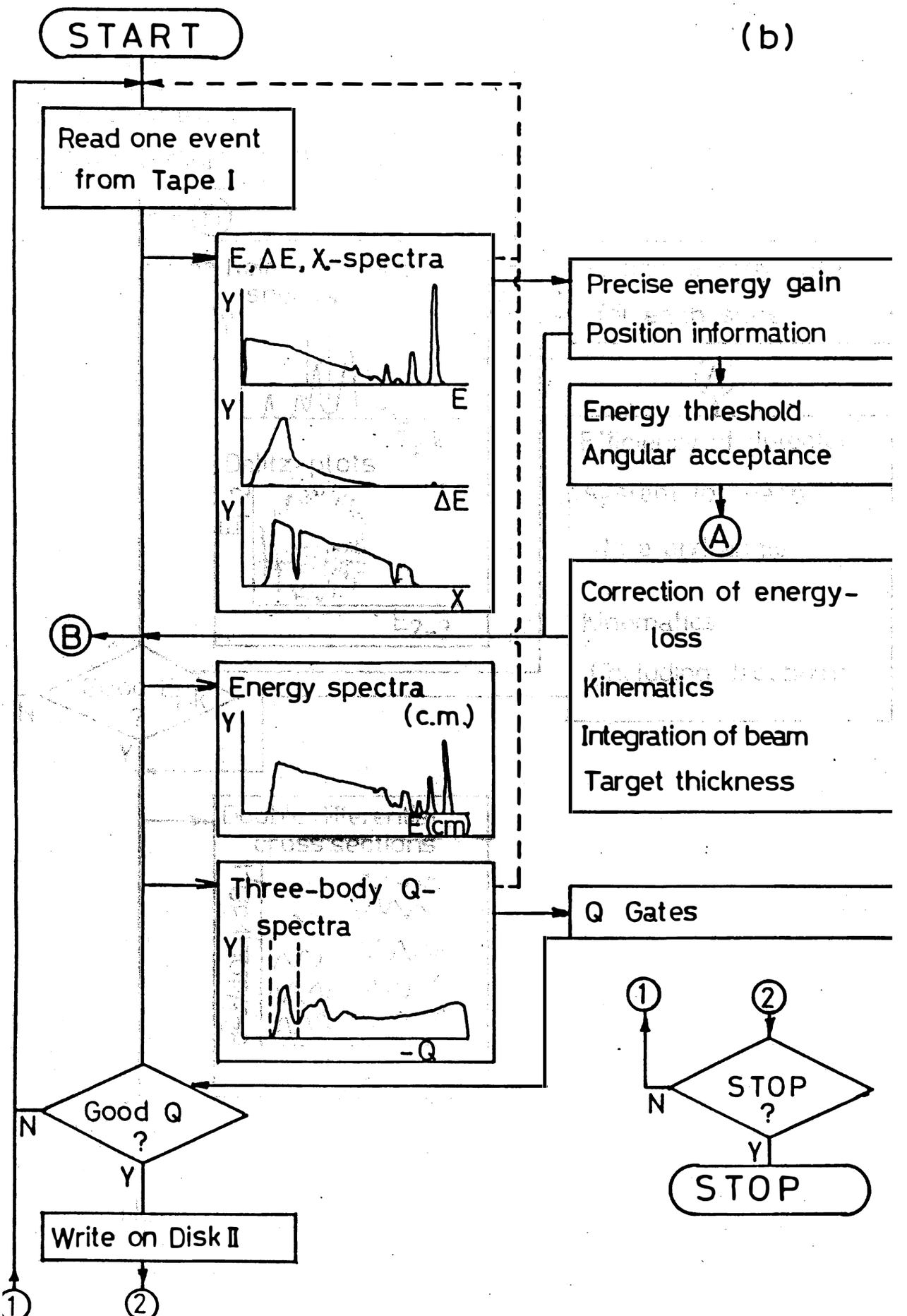
START
(b)
Read one event from Tape I
E, ΔE, X-spectra
Y
E
Y
ΔE
Y
X
Precise energy gain
Position information
Energy threshold
Angular acceptance
A
Correction of energy-loss
Kinematics
Integration of beam
Target thickness
B
Energy spectra (c.m.)
Y
E(cm)
Three-body Q-spectra
Y
-Q
Q Gates
Good Q ?
N
Y
Write on Disk II
1
2
1
2
STOP ?
N
Y
STOP

Fig. 2.

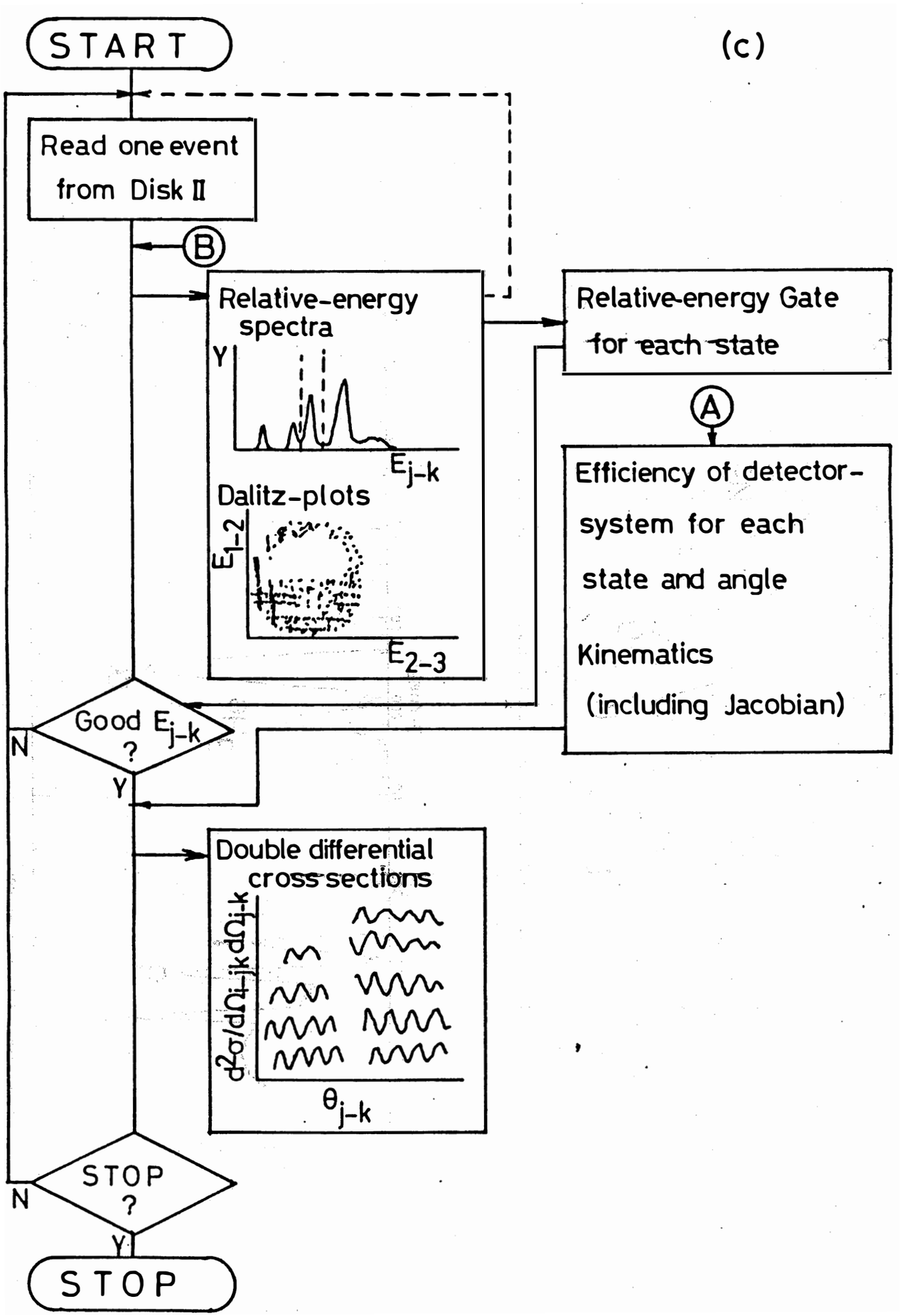
START
(c)
Read one event from Disk II
B
Relative-energy spectra
Y
E_{j-k}
Dalitz-plots
E_{1-2}
E_{2-3}
Relative-energy Gate for each state
A
Efficiency of detector-system for each state and angle
Kinematics (including Jacobian)
Good E_{j-k} ?
N
Y
Double differential cross sections
$d^2\sigma/d\Omega_{i-jk}d\Omega_{j-k}$
θ_{j-k}
STOP ?
N
Y
STOP

Fig. 2.

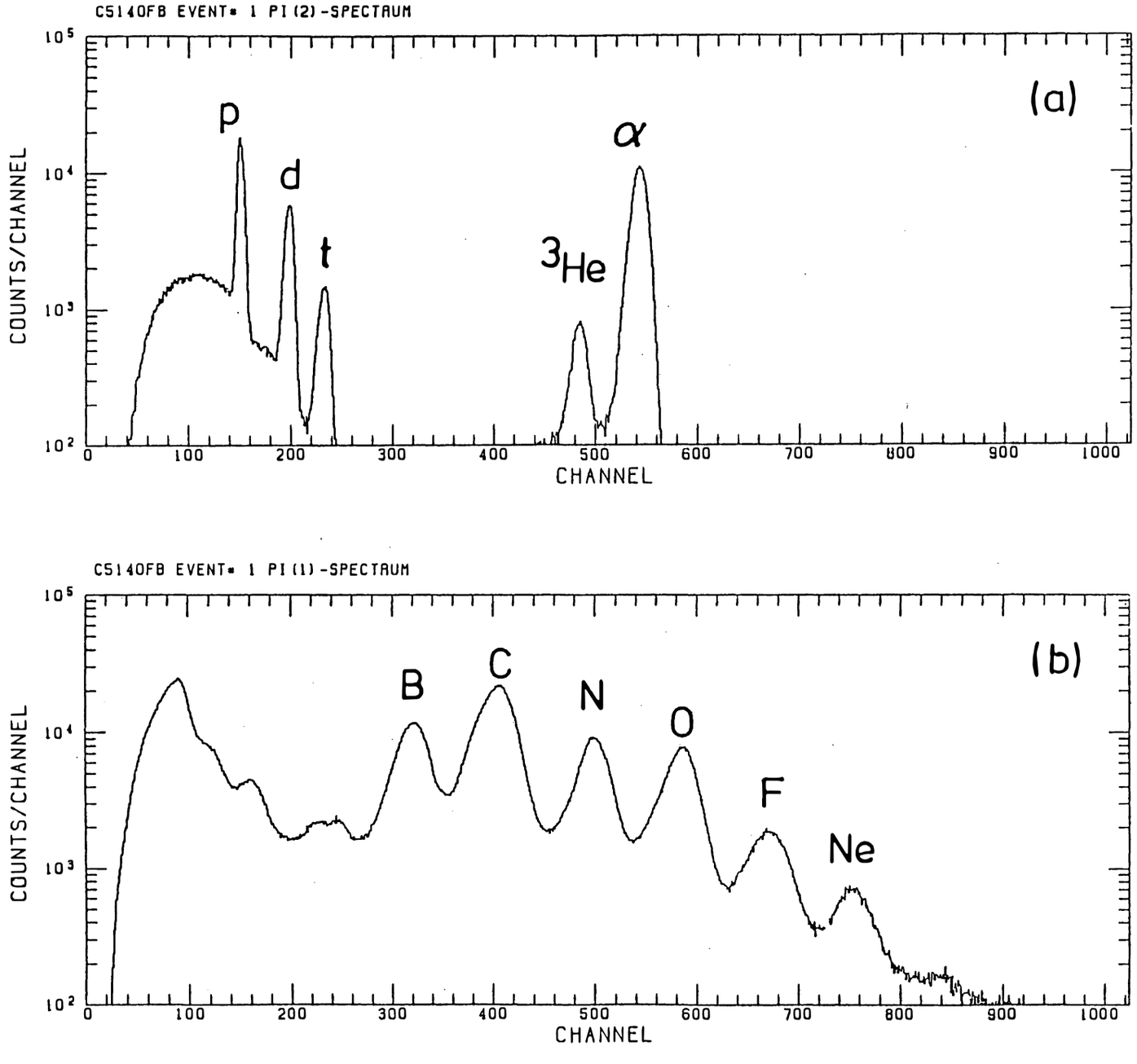
C5140FB EVENT= 1 PI(2)-SPECTRUM
COUNTS/CHANNEL
CHANNEL
p
d
t
3He
α
(a)
C5140FB EVENT= 1 PI(1)-SPECTRUM
COUNTS/CHANNEL
CHANNEL
B
C
N
O
F
Ne
(b)

Fig. 3.

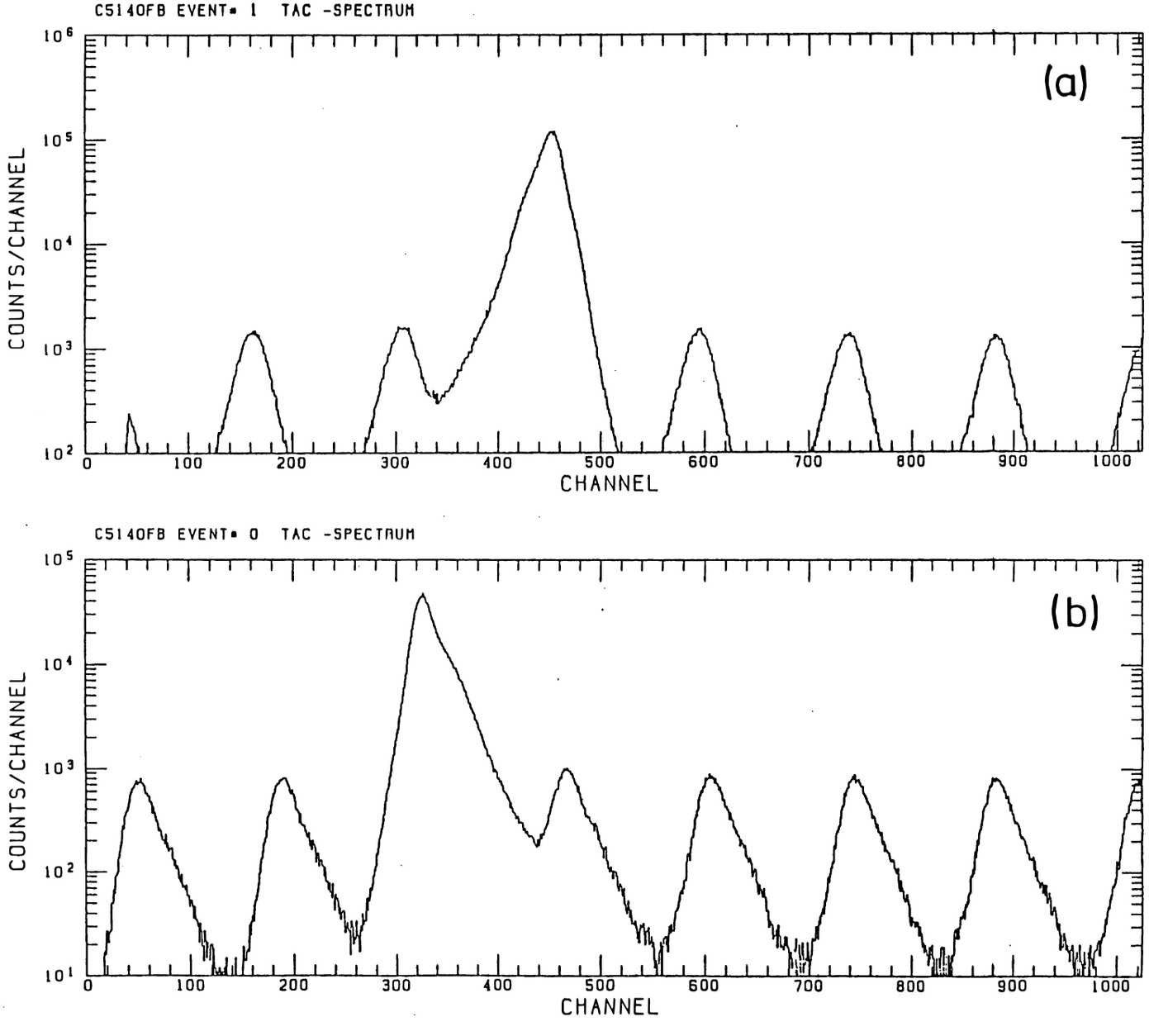
C5140FB EVENT# 1 TAC -SPECTRUM
(a)
COUNTS/CHANNEL
CHANNEL
C5140FB EVENT# 0 TAC -SPECTRUM
(b)
COUNTS/CHANNEL
CHANNEL

Fig. 4.

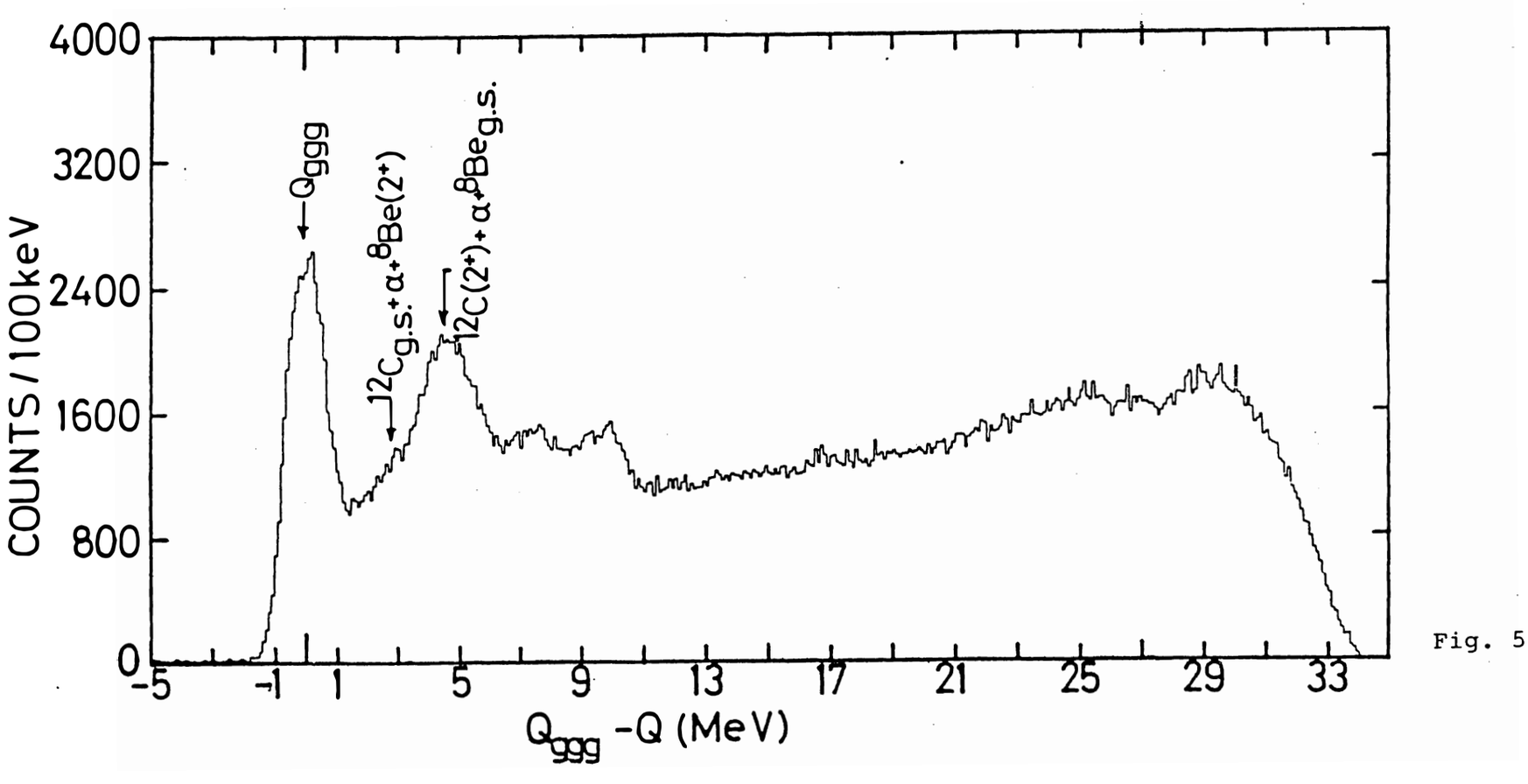
4000
3200
2400
1600
800
0
COUNTS/100keV
Q_{ggg}
$^{12}C_{g.s.}+\alpha+^{8}Be(2^+)$
$^{12}C(2^+)+\alpha+^{8}Be_{g.s.}$
-5
-1
1
5
9
13
17
21
25
29
33
Q_{ggg} -Q (MeV)

Fig. 5.

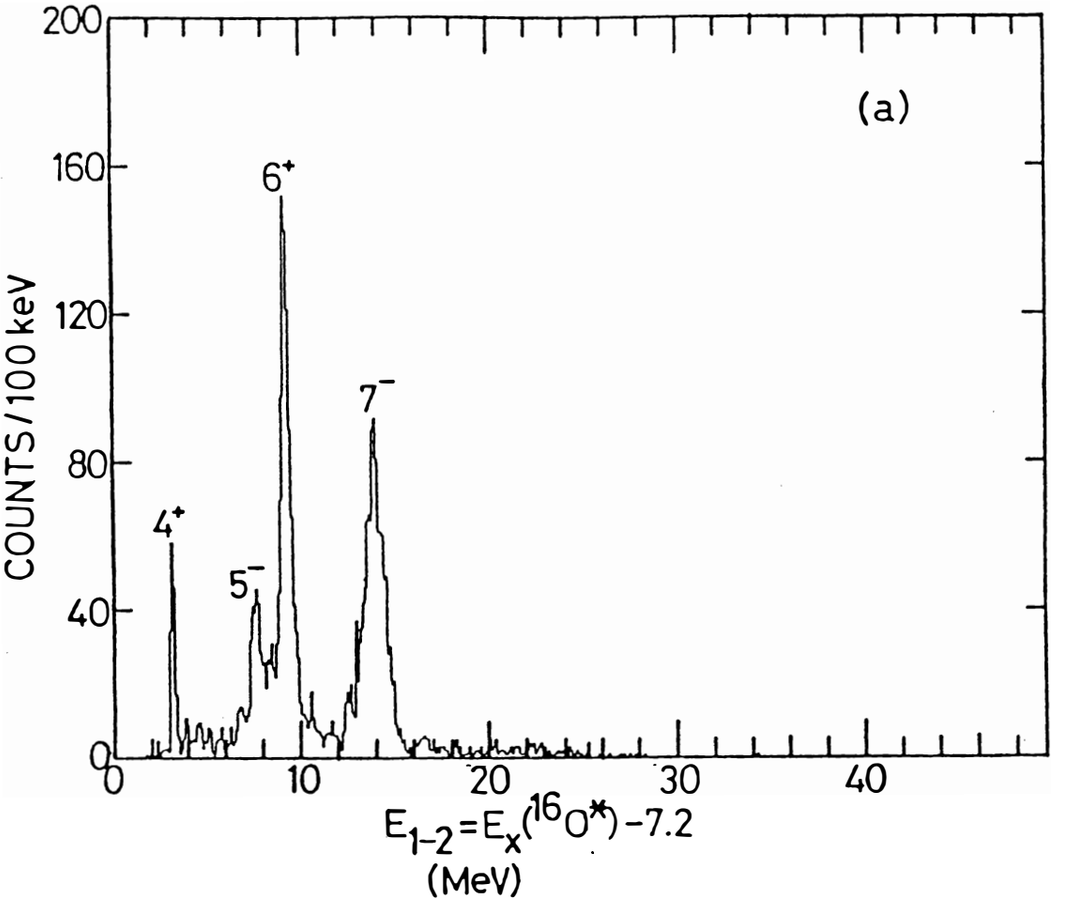
(a)
6+
7−
4+
5−
COUNTS/100 keV
200
160
120
80
40
0
0
10
20
30
40
E1-2=Ex(16O*)-7.2
(MeV)

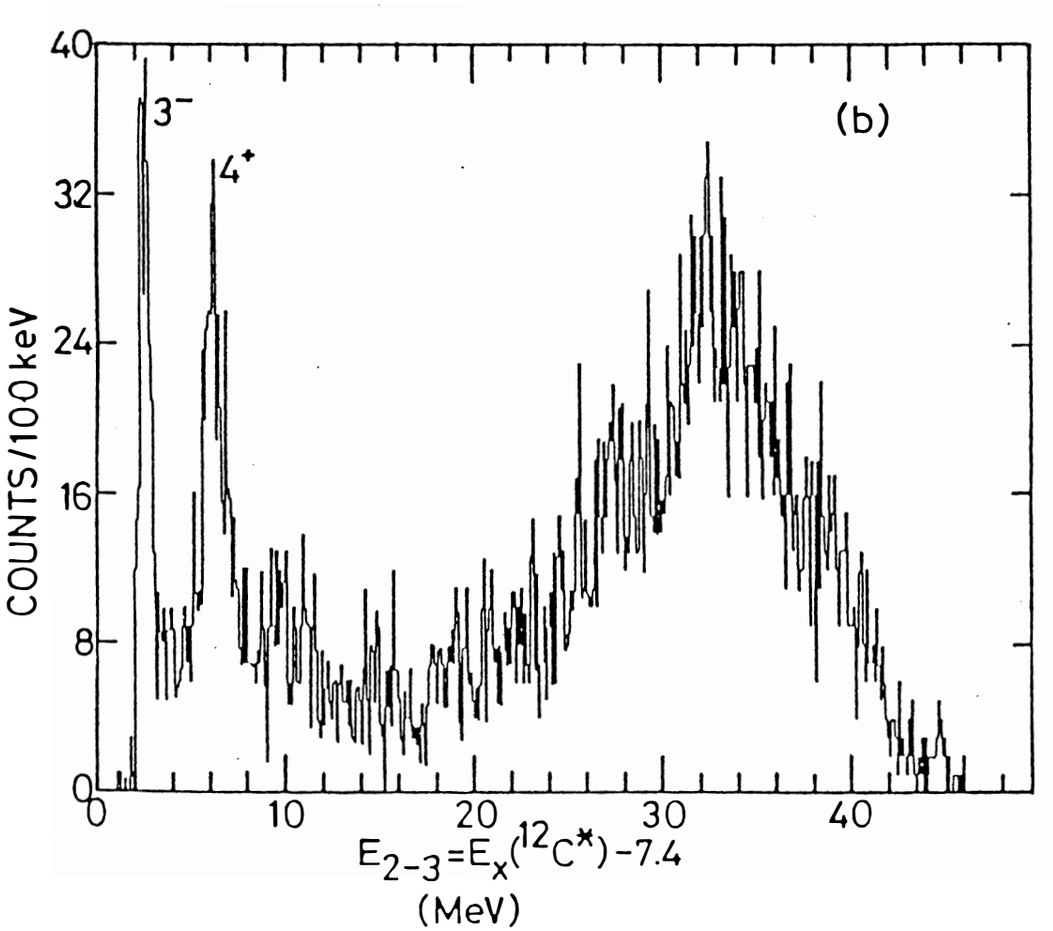
(b)
3−
4+
COUNTS/100 keV
40
32
24
16
8
0
0
10
20
30
40
E2-3=Ex(12C*)-7.4
(MeV)

Fig. 6.

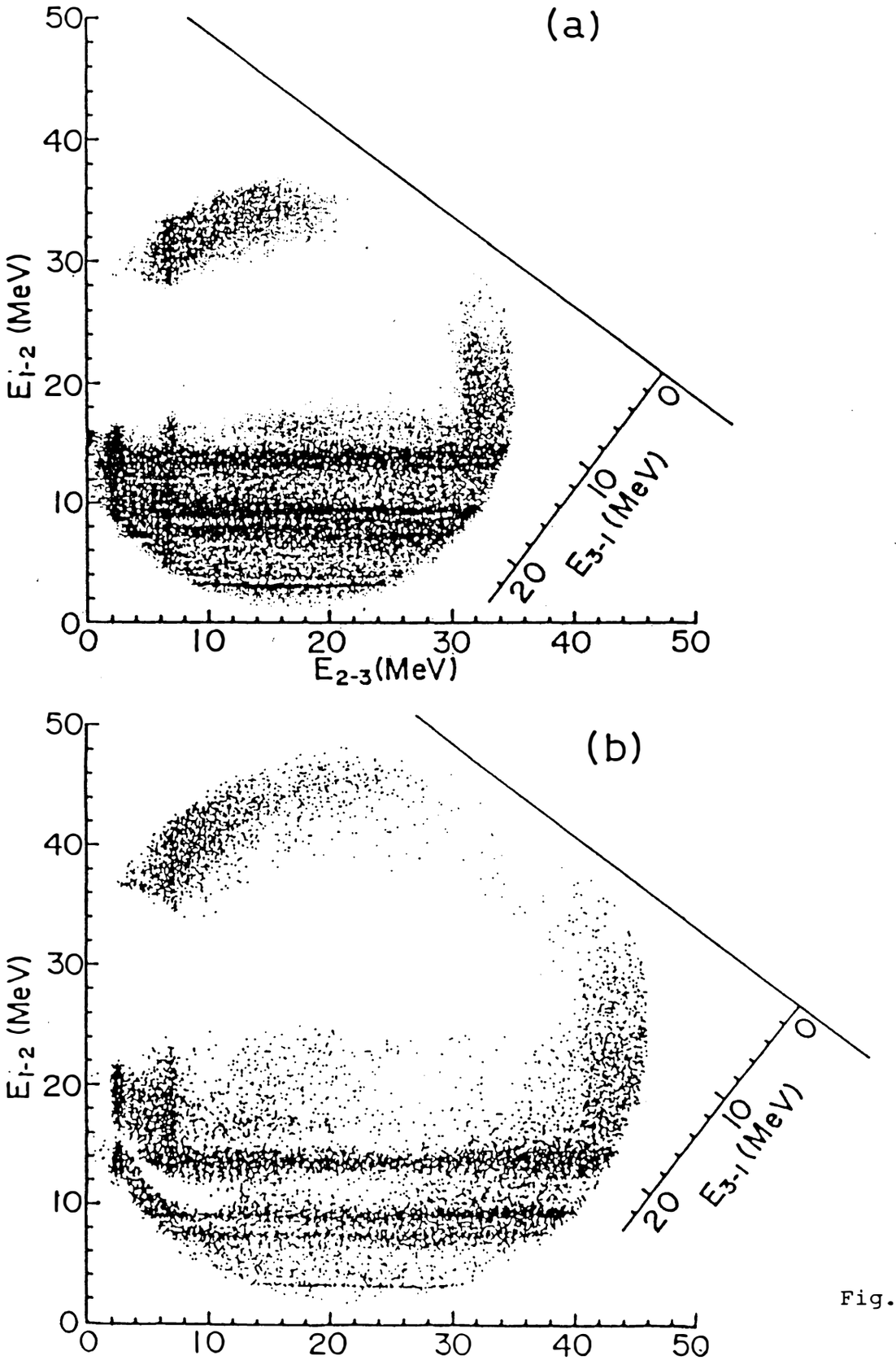

Fig. 7.

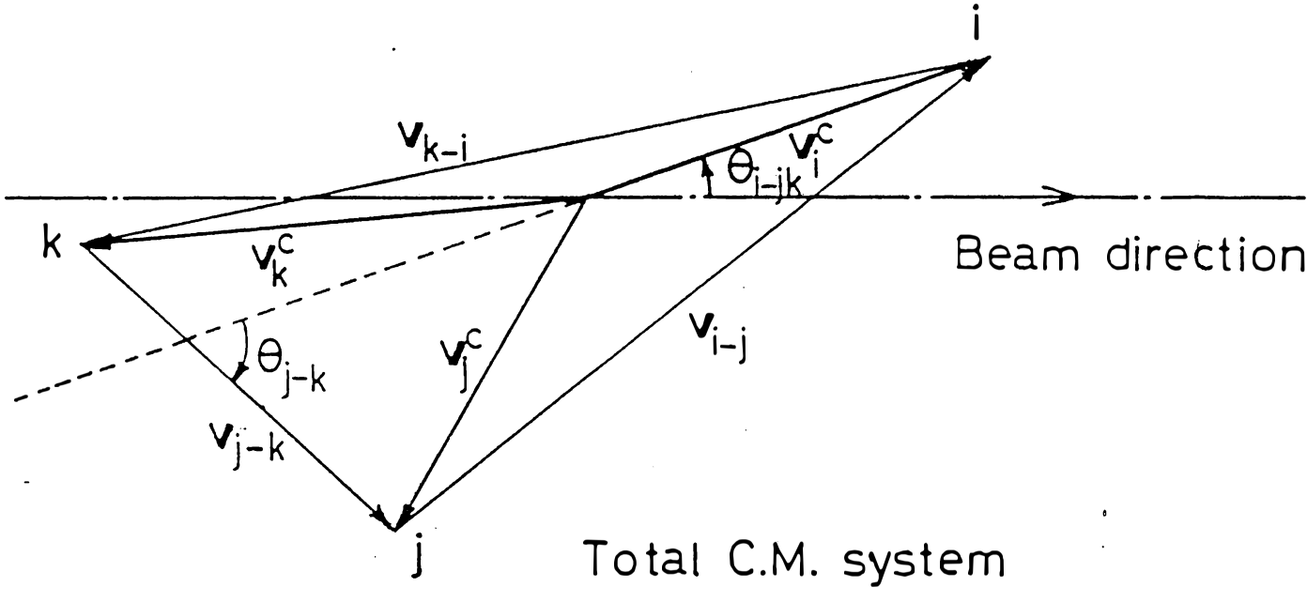
i
v_{k-i}
v_i^c
θ_{i-jk}
k
v_k^c
Beam direction
θ_{j-k}
v_j^c
v_{i-j}
v_{j-k}
j
Total C.M. system

Fig. 8.

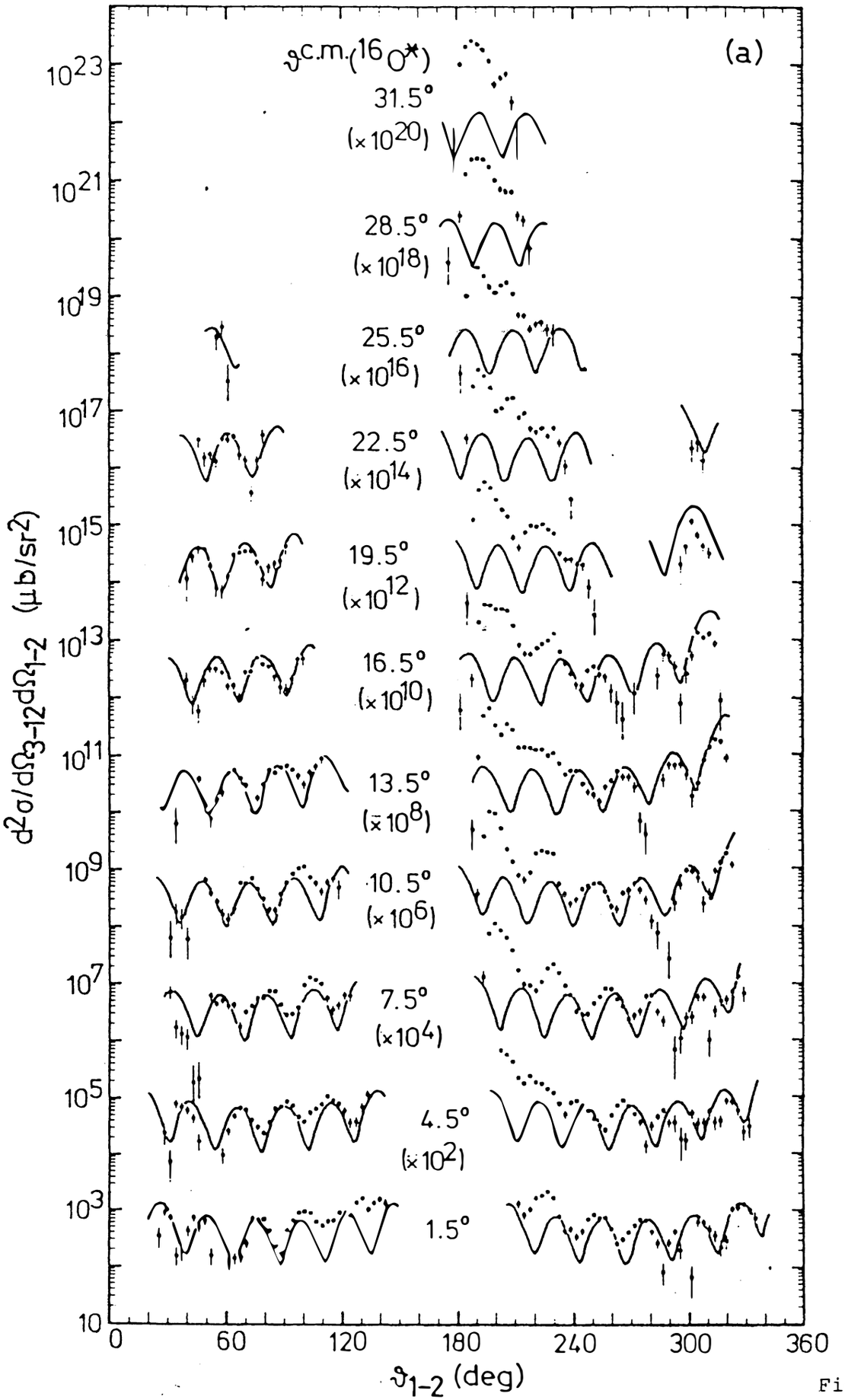
(a)
$\vartheta^{c.m.}(^{16}O^*)$
31.5°
(×10^20)
28.5°
(×10^18)
25.5°
(×10^16)
22.5°
(×10^14)
19.5°
(×10^12)
16.5°
(×10^10)
13.5°
(×10^8)
10.5°
(×10^6)
7.5°
(×10^4)
4.5°
(×10^2)
1.5°
$d^2\sigma/d\Omega_{3-12}d\Omega_{1-2}$ (μb/sr²)
ϑ_{1-2} (deg)
10^23
10^21
10^19
10^17
10^15
10^13
10^11
10^9
10^7
10^5
10^3
10
0
60
120
180
240
300
360

Fig. 9.

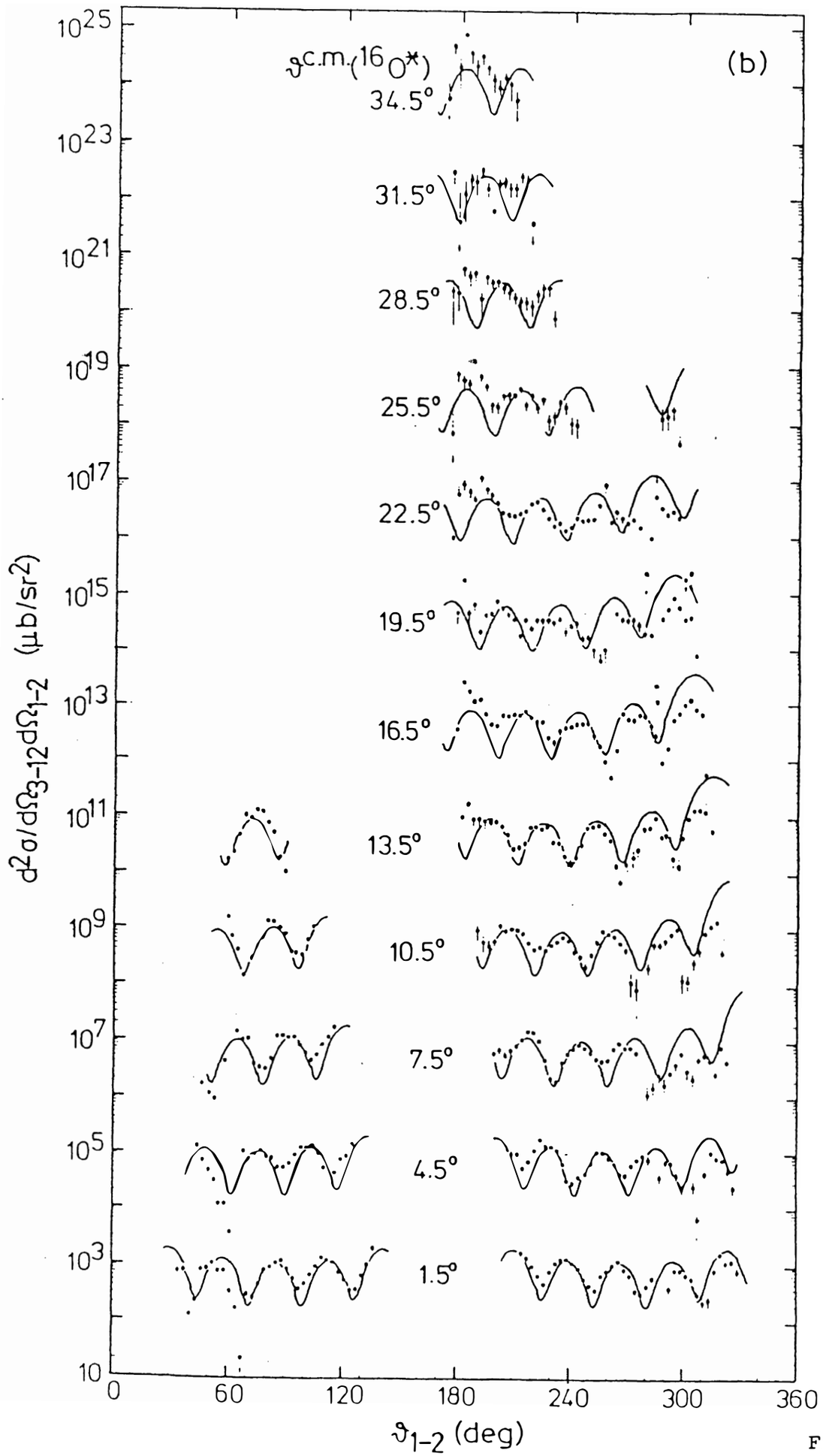
(b)
$\vartheta^{c.m.}(^{16}O^*)$
34.5°
31.5°
28.5°
25.5°
22.5°
19.5°
16.5°
13.5°
10.5°
7.5°
4.5°
1.5°
$d^2\sigma/d\Omega_{3-12}d\Omega_{1-2}$ (μb/sr²)
ϑ_{1-2} (deg)
10^{25}
10^{23}
10^{21}
10^{19}
10^{17}
10^{15}
10^{13}
10^{11}
10^{9}
10^{7}
10^{5}
10^{3}
10
0
60
120
180
240
300
360

Fig. 9.

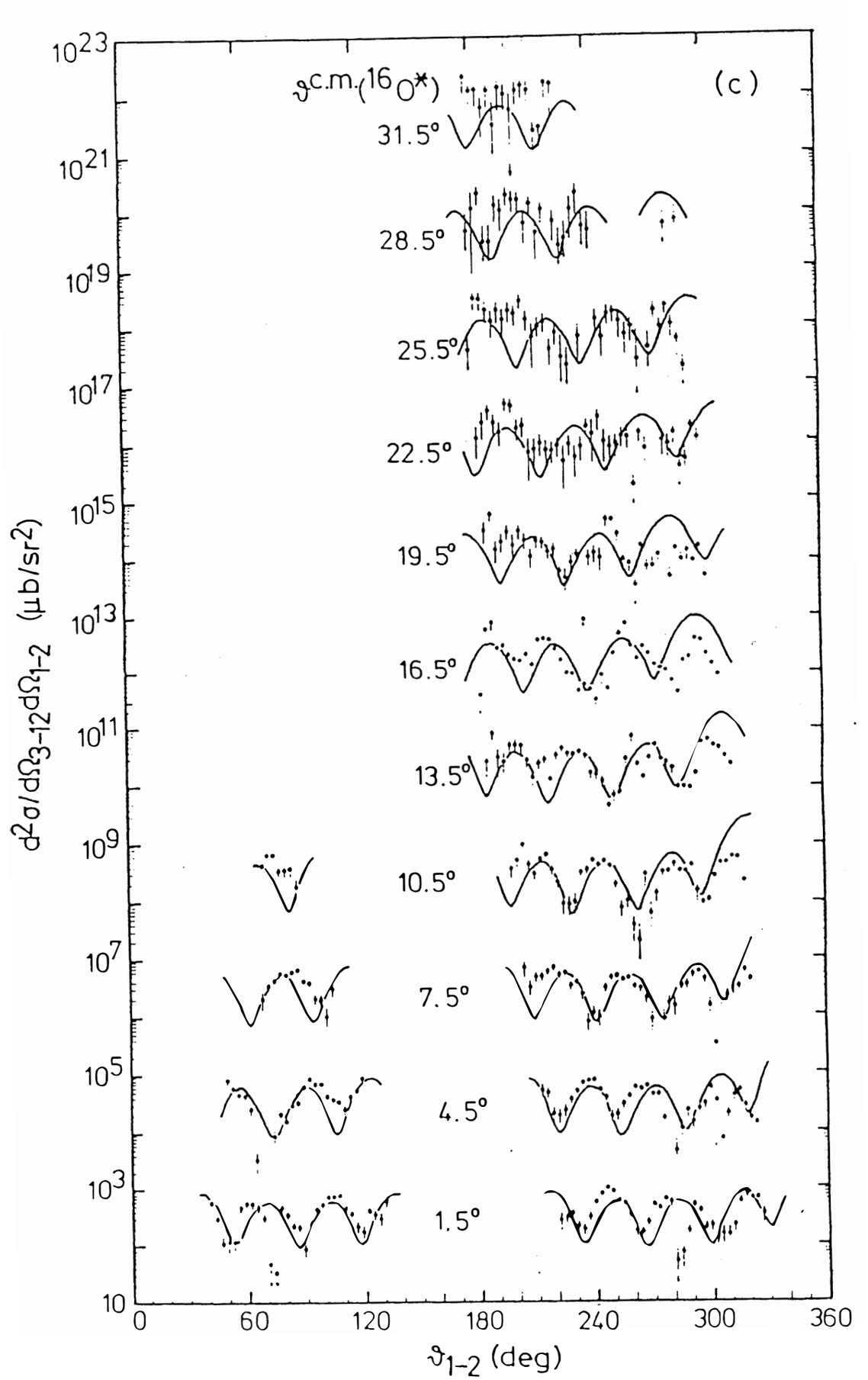
$\vartheta_{c.m.}(^{16}O^*)$
(c)
31.5°
28.5°
25.5°
22.5°
19.5°
16.5°
13.5°
10.5°
7.5°
4.5°
1.5°
$d^2\sigma/d\Omega_{3-12}d\Omega_{1-2}$ (μb/sr²)
ϑ_{1-2} (deg)
10^{23}
10^{21}
10^{19}
10^{17}
10^{15}
10^{13}
10^{11}
10^{9}
10^{7}
10^{5}
10^{3}
10
0
60
120
180
240
300
360

Fig. 9.

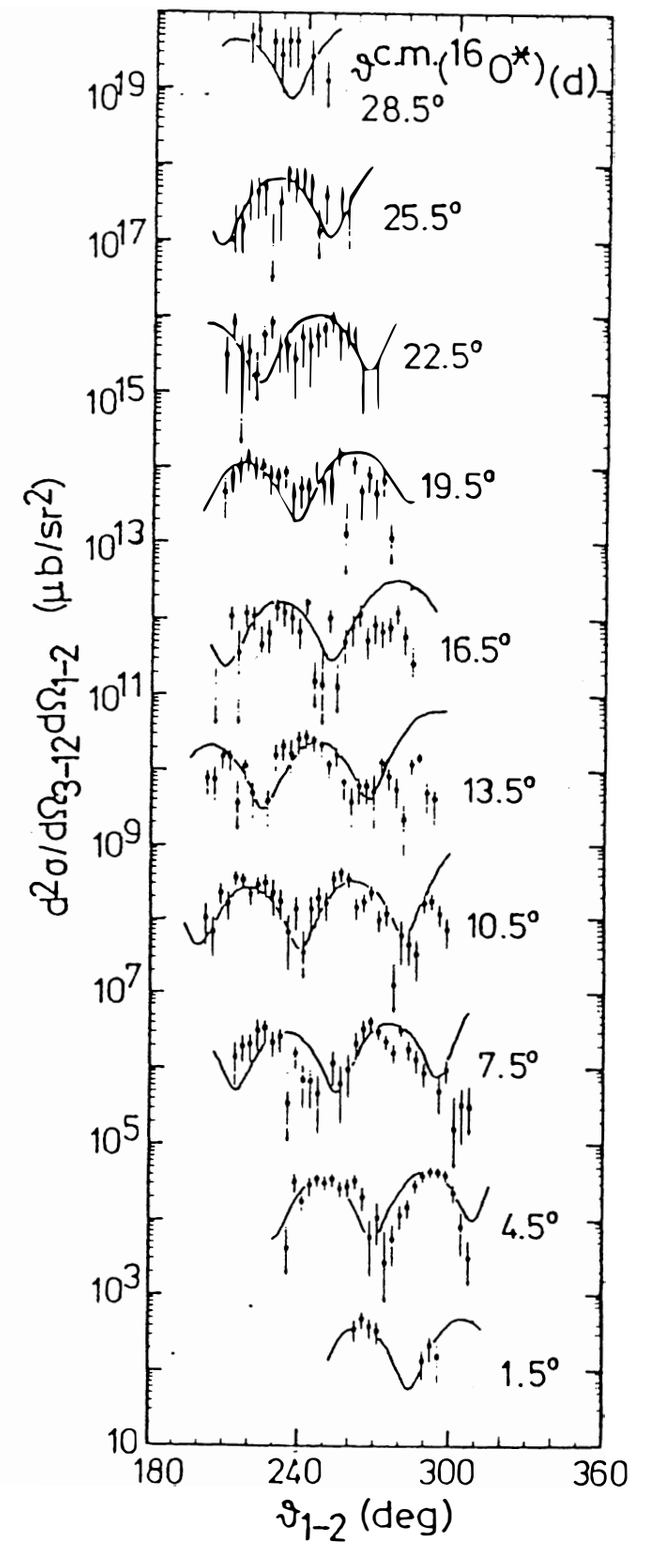
$\vartheta_{c.m.}(^{16}O^*)$ (d)
28.5°
25.5°
22.5°
19.5°
16.5°
13.5°
10.5°
7.5°
4.5°
1.5°
10^{19}
10^{17}
10^{15}
10^{13}
10^{11}
10^{9}
10^{7}
10^{5}
10^{3}
10
$d^2\sigma/d\Omega_{3-12}d\Omega_{1-2}$ (μb/sr^2)
180
240
300
360
ϑ_{1-2} (deg)

Fig. 9.

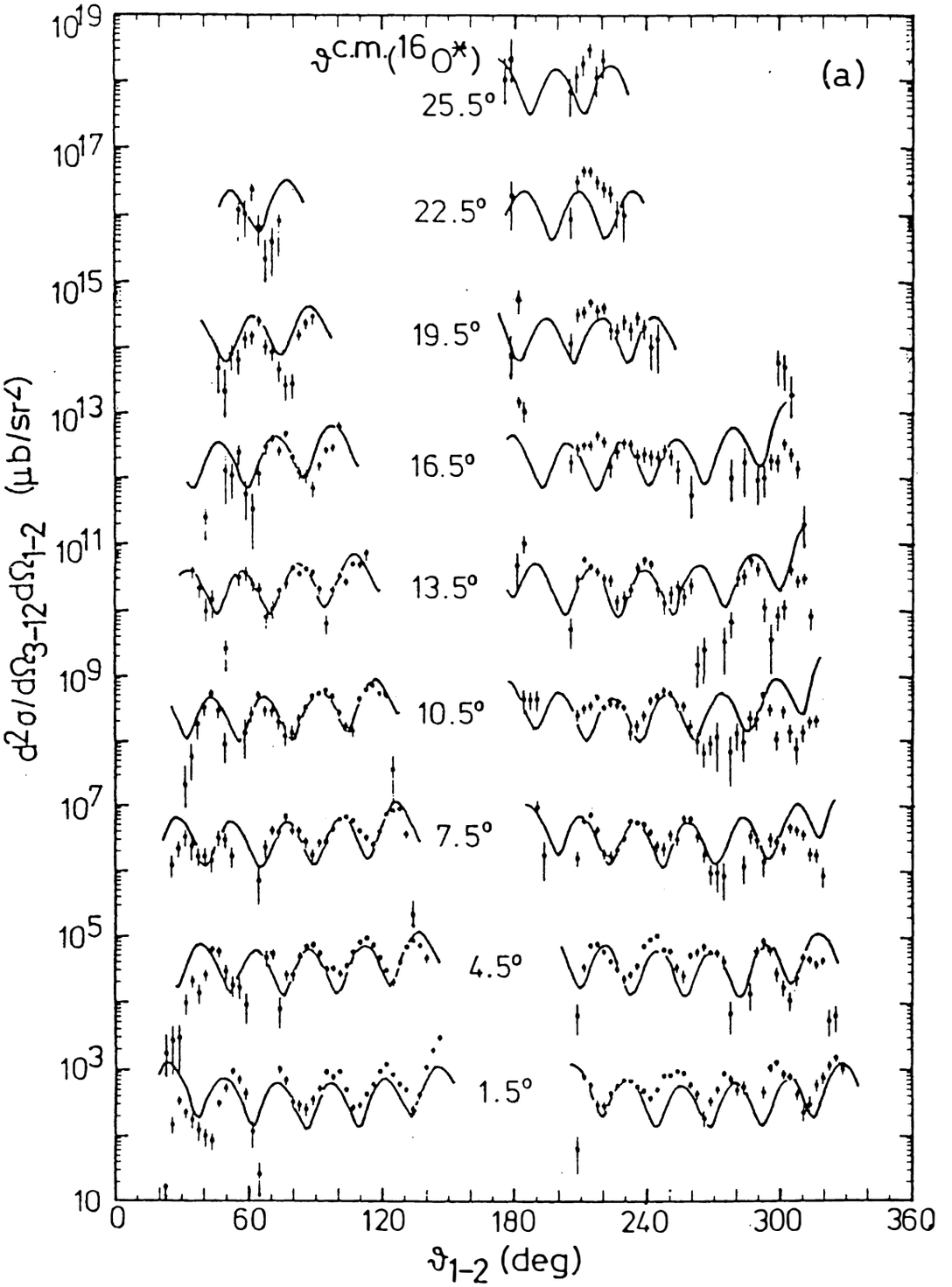
$\vartheta_{c.m.}(^{16}O^*)$
(a)
25.5°
22.5°
19.5°
16.5°
13.5°
10.5°
7.5°
4.5°
1.5°
$d^2\sigma/d\Omega_{3-12}d\Omega_{1-2}$ (μb/sr²)
ϑ_{1-2} (deg)
10^{19}
10^{17}
10^{15}
10^{13}
10^{11}
10^{9}
10^{7}
10^{5}
10^{3}
10
0
60
120
180
240
300
360

Fig. 10.

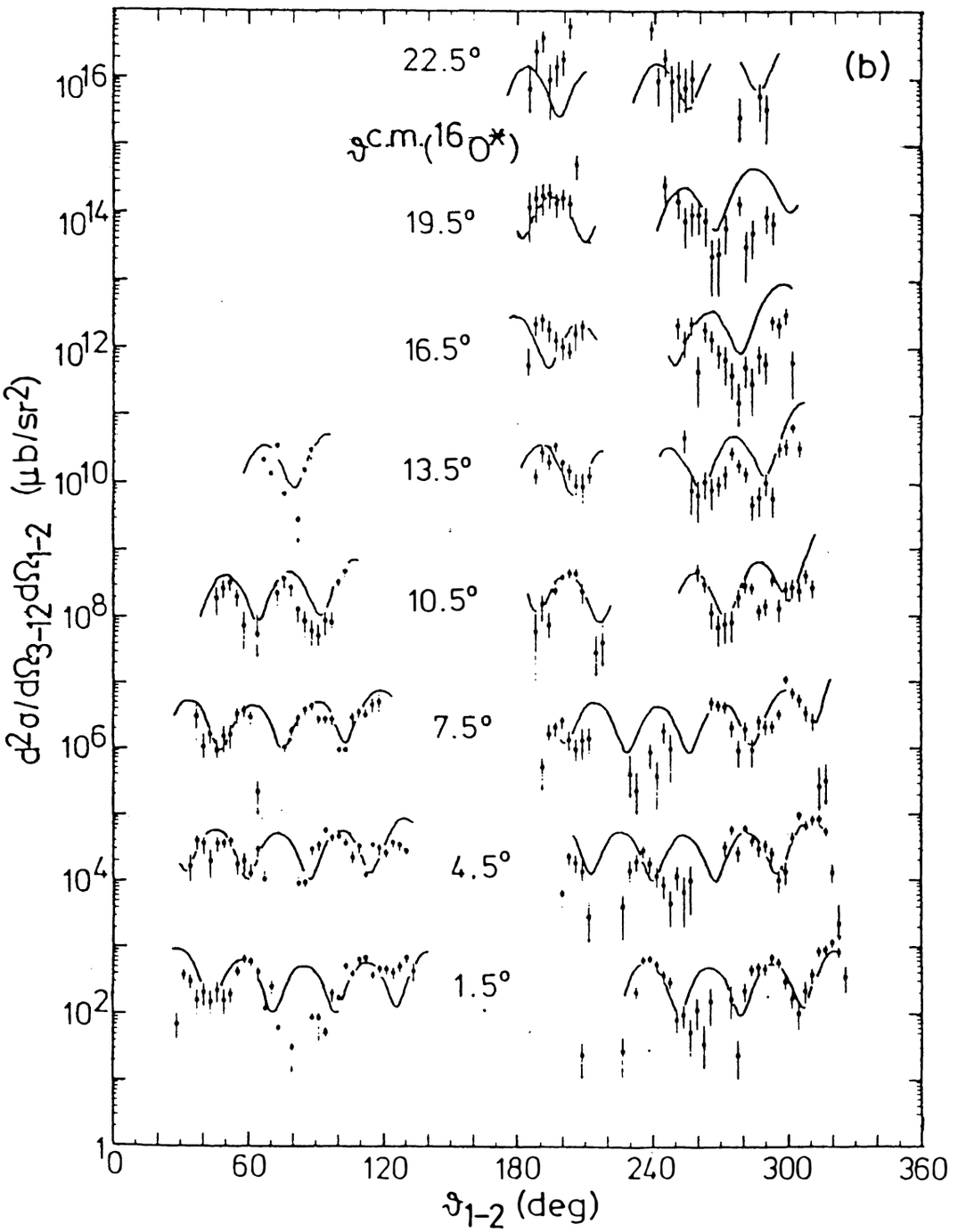
(b)
22.5°
$\vartheta^{c.m.}(^{16}O^*)$
19.5°
16.5°
13.5°
10.5°
7.5°
4.5°
1.5°
$d^2\sigma/d\Omega_{3-12}d\Omega_{1-2}$ (μb/sr²)
10^{16}
10^{14}
10^{12}
10^{10}
10^{8}
10^{6}
10^{4}
10^{2}
1
0
60
120
180
240
300
360
ϑ_{1-2} (deg)

Fig. 10.

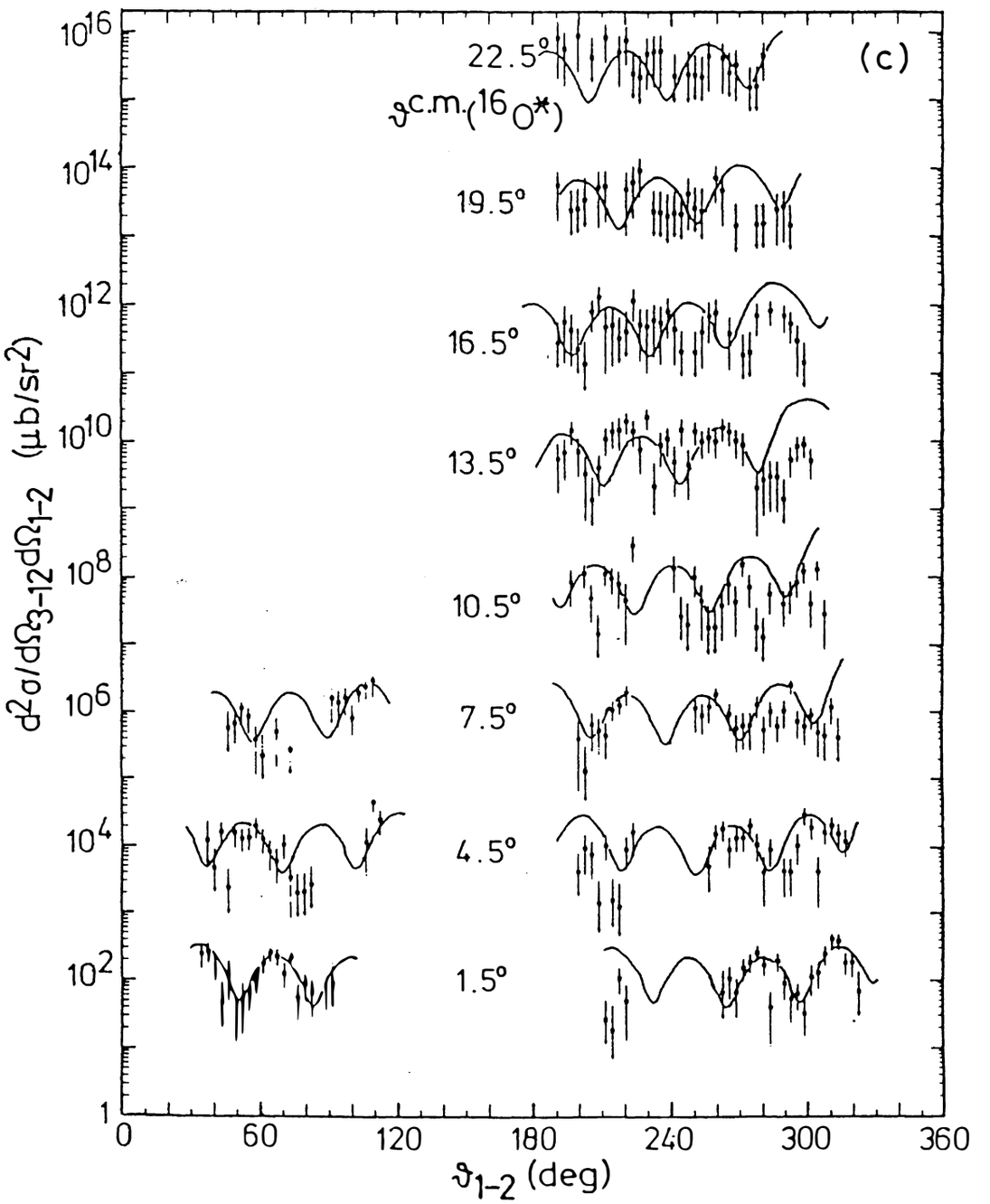
(c)
22.5°
$\vartheta_{c.m.}(^{16}O^*)$
19.5°
16.5°
13.5°
10.5°
7.5°
4.5°
1.5°
$d^2\sigma/d\Omega_{3-12}d\Omega_{1-2}$ (μb/sr^2)
ϑ_{1-2} (deg)
10^{16}
10^{14}
10^{12}
10^{10}
10^{8}
10^{6}
10^{4}
10^{2}
1
0
60
120
180
240
300
360

Fig. 10.

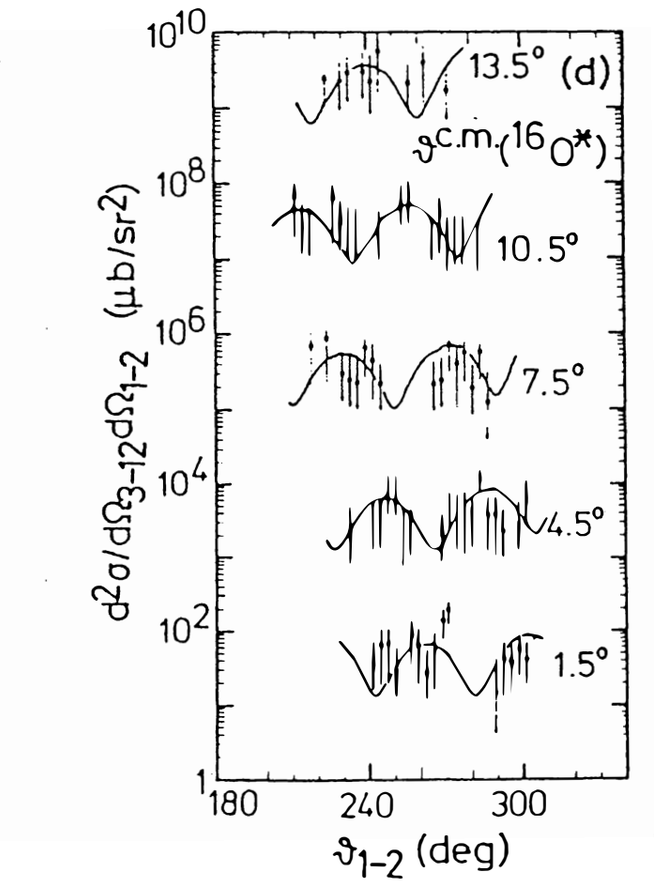
10^{10}
10^8
10^6
10^4
10^2
1
$d^2\sigma/d\Omega_{3-12}d\Omega_{1-2}$ (μb/sr^2)
13.5° (d)
$\vartheta^{c.m.}(^{16}O^*)$
10.5°
7.5°
4.5°
1.5°
180
240
300
ϑ_{1-2} (deg)

Fig. 10.

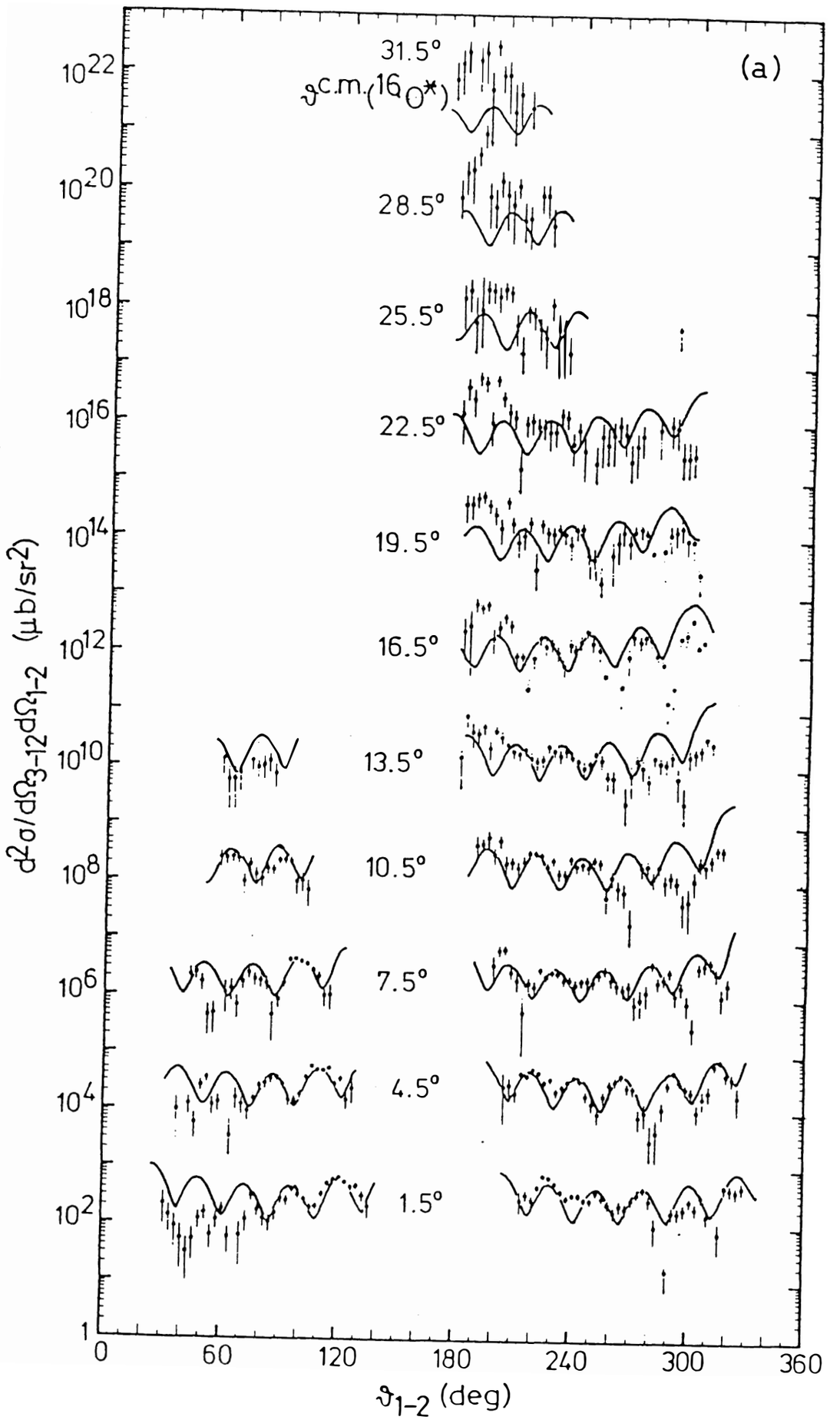
(a)
$\vartheta^{c.m.}(^{16}O^*)$
31.5°
28.5°
25.5°
22.5°
19.5°
16.5°
13.5°
10.5°
7.5°
4.5°
1.5°
$d^2\sigma/d\Omega_{3-12}d\Omega_{1-2}$ (μb/sr²)
ϑ_{1-2} (deg)
10^{22}
10^{20}
10^{18}
10^{16}
10^{14}
10^{12}
10^{10}
10^{8}
10^{6}
10^{4}
10^{2}
1
0
60
120
180
240
300
360

Fig. 11.

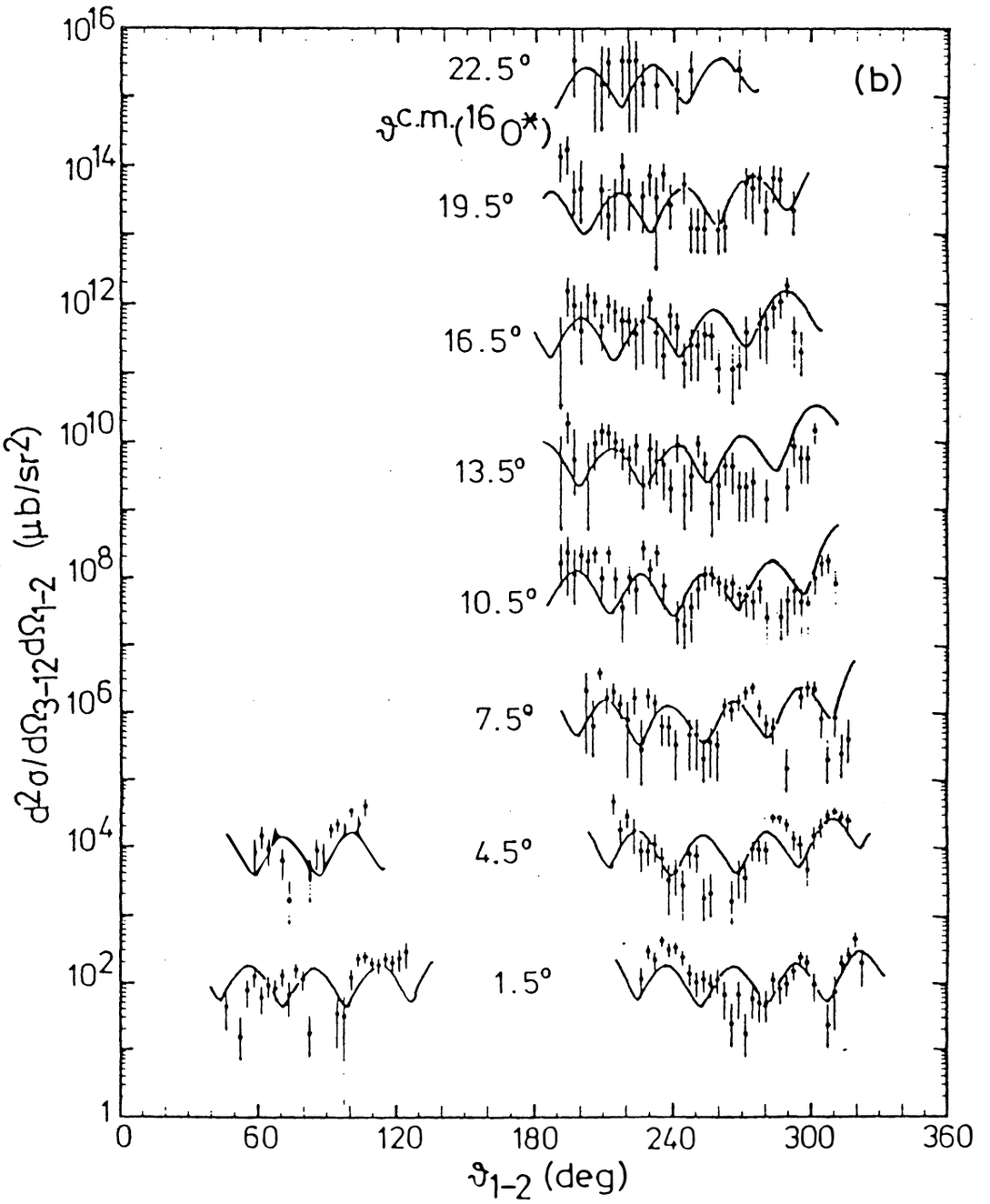
(b)
22.5°
ϑc.m.(16O*)
19.5°
16.5°
13.5°
10.5°
7.5°
4.5°
1.5°
d2σ/dΩ3-12dΩ1-2 (μb/sr2)
ϑ1-2 (deg)
10^16
10^14
10^12
10^10
10^8
10^6
10^4
10^2
1
0
60
120
180
240
300
360

Fig. 11.

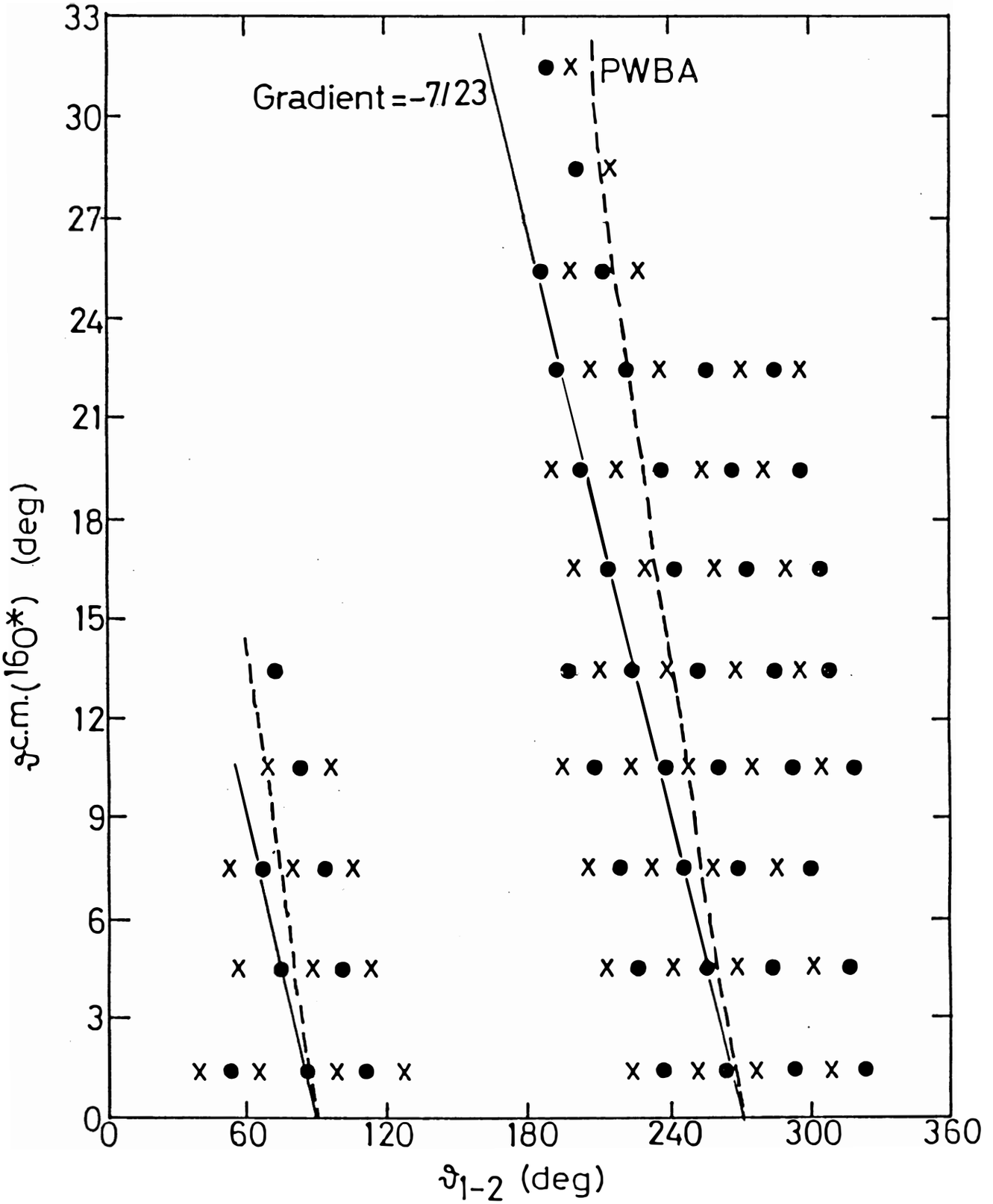
Gradient = -7/23
PWBA
33
30
27
24
21
18
15
12
9
6
3
0
0
60
120
180
240
300
360
ϑc.m.(16O*) (deg)
ϑ1-2 (deg)

Fig. 12.

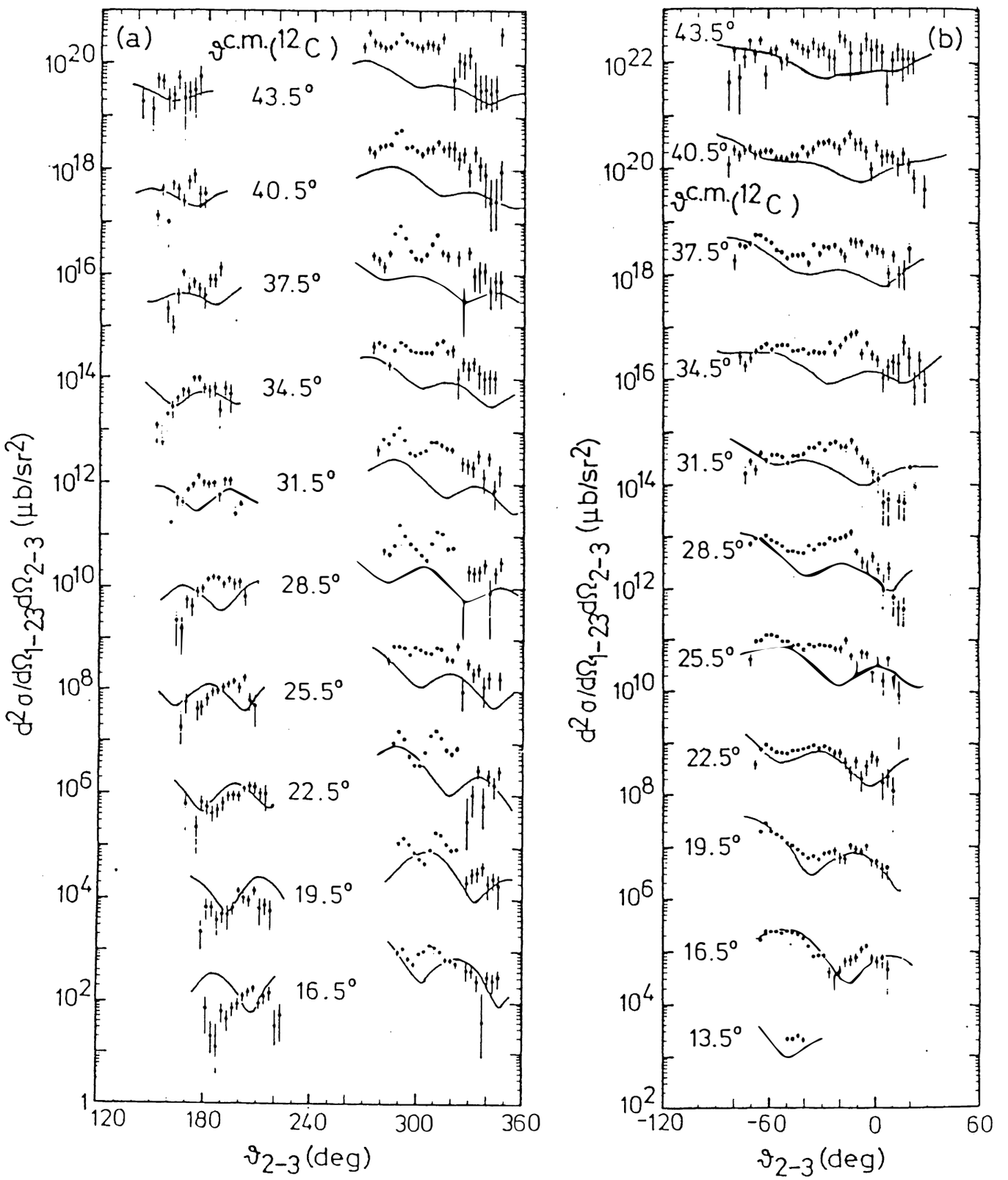
(a)
$\vartheta_{c.m.}(^{12}C)$
43.5°
40.5°
37.5°
34.5°
31.5°
28.5°
25.5°
22.5°
19.5°
16.5°
$d^2\sigma/d\Omega_{1-23}d\Omega_{2-3}$ (μb/sr²)
ϑ_{2-3} (deg)
(b)
43.5°
40.5°
$\vartheta_{c.m.}(^{12}C)$
37.5°
34.5°
31.5°
28.5°
25.5°
22.5°
19.5°
16.5°
13.5°
$d^2\sigma/d\Omega_{1-23}d\Omega_{2-3}$ (μb/sr²)
ϑ_{2-3} (deg)

Fig. 13.

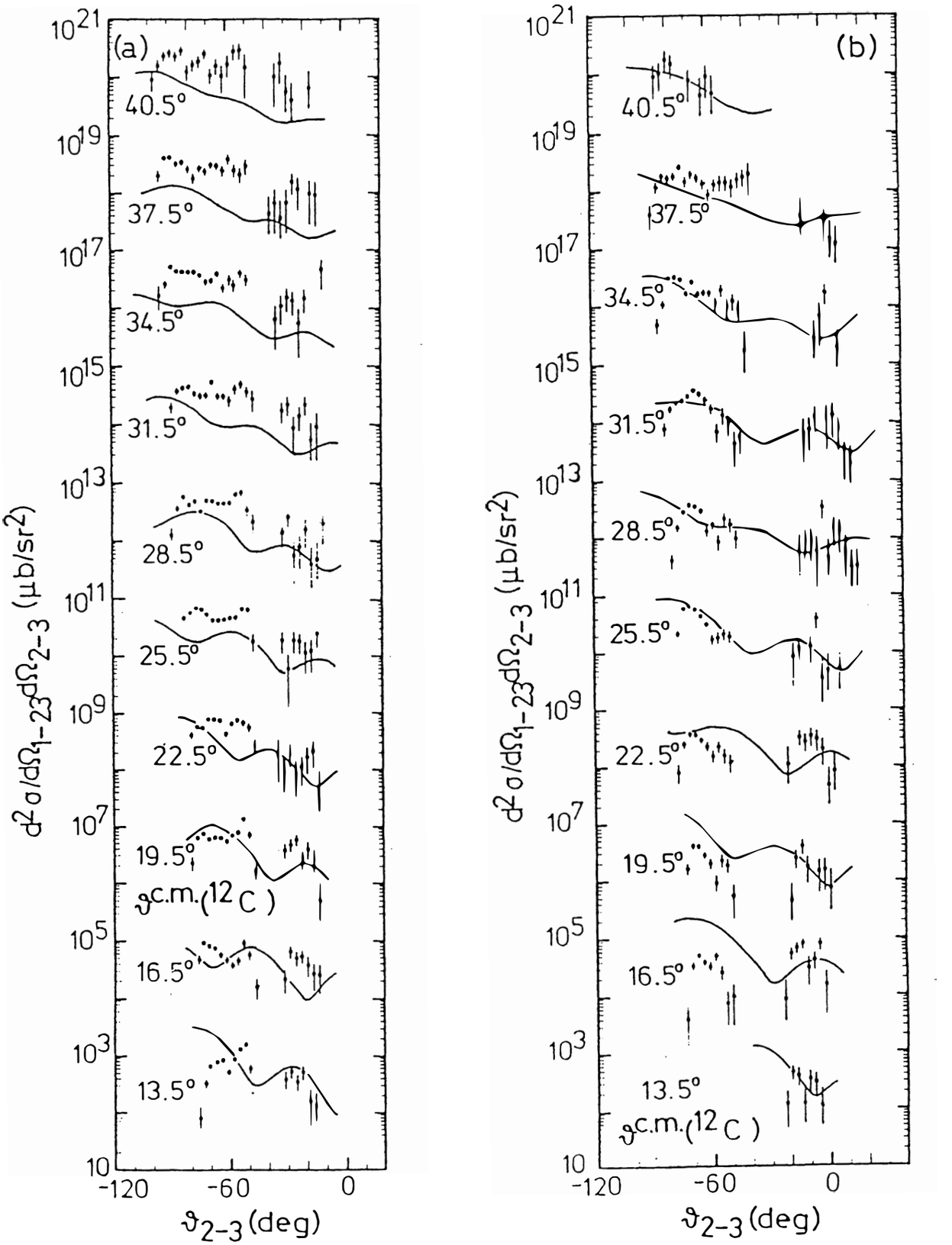
(a)
(b)
40.5°
37.5°
34.5°
31.5°
28.5°
25.5°
22.5°
19.5°
16.5°
13.5°
ϑc.m.(12C)
d²σ/dΩ1-23dΩ2-3 (μb/sr²)
ϑ2-3 (deg)
10²¹
10¹⁹
10¹⁷
10¹⁵
10¹³
10¹¹
10⁹
10⁷
10⁵
10³
10
-120
-60
0

Fig. 14.

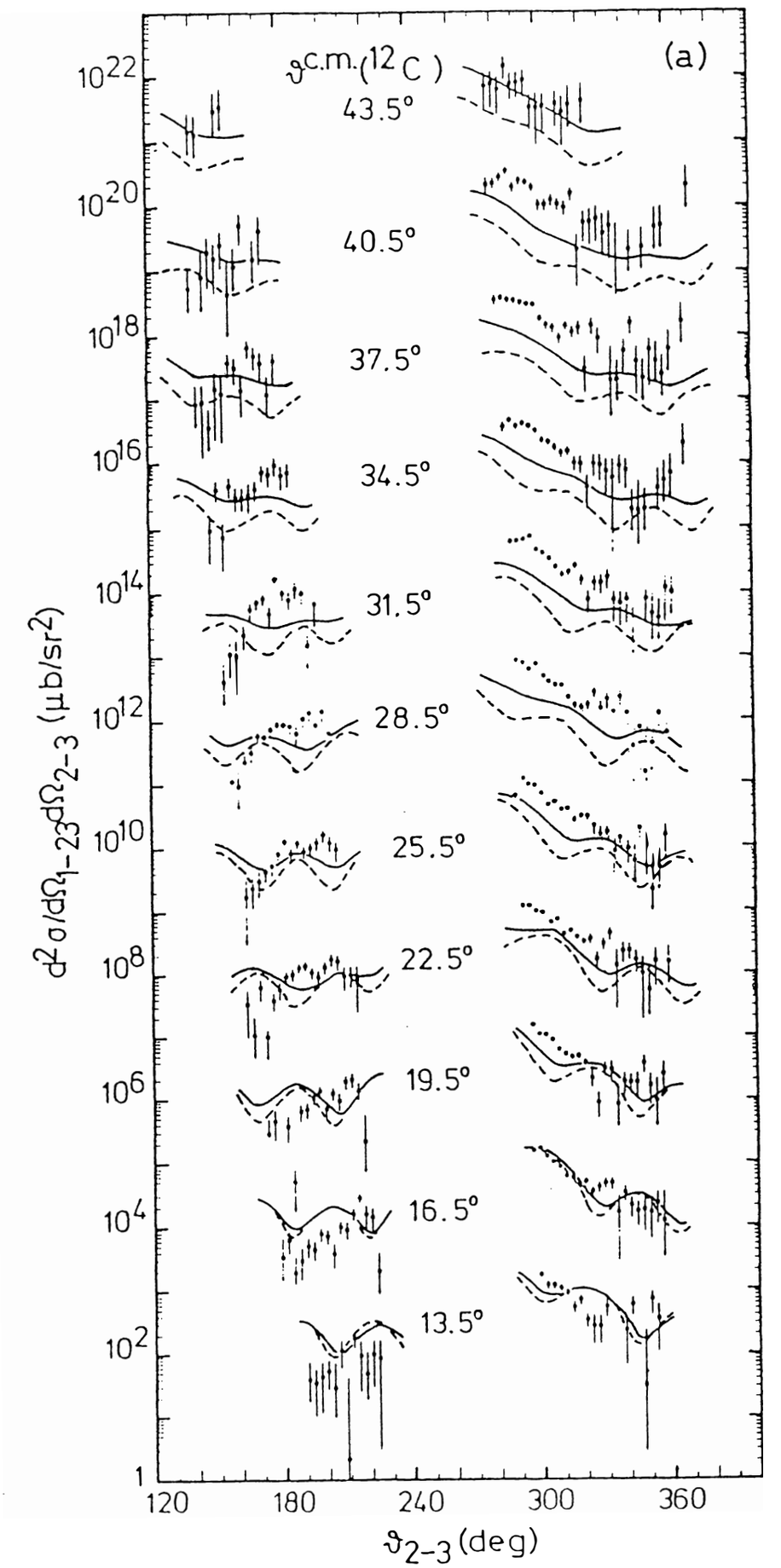
(a)
$\vartheta_{c.m.}(^{12}C)$
43.5°
40.5°
37.5°
34.5°
31.5°
28.5°
25.5°
22.5°
19.5°
16.5°
13.5°
$d^2\sigma/d\Omega_{1-23}d\Omega_{2-3}$ (μb/sr²)
10^{22}
10^{20}
10^{18}
10^{16}
10^{14}
10^{12}
10^{10}
10^{8}
10^{6}
10^{4}
10^{2}
1
120
180
240
300
360
ϑ_{2-3} (deg)

Fig. 15.

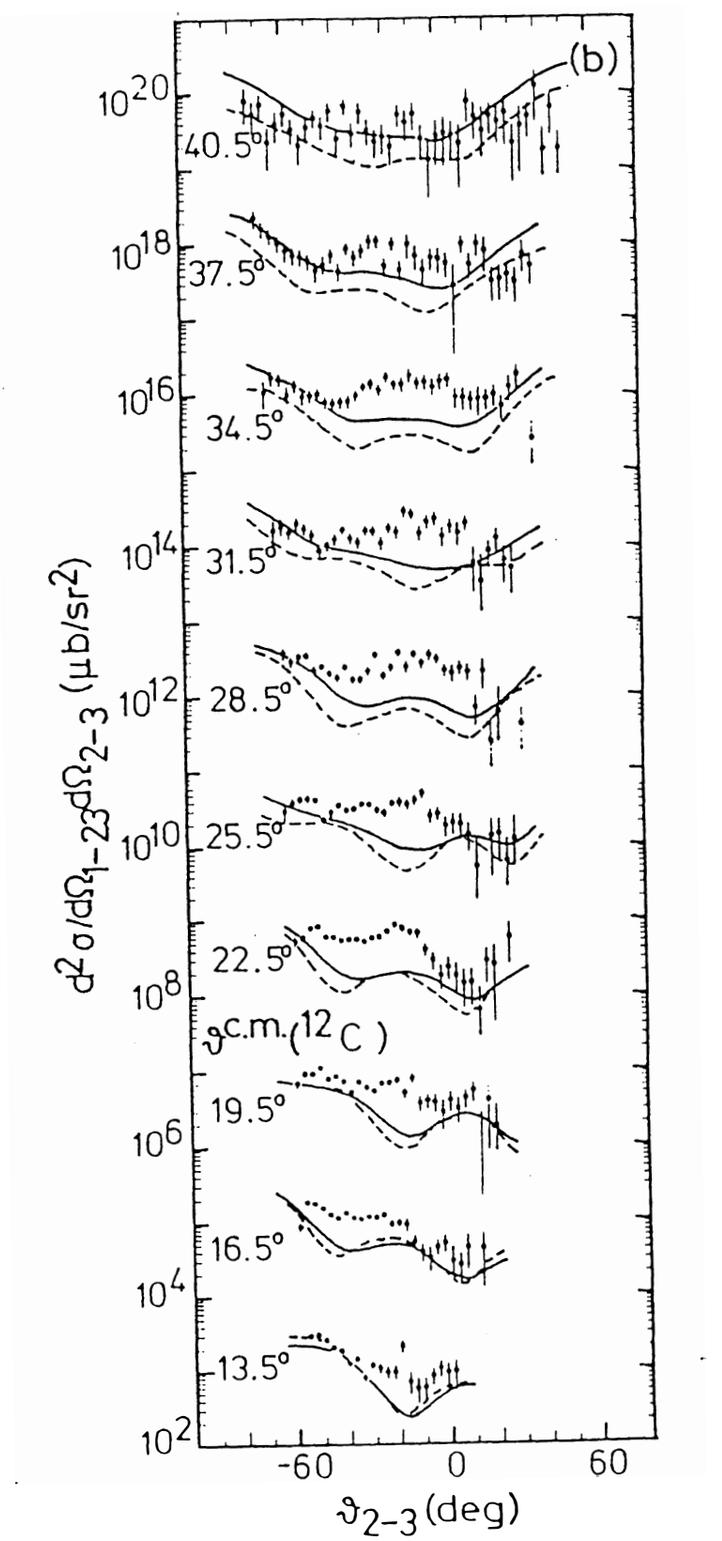
(b)
10^{20}
40.5°
10^{18}
37.5°
10^{16}
34.5°
10^{14}
31.5°
10^{12}
28.5°
10^{10}
25.5°
10^{8}
22.5°
$\vartheta_{c.m.}(^{12}C)$
10^{6}
19.5°
16.5°
10^{4}
13.5°
10^{2}
-60
0
60
ϑ_{2-3} (deg)
$d^2\sigma/d\Omega_{1-23}d\Omega_{2-3}$ (μb/sr^2)

Fig. 15.

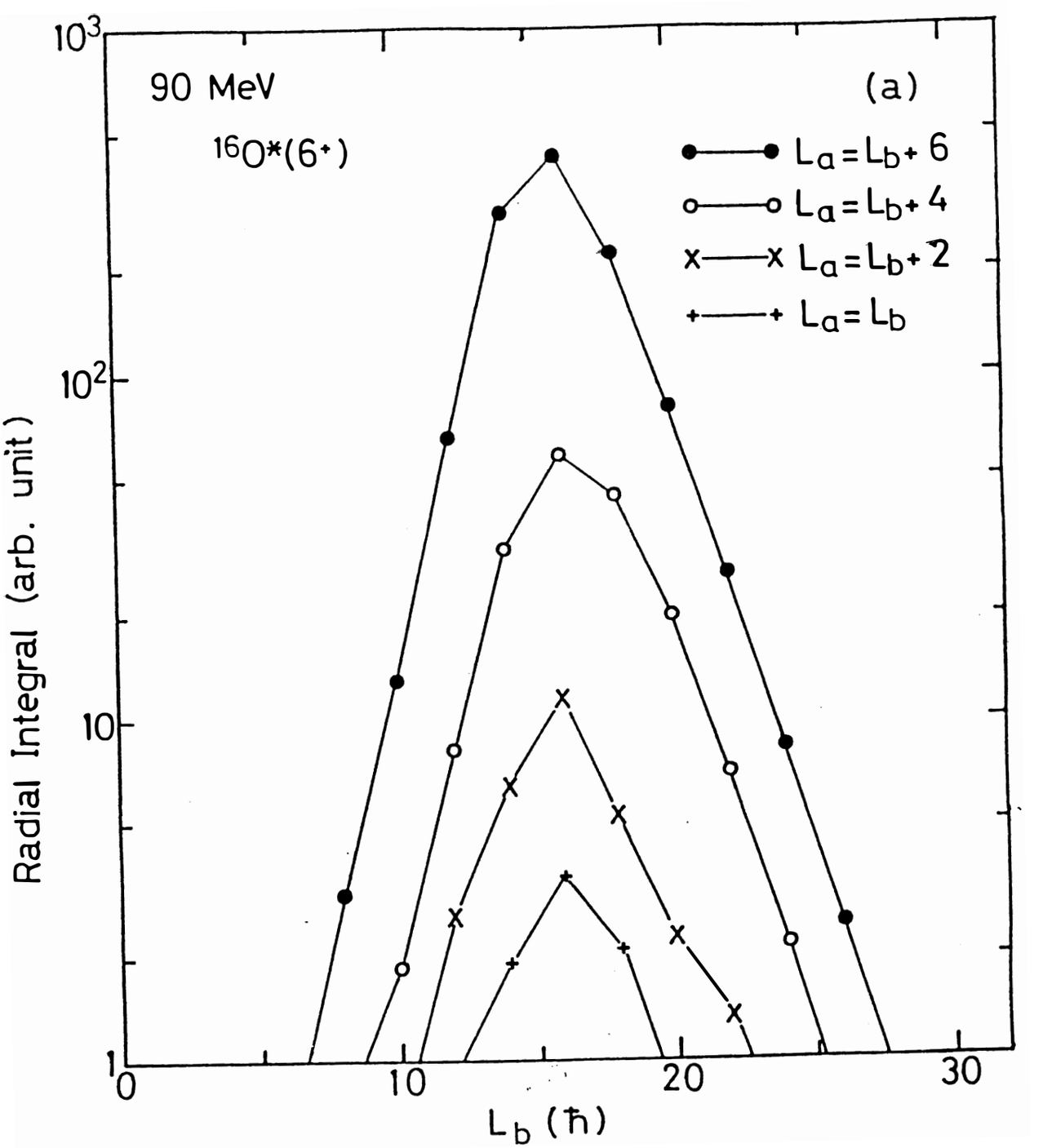
90 MeV
(a)
$^{16}O^{*}(6^{+})$
$L_a = L_b + 6$
$L_a = L_b + 4$
$L_a = L_b + 2$
$L_a = L_b$
Radial Integral (arb. unit)
10^3
10^2
10
1
0
10
20
30
L_b (ħ)

Fig. 16.

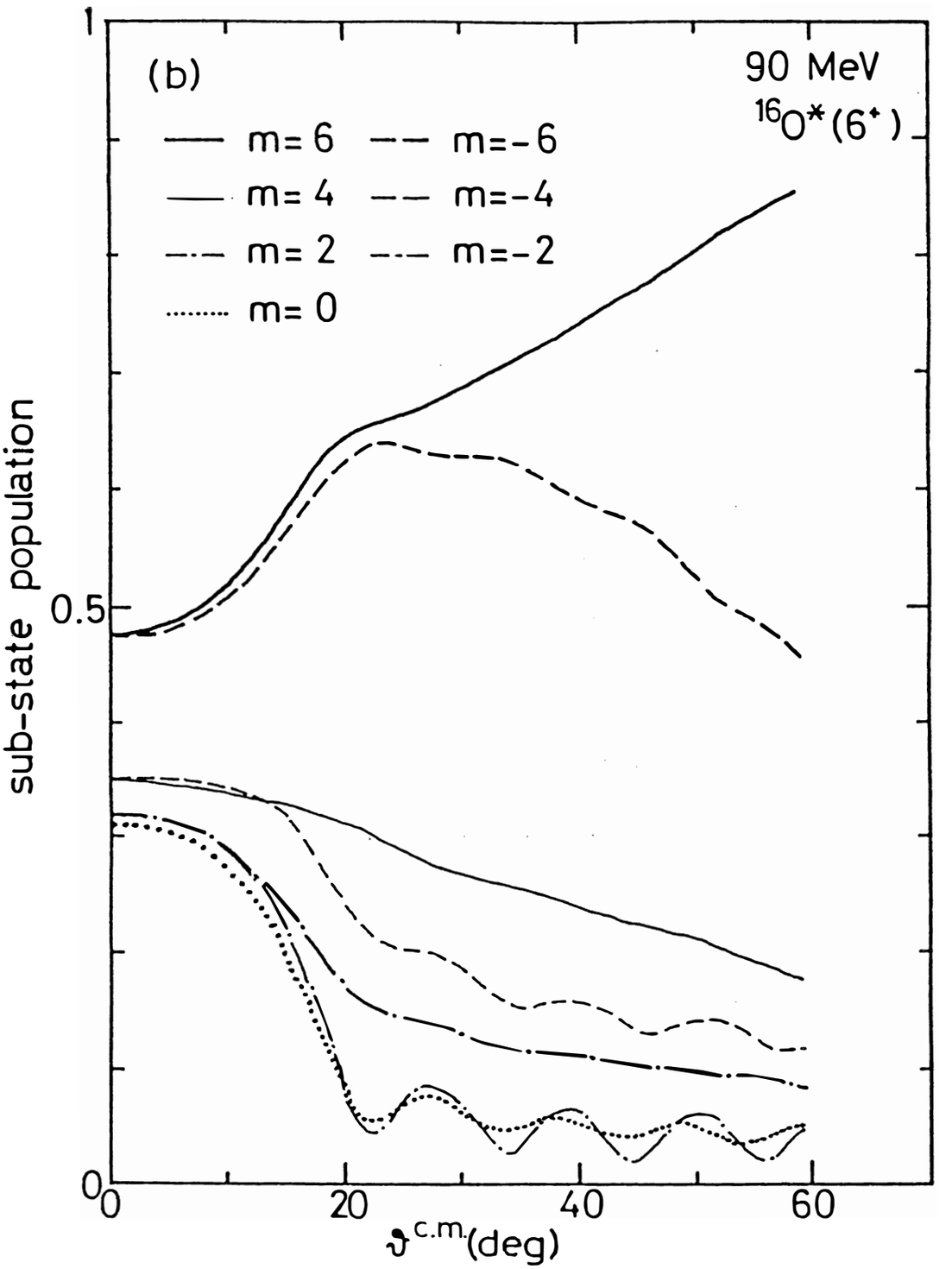
(b)
90 MeV
$^{16}O^*(6^+)$
m= 6
m=-6
m= 4
m=-4
m= 2
m=-2
m= 0
sub-state population
1
0.5
0
0
20
40
60
$\vartheta^{c.m.}$(deg)

Fig. 16.

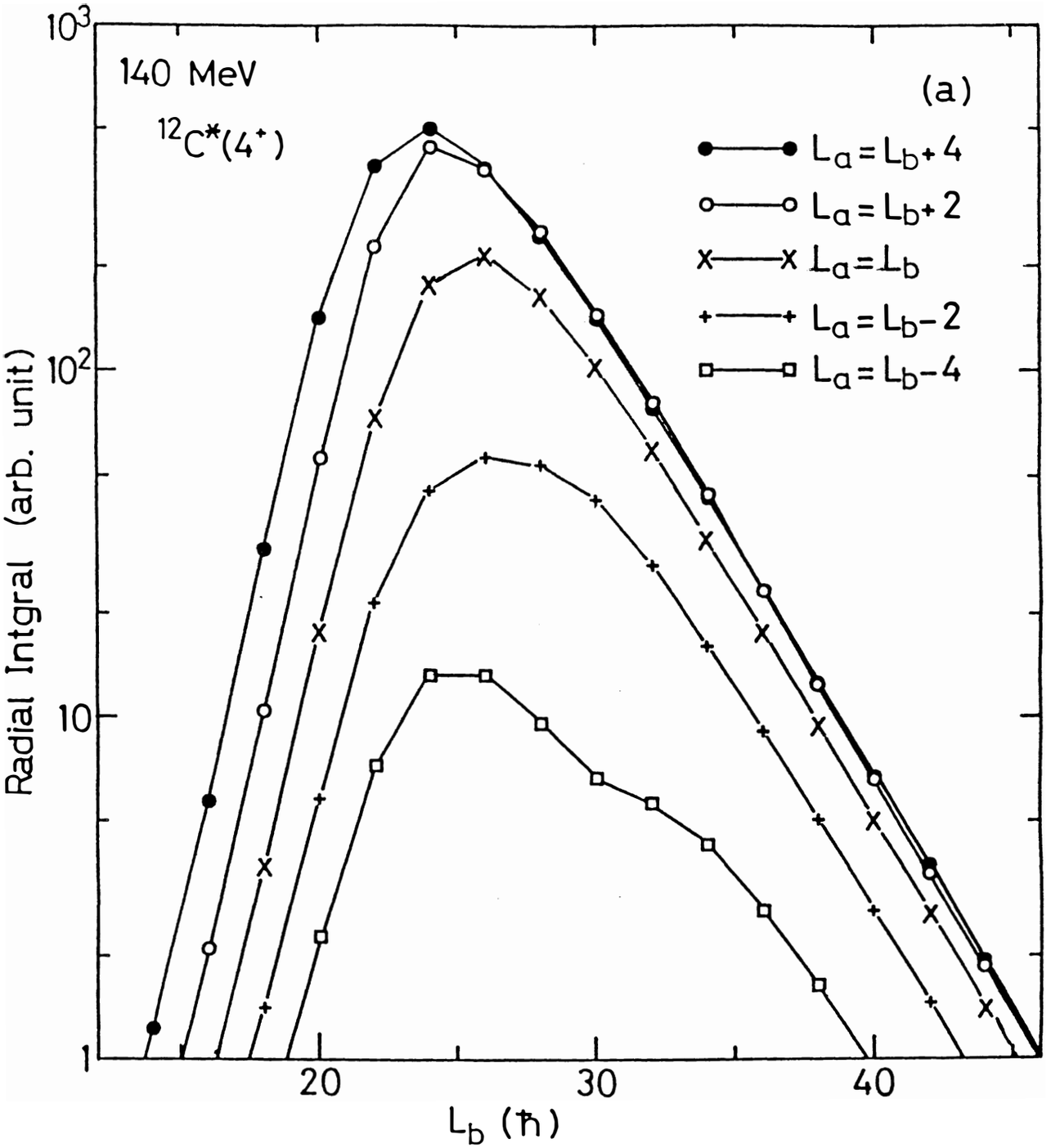
140 MeV
$^{12}C^*(4^+)$
(a)
$L_a = L_b + 4$
$L_a = L_b + 2$
$L_a = L_b$
$L_a = L_b - 2$
$L_a = L_b - 4$
Radial Intgral (arb. unit)
10^3
10^2
10
1
20
30
40
L_b (ħ)

Fig. 17.

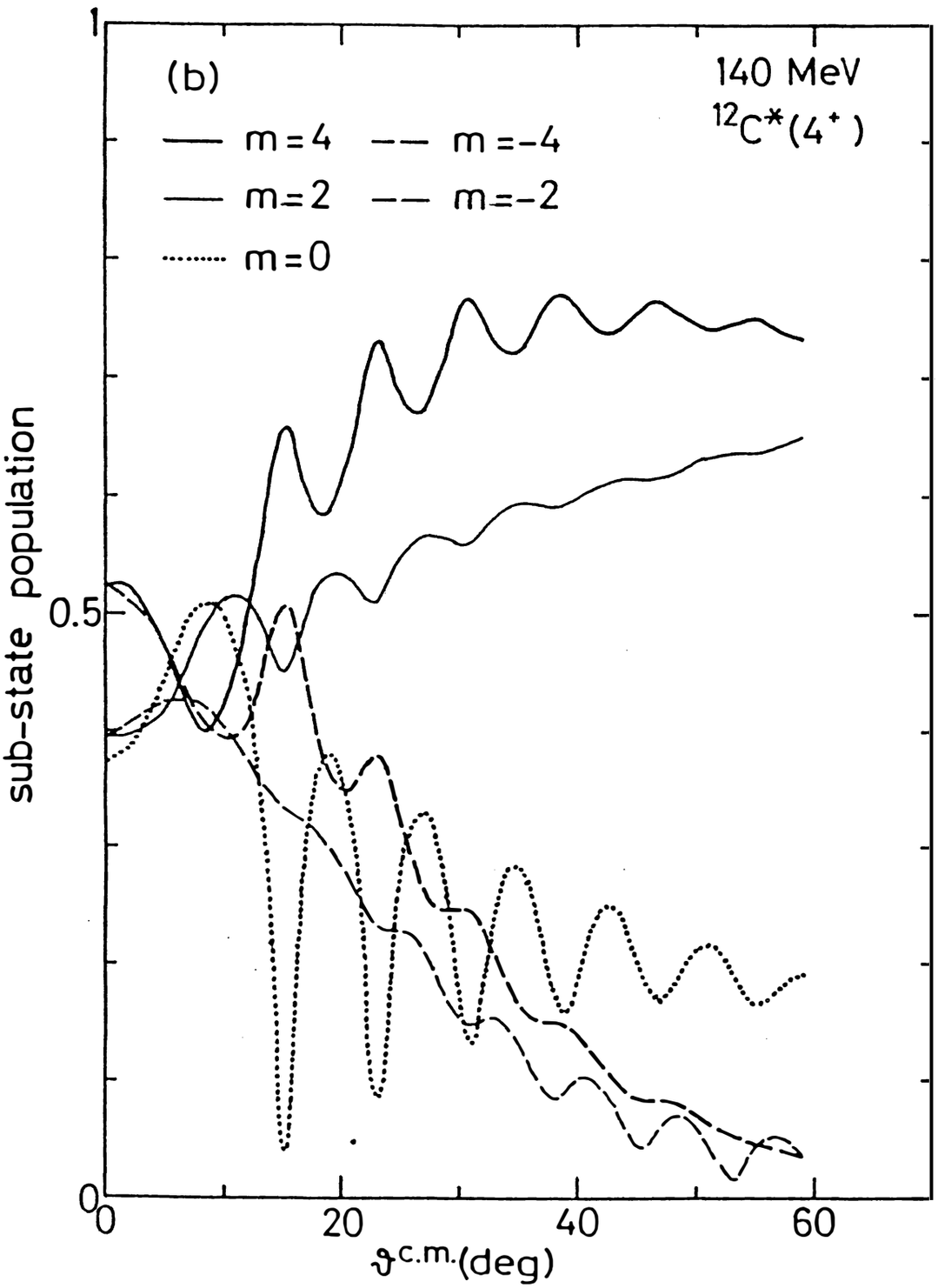
(b)
140 MeV
$^{12}C^*(4^+)$
m = 4
m = -4
m = 2
m = -2
m = 0
sub-state population
1
0.5
0
0
20
40
60
$\vartheta^{c.m.}$(deg)

Fig. 17.

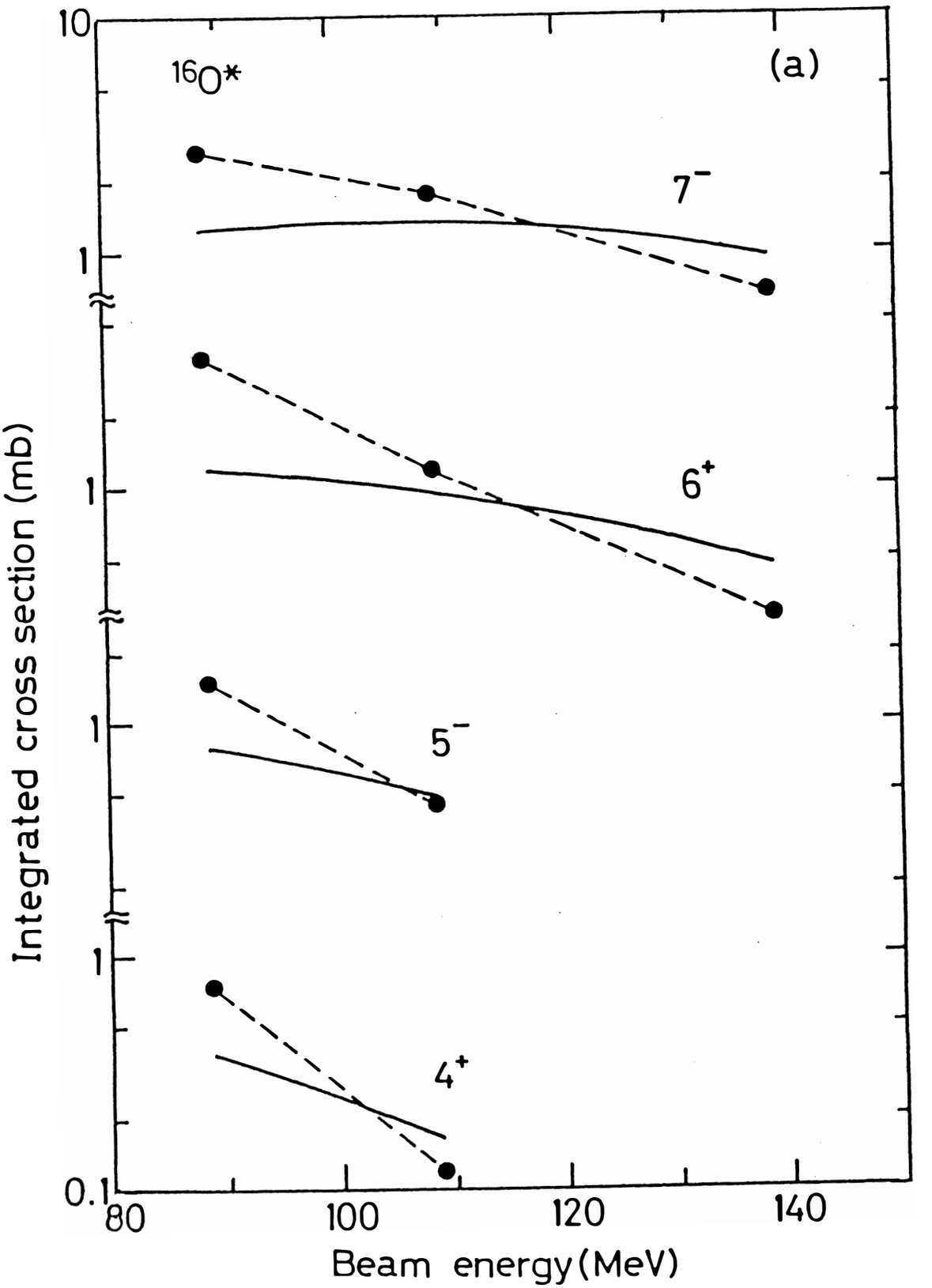
10
1
1
1
1
0.1
$^{16}O^*$
(a)
7^-
6^+
5^-
4^+
80
100
120
140
Integrated cross section (mb)
Beam energy (MeV)

Fig. 18.

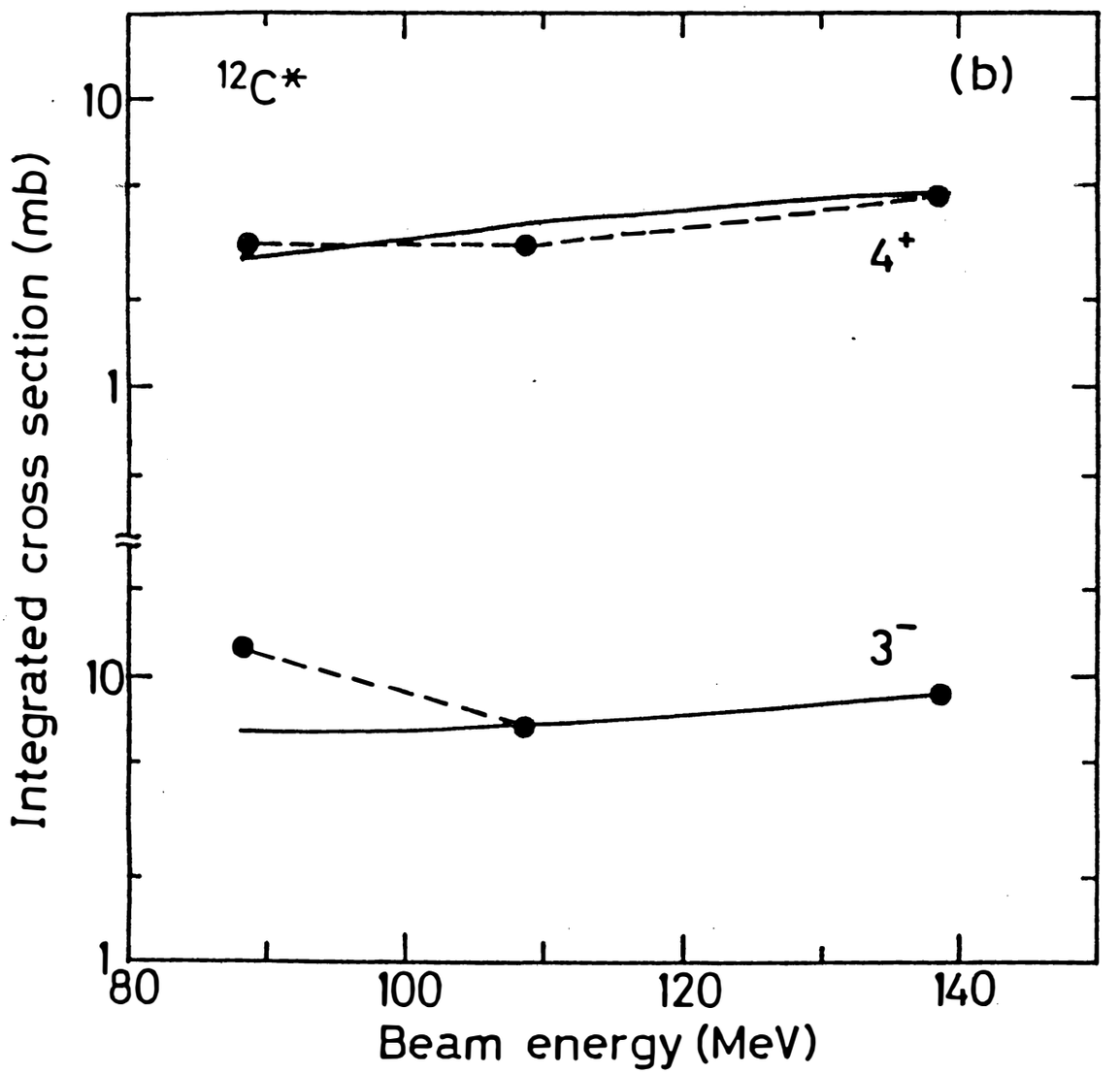
$^{12}C^*$
(b)
10
1
10
1
4^+
3^-
Integrated cross section (mb)
80
100
120
140
Beam energy (MeV)

Fig. 18.

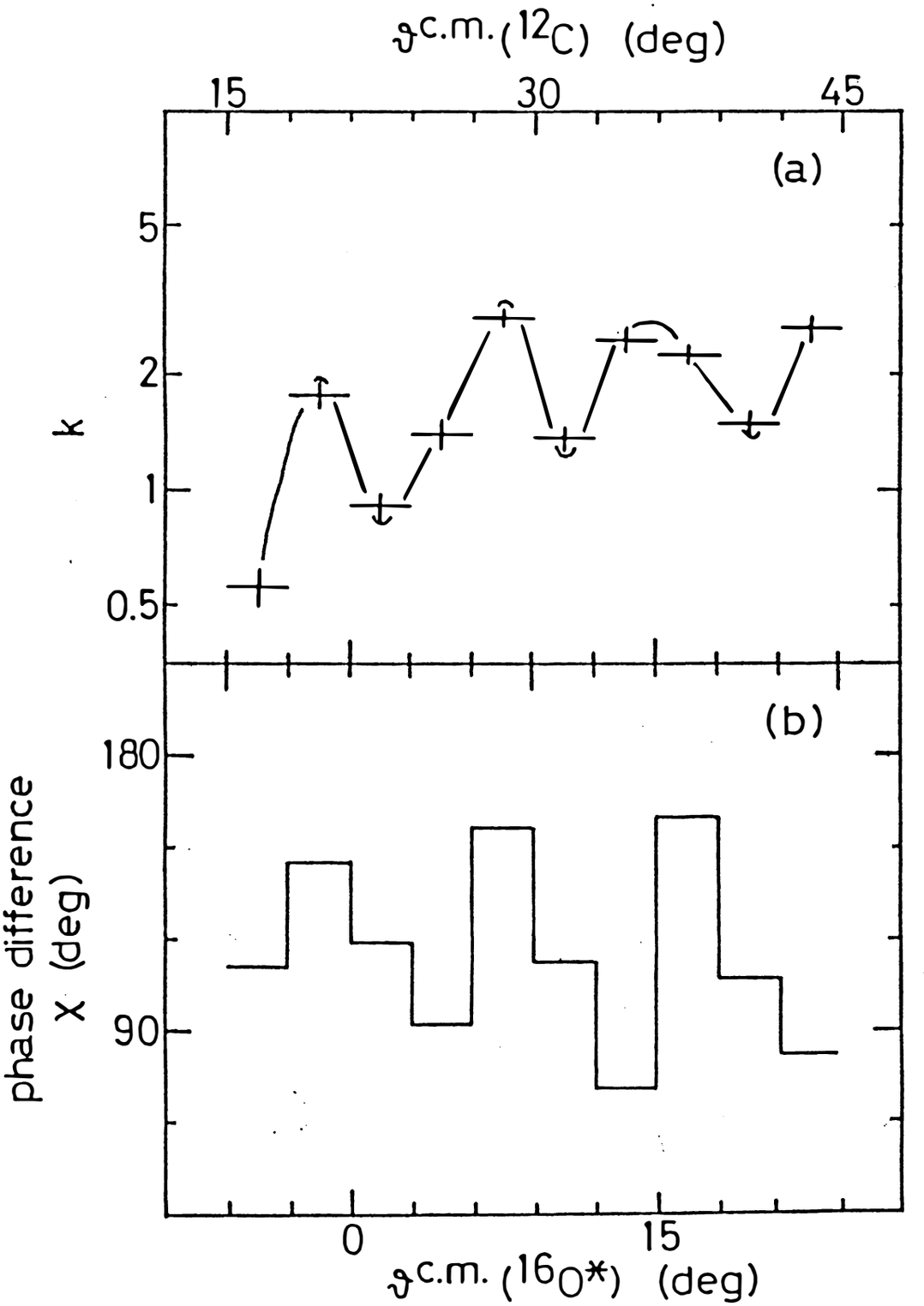
ϑc.m.(12C) (deg)
15
30
45
(a)
5
2
1
0.5
k
(b)
180
90
phase difference
χ (deg)
0
15
ϑc.m. (16O*) (deg)

Fig. 19.

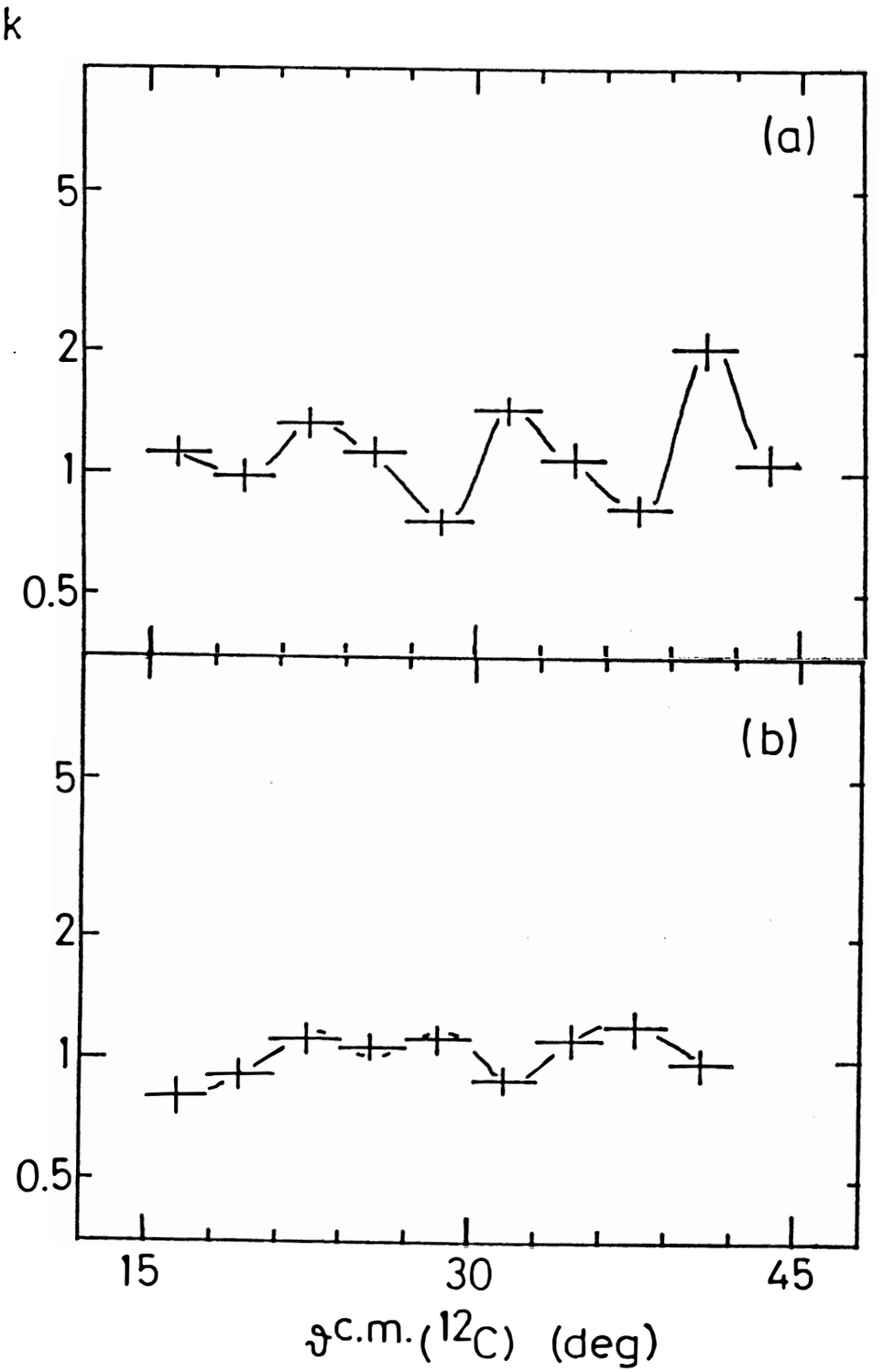

Fig. 20.

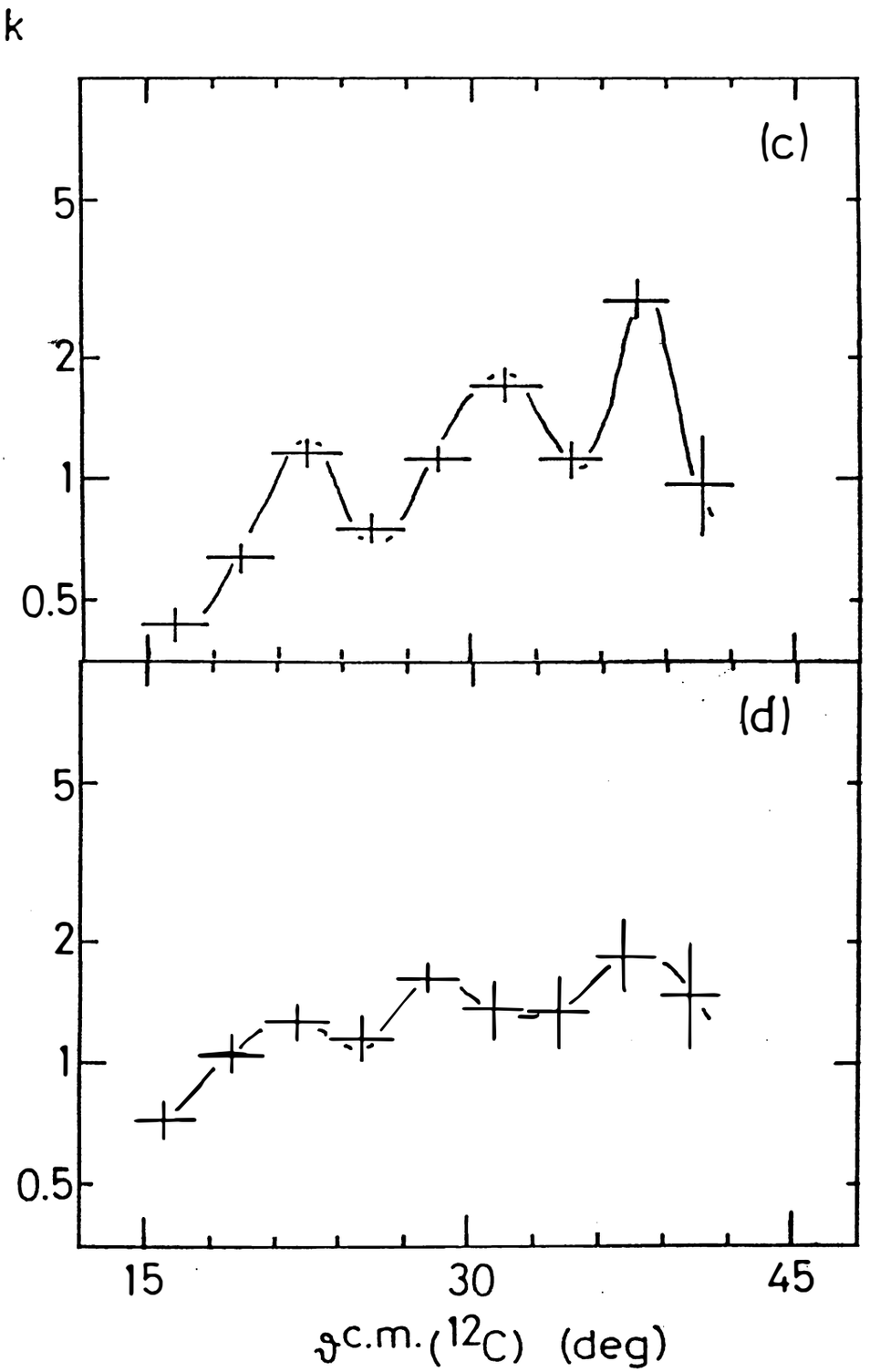

Fig. 20.

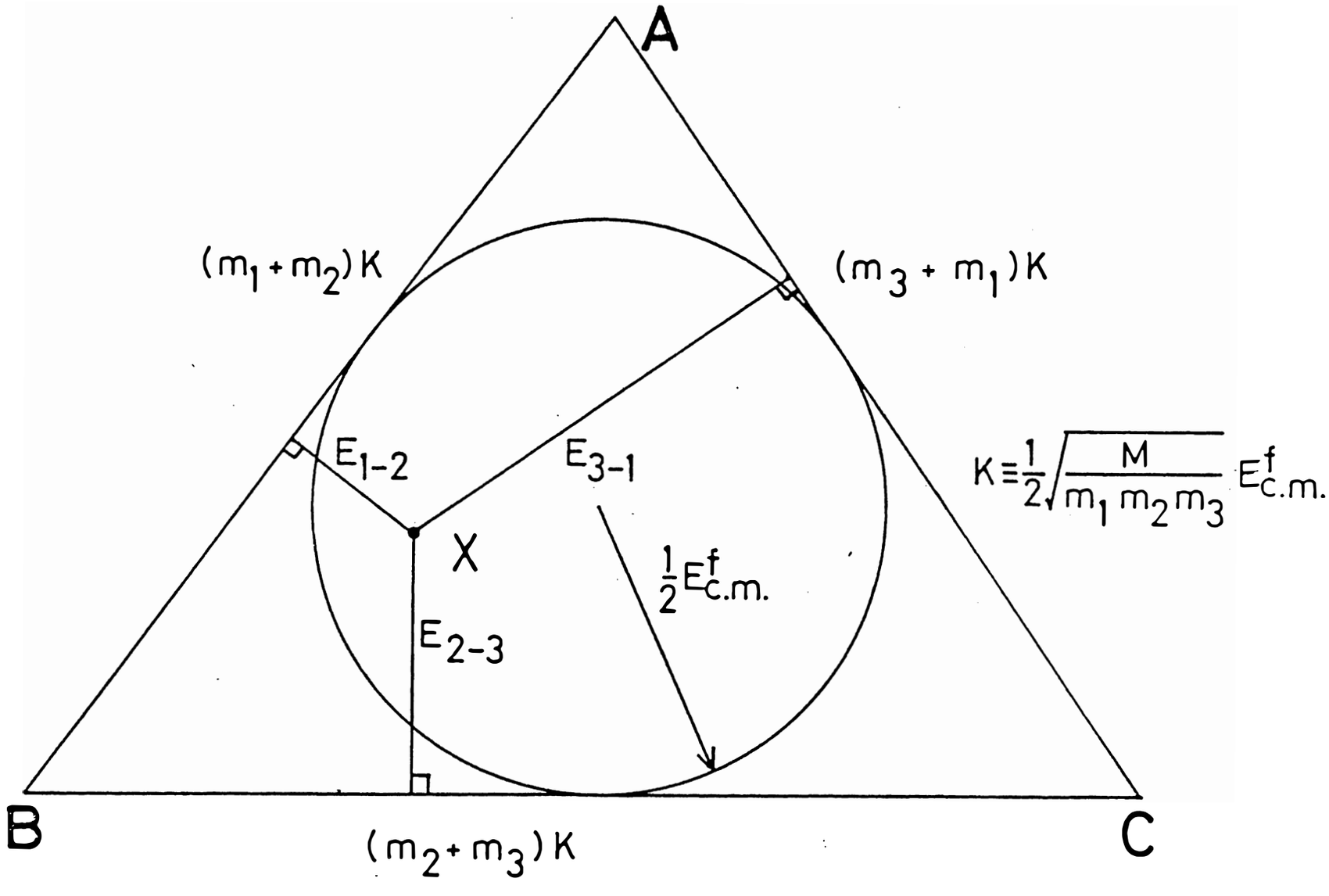
A
B
C
$(m_1 + m_2)K$
$(m_3 + m_1)K$
$(m_2 + m_3)K$
E_{1-2}
E_{3-1}
E_{2-3}
X
$\frac{1}{2}E^f_{c.m.}$
$K \equiv \frac{1}{2}\sqrt{\frac{M}{m_1 m_2 m_3}}\, E^f_{c.m.}$

Fig. 21.

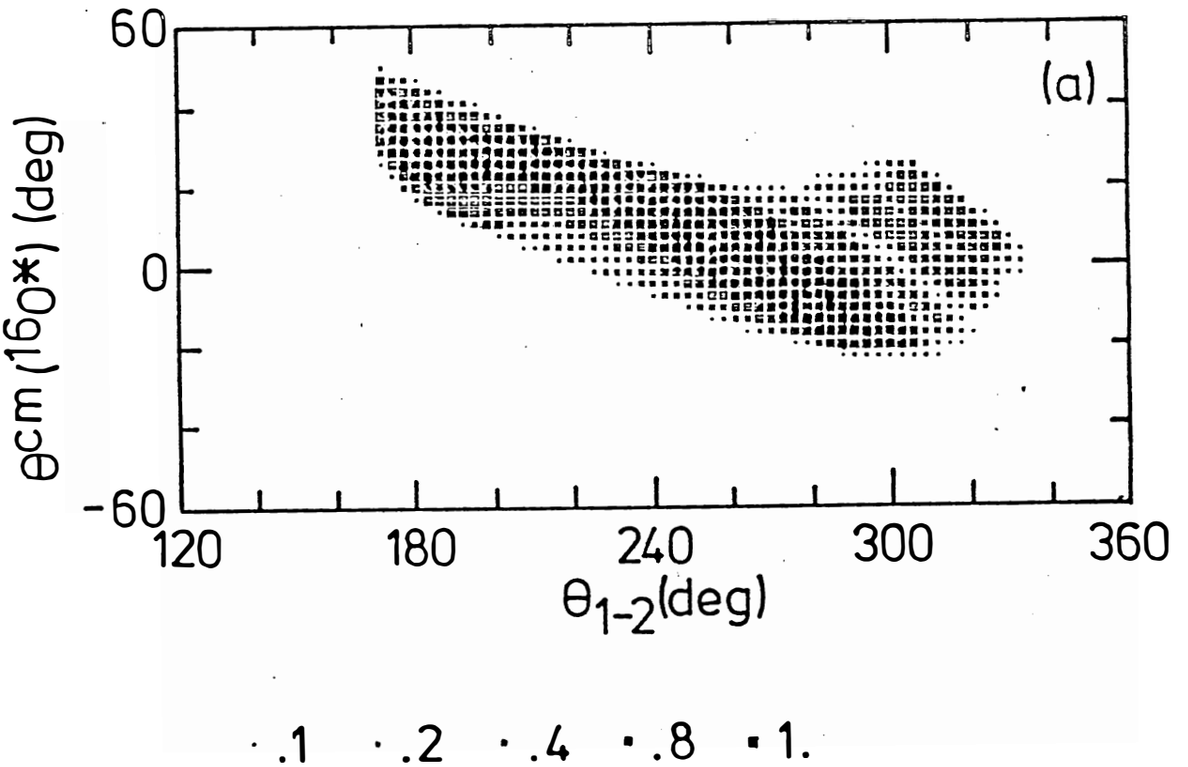
60
0
-60
120
180
240
300
360
(a)
$\theta_{cm}(^{16}O^*)$ (deg)
θ_{1-2}(deg)
.1 .2 .4 .8 1.

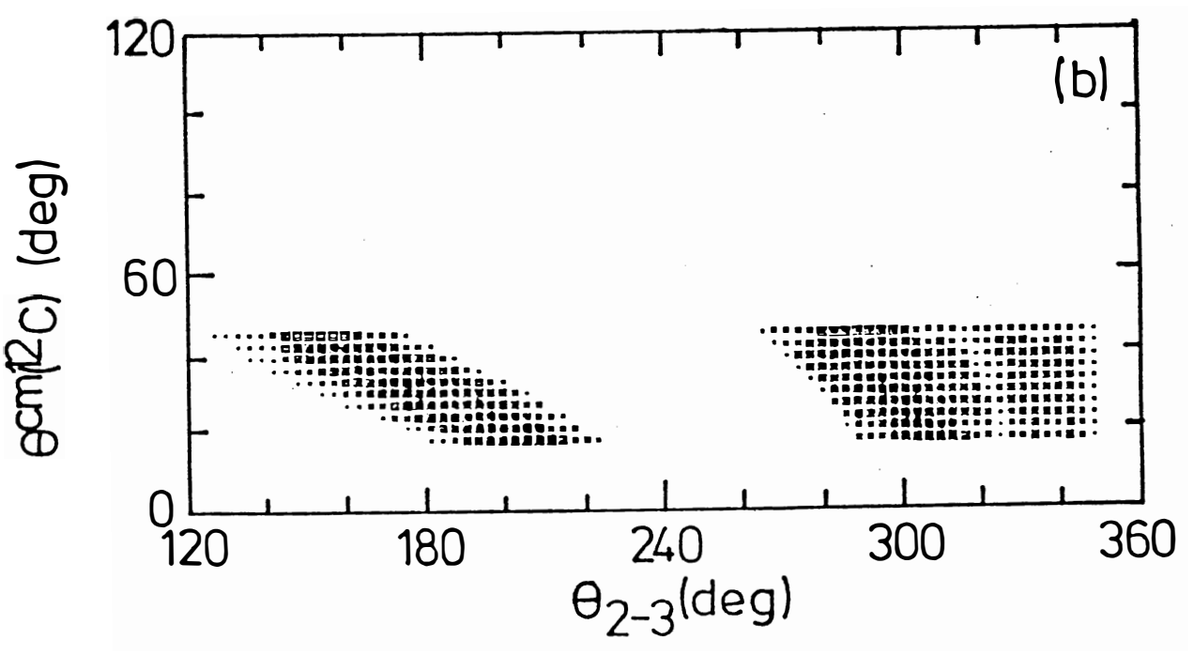
120
60
0
120
180
240
300
360
(b)
$\theta_{cm}(^{12}C)$ (deg)
θ_{2-3}(deg)

Fig. 22.